Fabrication of Nanoporous Si Composite Anodes and their Application to All-solid-state Lithium-ion Batteries

RYOTA OKUNO

FEBRUARY 2022

Doctoral Thesis at Nara Institute of Science and Technology

Fabrication of Nanoporous Si Composite Anodes and their Application to All-solid-state Lithium-ion Batteries

CONTENTS

1. GENERAL INTRODUCTION

1.1. Lithium-ion Batteries: Past and Present

The glorious history of lithium-ion batteries, LIBs, began when Whittingham presented the concept of intercalation reactions for rechargeable batteries [1]. Thereafter the principle of LIB formulated in the late of 1970s [2] was embodied as a cell using Li_xWO_2 cathode and TiS_2 anode [3]. Goodenough's discovery for cathode, in which lithiated transition metal oxides with $NaFeO_2$ structure reversibly intercalate Li^+ ions, is a major milestone [4]. Regarding anode, Yoshino described a by-product of oil production called petroleum coke in a seminal patent [5]. Thus, the main elements of LIBs were invented by Whittingham, Goodenough, and Yoshino. In 2019, they were awarded the Nobel Prize in Chemistry for the achievements. However, there were many studies required to develop commercial LIBs with superior properties compared to Ni-Cd and Ni-MH batteries. After a lot of challenges to memory effect, low specific energy, and poor charge retention, Sony was the first to manufacture LIBs in 1991. The original product had energy density of 200 Wh L^{-1} and specific energy of 80 Wh kg^{-1} with a charge limitation of 4.1 V. LIB's performance has improved significantly after the commercialization. The cathodes, anodes, and electrolytes were modified to reach higher energy densities, higher charge/discharge rates, and longer cycle life. Current LIBs commonly use transition metals oxides as the cathode active materials. In addition, the electrolytes are generally composed of lithium salts such as $LiPF_6$ and organic solvents such as ethylene carbonate. The evolution of anodes related to my work is briefly described below.

Innovative anode materials can be classified into three groups based on their performance and reaction mechanism.

1) Intercalation/deintercalation materials

C-based materials

2) Alloy/dealloy materials

Si, SiO, Ge, SnO_2 etc.

3) Conversion materials

metal oxides, metal phosphides, metal sulphides, and metal nitrides

First, C-based materials have been recognized as appropriate anode materials due to their availability, stability, and cost. There are two categories according to the degree of crystallinity and C atoms stacking [6]:

a) Hard C (non-graphitizable C) where crystallites possess disordered orientation

b) Soft C (graphitizable C) where crystallites are stacked almost in the same direction

Hard C exhibited high capacity and enhanced stability. Furthermore, the large d_{002} spacing (>0.372 nm) did not experience much volume change upon lithiation and provided excellent reversibility even at higher charging voltage [7]. As such, the 2nd generation of LIBs used the hard C instead of Yoshino's cokes as the anode material. They were rated at 220 Wh L^{-1} and 85 Wh kg^{-1} with the charging of 4.2 V [8]. This was about 10% increase in volumetric energy density over the first generation. On the other hand, soft C is quite popular because of appropriate reversible capacity, long cycle life, and good coulombic efficiency [9-13]. Natural graphite found commercial success by introducing C or Zr coating [14,15] and surface functionalizing [16] to limit direct contact with electrolytes. Even since the graphite anodes were made feasible, the volumetric capacity has undergone significant enhancements. As the result, the market share was completely dominated by graphite-based materials. However, the use of commercially available graphites is still limited to low power electronics like mobile phones due to a low specific capacity of 372 mAh g^{-1}. Recently, the research activity is strongly focused on porous C, nanotubes, nanofibers, and graphene. The size reduction and the unique shape introduce novel properties in LIBs [17-22]. For example, C nanorings with 20 nm outer diameters and 3.5 nm wall thickness showed outstanding performance: capacity over 1200 mAh g^{-1} and current density of 0.4 A g^{-1}.

Second, Si, SiO, Ge and SnO_2 etc. react with Li according to alloy/dealloy mechanism. Their theoretical capacity ranges from 782 mAh g^{-1} for SnO_2 up to 4199 mAh g^{-1} for Si [23-25]. The major drawback was the poor cycle life due to the high-volume expansion/contraction during alloy/dealloy process. To overcome these issues, the downsizing to nanoscale and the fabrication of composites are the most promising. Nanostructured alloy materials with different morphologies were considered as an implementable path to achieve long cycle life [26,27]. Regarding Si with the highest theoretical capacity, the development trend will be detailed in Section 1.3 because of the close relation to my study.

Third, transition metal compounds such as oxides, phosphides, sulphides, and nitrides (M_xK_y; M = Fe, Co, Cu, Mn, Ni, and K = O, P, S, and N) were utilized as anodes in LIBs. The electrochemical reaction between these compounds and Li implies the reduction (oxidation) of the transition metal along with the composition (decomposition) of lithium compounds (Li_xK_y). Anodes based on the compounds exhibited high reversible capacities (500-1000 mAh g^{-1}) owing to the participation of many electrons in the conversion reactions [28-30].

The high gravimetric and volumetric energy, high power density, long cycle life and low self-discharge property [31-38] proved that LIB is the most efficient energy storage device for a wide range of portable electronics [39-45]. Beyond the dominance in this consumer electronics, the ultimate and exciting market of LIBs is the application to electric vehicles (EVs). Today, almost all major car manufacturing companies have at least either one type of hybrid EV, plug in hybrid EV, and pure EV on their product line. In 2025, 50% of all manufactured LIBs is forecasted by demand in EV sector. However, the employment of LIBs in next generation EVs needs higher safety ability than the present technology [46]. In the following section, all-solid-state LIBs (ASSLIBs) are reviewed as the solution.

1.2. All-solid-state Lithium-ion Batteries: Past and Present

Conventional LIBs as described in Section 1.1 normally use organic liquid electrolytes with low ionic resistance, leading to some drawbacks such as safety issue, insufficient lifetime, high cost, and low power density. In contrast, ASSLIBs with nonflammable inorganic solid electrolytes can avoid some of the issues, in particular, the safety concerns [47]. Therefore, ASSLIBs should be used widely in large electrical power storage systems such as EVs as well as electronic devices. In the most recent years, a significant progress has been made for ASSLIBs by optimizing solid electrolytes. Moreover, some companies have been devoted to promote the application to electronic devices and EVs. There are various ASSLIBs based on the type of inorganic solid electrolytes as below.

1) Oxynitride-based ASSLIBs
2) Sulfide-based ASSLIBs
3) NASICON-based ASSLIBs
4) Perovskite-based ASSLIBs
5) Garnet-based ASSLIBs

In this section, the author describes the advances, challenges, and prospective in ASSLIB research.

Regarding oxynitride-based ASSLIBs, thin film with lithium-phosphorous-oxynitride (LiPON) electrolyte have been extensively investigated [48-58]. Electrode, solid electrolyte, and current collectors are usually sequentially constructed on a substrate. Battery and powered electronic device must be functionally integrated with maximum efficiency and voltage control [59-68]. Lethien fabricated regular pattern with LiPON/$LiFePO_4$ thin films as the solid electrolyte/cathode for 3D micro-battery [69]. The preparation of high aspect ratio Si nanopillar (SiNPL) as anode was performed by combining deep reactive ion etching and photolithography processes. Finally, the conformal deposition of LiPON/$LiFePO_4$ bilayers was also achieved on SiNPL array by

RF sputtering. The full stack of films is only 10-15 μm in thickness. The batteries can be made into flexible when the support is thin enough [70]. Such thin film ASSLIBs with typical capacities of 0.1-5 mAh possess wide applications in sensors, RFID tags, and smarter cards [71].

Sulfides (Li_2S-P_2S_5) with high ionic conductivity and wide electrochemical windows have been demonstrated as a kind of attractive solid electrolytes [72-74]. Tatsumisago reported ASSLIB with $LiCoO_2$ and $80Li_2S$-$20P_2S_5$ glass-ceramic electrodes exhibited a long cycle performance [75]. The cell worked reversibly even at a high current density of over 10 mA cm^{-2}. Various types of Li-S ASSLIBs were also fabricated using Li_2S-P_2S_5 glass-ceramic electrolytes [76]. The batteries displayed large capacity, >1000 mAh g^{-1}. Sakuda found that sulfide electrolytes with low bond energy and a highly covalent character were beneficial in achieving high ionic conductivity [77]. Young's moduli of sulfide electrolytes fell in between those of oxides and organic polymers. Recently, Kanno reported the feasibility of $Li_{10}GeP_2S_{12}$ as solid electrolyte for practical lithium batteries [78]. The battery delivered discharge capacity of over 120 mAh g^{-1} and excellent discharge efficiency of about 100% after the second cycle. Most recently, Kato designed new solid-state electrolyte, $Li_{9.54}Si_{1.74}P_{1.44}S_{11.7}C_{10.3}$ (LSPSC), with high ionic conductivity of about 25 mS cm^{-1} [79]. The remarkably enhanced conductivity was attributed to the change of Li^+ ion transport from one dimensional to three-dimensional pathways. A cell with $LiCoO_2$ cathode, $Li_4Ti_5O_{12}$ anode, and LSPSC electrolyte could operate in a wide temperature range from -30°C to 100°C and keep about 75% capacity after 500 cycles at high-rates of charge/discharge [80]. This work represents large progress in the development of ASSLIBs.

All-solid-state lithium-air batteries (ASSLABs) with NASICON-type $18.5Li_2O$-$6.07Al_2O_3$-$37.05GeO_2$-$37.05P_2O_5$ electrolyte was built by Kumar [81]. ASSLABs with $Li_{1+x}Al_yGe_{2-y}(PO_4)_3$ solid electrolyte were also constructed by Zhou [82,83]. The discharge and charge capacities were about 1700 mAh g^{-1} and 900 mAh g^{-1}, respectively, at a current density of 500 mA g^{-1} in the voltage range of 2.0-4.2 V (vs. Li/Li^+). Symmetric cell configuration can simplify the fabrication process and reduce the interfacial issues as well as decrease manufacturing costs. Kobayashi prepared symmetric ASSLIBs with $Li_3V_2(PO_4)_3$ electrodes and $Li_{1.5}Al_{0.5}Ge_{1.5}(PO_4)_3$ electrolyte [84]. $Li_{1.5}Al_{0.5}Ge_{1.5}(PO_4)_3$ was added into the electrode to increase the interface area between active materials and electrolyte. The discharge capacity could reach 92 mAh g^{-1} at a current density of 22 μA cm^{-2} at 80 °C, and 38 mAh g^{-1} at 25 °C, respectively. Iriyama fabricated new kind of ASSLIB thin film with $Cu/Li_2O-Al_2O_3-TiO_2-P_2O_5$-based glass ceramics sheet/amorphous Li-Mn-O/Pt by applying high DC voltage [85]. The obtained battery could perform stable charge/discharge reaction at 1.4 V.

Perovskite $Li_{0.35}La_{0.55}TiO_3$ (LLTO) with high ionic conductivities of 10^{-3}-10^{-4} S cm^{-1} was used as the electrolytes for three-dimensional ASSLIBs [86-90]. Here LLTO possess honeycomb structure which has micro-sized holes on both sides of membrane. The impregnation of $LiCoO_2$ and $Li_4Mn_5O_{12}$ particles mixed with precursor sol into honeycomb holes enabled good contact between LLTO electrolyte and active material [91]. $LiCoO_2$/LLTO/$Li_4Mn_5O_{12}$ ASSLIB was successfully operated at 1.1 V with a discharge capacity of 7.3 μAh cm^{-2}. Thin films with amorphous lithium lanthanum titanate solid electrolyte were fabricated by e-beam evaporation under a higher power [92]. Li/LiPON/LLTO/$LiCoO_2$ cell with LLTO thin film as solid electrolyte showed the capacity degradation of 0.5% per cycles after 100 cycles at 7 μA cm^{-2}.

Garnet-type $Li_7La_3Zr_2O_{12}$ (LLZO) was explored as solid electrolyte for ASSLIBs with Li metal anode [93]. Cyclic voltammogram of Li/LLZO/Li cell showed that the dissolution and decomposition reactions of lithium reversibly occurred without any reaction with LLZO [94]. Full cell composed of $LiCoO_2$/LLZO/Li configuration was successfully operated at the expected voltage estimated from redox potential of Li and $LiCoO_2$. The discharge capacity of full cell was 15 μAh cm^{-2}. However, an irreversible behavior was observed at the first discharge and charge cycle due to the interfacial issue between $LiCoO_2$ and LLZ. The electrochemical performance and charge transfer resistance of $LiCoO_2/Li_{6.75}La_3Zr_{1.75}Nb_{0.25}O_{12}/Li$ ASSLIB was measured by Ohta [95].

The interfacial resistance between LCO and LLZONb was comparable to that of LIBs with liquid organic electrolytes. This battery showed capacity retention of approximately 98% after 100 cycles. Li^+ ion conductor Li_3BO_3 (LBO) was used as buffer layer between $LiCoO_2$ active cathode material and Nb doped $Li_7La_3Zr_2O_{12}$ (LLZONb) electrolyte [96]. Sufficient interface contact could be easily achieved with sintering LBO into the cathode layer by annealing process. The obtained battery exhibited good electrochemical performance and lower interfacial resistance. Guo prepared Ta-doped $Li_7La_3Zr_2O_{12}$ electrolyte for ASSLIBs [97]. The battery shows the first discharge capacity of 150 mAh g^{-1} at 0.05 C and 93% capacity retention after 100 cycles at 60 °C. The performance can be further improved by increasing temperature up to 100 °C. These results indicate that the lamellar garnet-type ceramic electrolytes are promising for developing high-performance ASSLIBs operating at intermediate temperatures. Guo examined the effect of moisture on Li^+ ion conduction of $Li_7La_3Zr_2O_{12}$ ceramic and the electrochemical properties of LLZ-based solid state battery with $LiFePO_4$ (LFP) film cathode [98]. The secondary phase was observed in LLZ ceramic, when the specimen was exposed to humid air. $Li_7La_3Zr_2O_{12}$-based Li-rich garnets tend to react with water and CO_2 in air to form Li^+ ion insulating Li_2CO_3 layer on the surface of garnet particles, leading to large interfacial resistance for Li^+ ion transfer. Goodenough et al. found adding 2 wt% LIF to garnet $Li_{6.5}La_3Zr_{1.5}Ta_{0.5}O_{12}$ can effectively increase the stability of garnet electrolyte against moist air [99]. Therefore, the protection of LLZ ceramic from moisture is necessary to gain high performance LLZ-based solid state cell at room temperature.

Due to safety concerns of current LIBs, there are huge market needs for ASSLIBs. However, it still takes a long time for the practical use, despite considerable advances described above. The challenges hindering the commercialization is the enhancement of storage capacity and energy density. In the next section, the studies on Si anodes are reviewed as the most promising method to meet the energy demands.

1.3. Si Anodes: Past and Present

LIBs have remarkable advantages in cycle life and weight energy density in comparison with other energy storage devices. Therefore, the related technologies are the key of the contemporary energy system which is closely coupled with renewable energy generation, transmission and utilization [100-103]. However, current LIBs cannot meet the ever-increasing energy demands [104,105]. Thus, a lot of new electrode materials with different storage mechanisms have been explored to improve the battery performance [106-109]. Among such advanced candidates, Si is the most promising as an anode active material mainly for the following reasons [110-112]: high theoretical capacity, low operating potential, and abundance in nature. The theoretical capacity, TC, can be calculated by a following equation:

$$TC = \frac{(n \times F)}{MW}$$

where n is the number of electrons involved in the reaction of 1 mol active material. F and MW are Faraday's constant (26801 mAh/mol) and molar weight of active material, respectively. For example, in the case of $Li_{22}Si_5$ phase, the lithiation process is expressed by a following reaction equation:

$$22Li^+ + 5Si + 22e^- = Li_{22}Si_5$$

Therefore,

$$n = \frac{22}{5} = 4.4$$

Since MW is 28.084 (atomic weight of Si), TC can be calculated as follows:

$$TC = \frac{(4.4 \times 26801)}{28.084} = 4199\ mAh\ g^{-1}$$

Table 1-1 summarizes TCs of several crystalline Li-Si phases, which are calculated using the same formula.

For application of Si as anode for LIBs, it is important to understand the details of Li-Si phase diagram. As shown in Figure 1-1 [113], thermodynamic process forms a series of Li-Si alloy phases, such as LiSi, $Li_{12}Si_7$, $Li_{13}Si_4$, $Li_{15}Si_4$, and $Li_{22}Si_5$. However, there is clearly some differences in electrochemical process. Liu found that the lithiation of Si is the ledge peeling of Si (111) facet by Li^+ ions, which produces amorphous Li_xSi layer by layer [114]. Namely, initial products in electrochemical lithiation process are always amorphous Li_xSi (with $0<x<3.75$), though the crystalline phases normally have lower Gibbs free energy than the amorphous counterparts. The thickness of amorphous layer gradually increases with uniform distribution of Li. Then the amorphous phase suddenly crystallizes to form $Li_{15}Si_4$ at $x=3.75$ [115]. During the crystallization, no fluctuations are seen in the composition and volume. Density functional theory calculations and in-situ transmission electron microscope, TEM, measurements indicated that the amorphous Li_xSi crystallizes through spontaneous congruent phase transformation process without long-distance atomic diffusion. This mechanism differs from nucleation and growth in thermal equilibrium process.

The lithiation mechanism of Si is associated with massive volume changes. The expansion coefficient of crystalline Li-Si phase, for example, $Li_{22}Si_5$, to Si can be calculated through following process.

i) unit cell density and unit cell volume are determined using database [116]

density: 1.2 g cm^{-3}

volume: 1.60239×10^{-21} cm^3

Table 1-1. Theoretical capacities of several crystalline Li-Si phases.

Crystalline Phase	$Li_{22}Si_5$	$Li_{15}Si_4$	$Li_{13}Si_4$	$Li_{12}Si_7$	LiSi
Theoretical Capacity (mAh g^{-1})	4199	3579	3102	1636	954

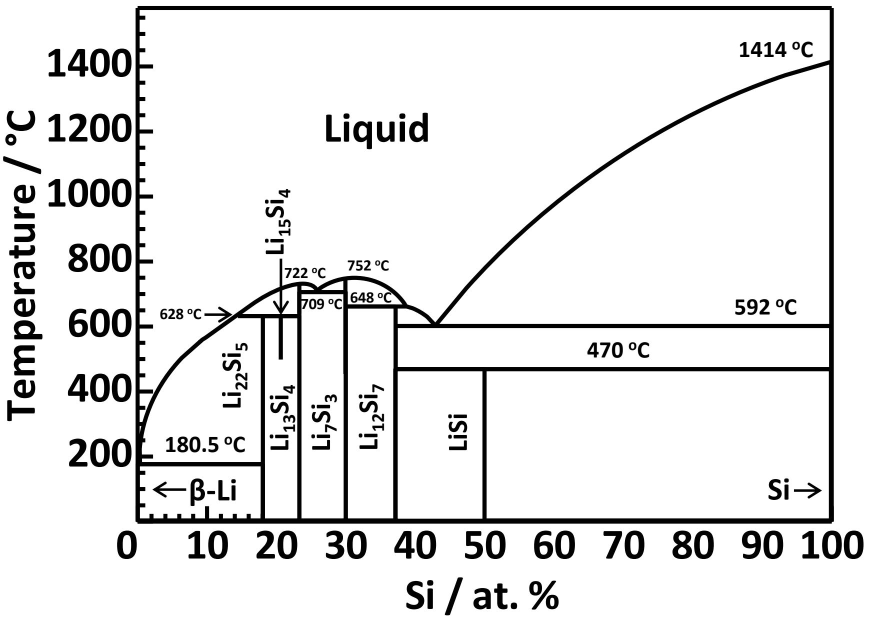

Figure 1-1. Li-Si phase diagram.

ii) weight of a single $Li_{22}Si_5$ is obtained using Avogadro constant and atomic weight

$$\frac{(6.938 \times 22 + 28.084 \times 5)}{6 \times 10^{23}} = 4.88427 \times 10^{-22}\ g$$

iii) number of a single $Li_{22}Si_5$ in unit cell is obtained using an above calculated value, unit cell density, and unit cell volume

$$\frac{1.2 \times (1.60239 \times 10^{-21})}{4.88427 \times 10^{-22}} = 3.93686$$

iv) number of Si atom in unit cell is obtained using an above calculated value

$$3.93686 \times 5 = 19.6843$$

v) volume of a single $Li_{4.4}Si$ is obtained using an above calculated value and unit cell volume

$$\frac{(1.60239 \times 10^{-21})}{19.6843} = 8.14044 \times 10^{-23}\ cm^3$$

vi) expansion coefficient is obtained using an above calculated value and volume of a single Si (2.05292×10^{-23} cm^3)

$$\frac{8.14044 \times 10^{-23}}{2.05292 \times 10^{-23}} = 3.965$$

Table 1-2 summarizes the expansion coefficients of several crystalline Li-Si phases,

Table 1-2. Expansion coefficients of several crystalline Li-Si phases.

Crystalline Phase	$Li_{22}Si_5$	$Li_{15}Si_4$	$Li_{13}Si_4$	$Li_{12}Si_7$	LiSi
Expansion Coefficient	3.965	3.63	3.237	2.094	1.537

which are calculated using the same method.

The large expansion demonstrated by above calculation causes three main challenges to the practical use of Si anodes. First, the cycle life is short because the decomposition proceeds by the large volume change with the storage and release of Li^+ ion. Second, the pulverization of entire electrode in the alloying/dealloying process causes rapid and irreversible capacity reduction and low Coulomb efficiency (CE). Finally, as solid electrolyte interphase (SEI) breaks due to the delithiation, SEI thickness increases with cycle number, resulting in the decrease of reversible capacity [117,118]. Tremendous strategies for the issues listed above are follows:

1) downsizing at various dimensions [119-124]
2) compositing with C [125-131]
3) compositing with metal [132-135]
4) compositing with metal oxides [136-139]

In this section, the author describes the advances, challenges, and prospective in Si anodes for LIBs with liquid electrolytes.

Regarding downsizing, various nanostructures with different dimensions have been designed to improve the electrochemical performance:

a) 0 dimensional: nanoparticles
b) 1 dimensional: nanowires
c) 2 dimensional: nanosheets and silicene
d) 3 dimensional: hierachical nanostructure, hollow, and porous structures

Turning to nanoscale is an efficient strategy to overcome the large expansion/contraction problem by relieving internal strain. Kim prepared well-dispersed 0D nanoparticles with various sizes by reverse micelle method [140]. The capacity was maintained at 2700 mAh g^{-1} after 40 cycles at 0.2 C. The highest charge capacity was obtained at a diameter of 10 nm. Using in-situ TEM technology, Liu found that nanoparticles exhibited stronger resistance to mechanical strain at a critical size of 150 nm [141]. Recently, Lin prepared crystalline nanoparticles through a reduction of micro-sized Si zeolite by metallic Al in molten $AlCl_3$ at 200°C [142]. LIBs with Si crystalline nanoparticles reached reversible capacities of 2663 mAh g^{-1} at 0.5 A g^{-1} after 50 cycles and 870 mAh g^{-1} at 3 A g^{-1} after 1000 cycles. In 2007, Cui fabricated 1D nanowires with a diameter of 90 nm vertically aligned on stainless steel substrate by chemical vapor deposition [143]. The improved LIB performance was ascribed to the sufficient space between nanowires to release the strain from large volume change. Very recently, Wang produced nanowire film using magnetron sputtering with electroless etching technology. The anode delivered an initial reversible discharge capacity of 3158 mAh g^{-1} and maintained a capacity of 2840 mAh g^{-1} after 100 cycles at 200 mA g^{-1} [144]. 2D materials possess smaller specific variable SEI surface area compared to other dimensional nanostructures. Chen synthesized ultrathin mesoporous nanosheets by soft template [145]. Owing to ultrathin 2D characteristics and mesoporous structure, the nanosheets buffered the structural stress, resulting in superior cycle performance. Lately, scalable preparation of freestanding high-quality silicene via liquid oxidation and exfoliation of $CaSi_2$ was reported by Liu [146]. The obtained silicene exhibited an extraordinary cycling stability with no capacity decay after 1800 cycles. Well-crystallized hierarchical mesoporous Si was synthesized through the magnesiothermic reduction process using 0D Si particles as self-template [147]. The 3D nanostructure exhibited a reversible capacity of 959 mAh g^{-1} was retained after 300 cycles at 0.2 A g^{-1} with a high mass loading density of 1.4 mg cm^{-2}. Xiao combined magnesiothermal reduction and acid etching method to synthesize hollow porous nanospheres [148]. In-situ TEM demonstrated that both the mesoporous shell and hollow internal void relieved inward expansion and contraction during lithiation and delithiation.

Second, C uniformly coated on Si with various structures becomes a promising approach to improve the electrochemical performance [149,150]. Encapsulation of polybenzimidazole onto microsized Si spheres was achieved by an aerosol-assisted assembly combined with physisorption process [151]. Si-C composite exhibited high reversible specific capacity (2172 mAh g^{-1}), superior rate capability (1186 mAh g^{-1} at 5 A g^{-1}) and prolonged cycle life. Guo fabricated porous Si nanoparticles loaded in controllable void C spheres with yolk-shell structure by combining hydrothermal water etching and magnesiothermic reduction strategy [152]. The optimized composite showed excellent LIB performance, delivering a capacity of 1400 mAh g^{-1} after 100 cycles at 0.2 A g^{-1}. Moreover, Chen fabricated double C shells with certain inter spaces by CVD and magnesiothermic reduction method [153]. The inner C shell provided certain voids to withstand volume changes. Compared with bare Si and single C layer coated Si electrodes, the composite electrode possessed superior rate capability and good cycling performance up to 1000 cycles. An et al. reported a scalable top-down technique to produce ant-nestlike porous Si [154]. Synchrotron radiation tomographic reconstruction images and in-situ TEM characterization reveal that the unique structure could prevent pulverization and accommodate volume expansion during cycling. The C-coated porous Si anode delivered a high capacity of 1271 mAh g^{-1} with 90% capacity retention after 1000 cycles. Li reported an efficient approach to large-area fabrication of 3D graphene-Si networks with good flexibility and high electrical conductivity [155]. These properties are beneficial to minimizing the volume change of Si and facilitating the diffusions of both lithium and electron. As the results, 3D network exhibited a superior rate capability, cyclability and high reversible capacity over 2050 mAh g^{-1} after 200 cycles.

Third, as metal composites, Song delivered a template-free synthesis of highly connected hollow Si-Cu nanotubes [156]. CuO was firstly grown on the copper foam by a thermal oxidation treatment. Then, coating amorphous Si on CuO nanowires was achieved via a plasma-enhanced CVD technology. Finally, hollow Si-Cu nanotubes were obtained by an in-situ H_2 annealing. The resulting anode possessed a high specific capacity of 780 mAh g^{-1} after 1000 cycles, with a capacity retention rate of 88%. Recently, 3D nanoporous Si-Ge alloy with tunable morphology and porosity was synthesized by a dealloying method with a ternary AlSiGe ribbon as the precursor [157]. By adjusting the Al content in the precursor, the morphology and porosity could be controlled. With an Al content of 80%, 3D alloy with hierarchical micropores delivered a high reversible capacity of 1158 mAh g^{-1} after 150 cycles. Zhang developed a composite anode of

Cu/Si/Ge nanowire arrays, where each nanowire consisted of a core of Cu segments and a Si/Ge bilayer shell [158]. This unique electrode architecture exhibited several favorable properties: nanowires enabled facile strain relaxation; free space between nanowires and hollow space between Cu segments accommodated volume expansion; core Cu segments enhanced electron transport. Moreover, the outer Ge shell also served as an active high-capacity coating. By using in-situ TEM and electrochemical testing, a novel co-lithiation/co-delithiation reaction mechanism was proposed, which effectively alleviated the electrochemically induced mechanical degradation and thus greatly enhanced the long cycle stability of the electrode.

Finally, regarding metal oxide composites, Fang reported a rational design of core-shell structure with Si nanoparticles encapsulated in TiO_2 hollow spheres by combination of hydrolysis with magnesiothermic reduction method [159]. In this architecture, the inside void provided enough space for accommodation of the volume expansion. In addition, the robust TiO_2 shell could improve the electrical conductivity and prevent the direct contact of Si with the electrolyte. As a result, the hollow nanospheres maintained a specific capacity of 804 mAh g^{-1} after 100 cycles. Lately, a facile sol-gel strategy was proposed to synthesize core-shell Si@amorphous TiO_2 (~3 nm) by Yang [160]. STEM and the elemental mapping characterizations clearly verified that a thin TiO_2 nanograin layer was conformally coated on Si nanoparticle core. The amorphous TiO_2 shell offered superior buffering properties over the pristine Si nanoparticles and crystalline TiO_2 layers coated Si for unprecedented cycling stability. More recently, Wang reported thermally alloy lithiation approach to prepare the lithiated TiO_2 protecting Li_xSi nanoparticles [161]. The robust lithiated TiO_2 matrix not only improved the electrical conductivity but also spatially limited the direct SEI formation during cycling. More importantly, the coating layer protected the most inner Li_xSi alloys from corrosion, leading to high dry-air stability. As a result, the anode achieved a capacity of about 1300 mAh g^{-1} after 500 cycles.

1.4. Purpose of This Study

The goal of this study is to enhance the energy density of ASSLIBs by using Si anodes. To accommodate the volume expansion of Si, which is a serious problem in the practical use, this thesis focuses on the fusion of nanosizing and compositing. Specifically, nanoporous Si particles are adopted as the anode active material. This is because nano-sized pores are expected to act as the buffer regions for large volume change. In addition, sulfide-based solid electrolyte is used as a counterpart to prepare the composite anodes. The sulfide should have excellent adhesion with Si particles due to its low Young's modulus [162]. To the best of my knowledge, the approach described above is a novel attempt in ASSLIBs. It is also worth noting that there are the advantages in the manufacturing cost and handling compared to other Si anodes. In this dissertation, I report the fabrication of nanoporous Si composite anodes and their application to sulfide-based ASSLIBs.

1.5. Contents of This Thesis

This doctoral thesis consists of the following five chapters.

Chapter 1

This chapter describes the background and the contents of this thesis.

Chapter 2

In Chapter 2, I describe the preparation and the structural characteristics of nanoporous Si particles. Si particles were prepared by three processes: air oxidation of Mg_2Si ($Mg_2Si + O_2 \rightarrow Si + 2MgO$) and Mg_2Si reduction of mesoporous SiO_2 or SiO_2 fumes ($SiO_2 + Mg_2Si \rightarrow 2Si + 2MgO$). The crystal structure of the prepared Si particles was confirmed to be diamond cubic by X-ray diffraction (XRD) and Raman scattering measurements. Using field emission scanning electron microscopy (FE-SEM) and TEM, nano-sized pores were observed on the surface and inside of Si particles. Specific surface area (~300-500 nm) and pore size (<10 nm) were analyzed by Brunauer-Emmett-Teller (BET) measurements. In addition, the oxidation state of the Si surface was quantitatively evaluated using x-ray photoelectron spectroscopy (XPS). Based on all the experimental results, it was concluded that Mg_2Si reduction of SiO_2 provided highly-pure nanoporous Si particles compared to the air oxidation of Mg_2Si.

Chapter 3

In Chapter 3, I describe the electrochemical characteristics of ASSLIBs with various Si composite anodes. Anode composite materials consisted of nanoporous Si paricles, $75Li_2S \cdot 25P_2S_5$ solid electrolyte (SE), and acetylene black. To fabricate ASSLIBs with half cell configuration, the anode composite material, SE powder, and Li-In counter electrode were sequentially stacked in an electric insulation tube. The capacity retention of nanoporous Si half cell was much larger than that of non-porous Si half cell. Based on the cross-sectional SEM images and electrochemical impedance profiles, the high capacity retention was caused by the closely-contact between nanoporous Si particles/aggregates and SE. This indicates that the shrinkage of pores buffers the volumetric expansion of Si. In addition, the elasticity of sulfied-based SE relieves the strains arising from the slightly expanded Si particles. Using oxidation state, particle size, pore size, and dispersibility of Si particles as parameters, the capacities, coulombic efficiencies, and capacity retentions were compared among three kinds of half cells.

Chapter 4

From the practical point of view, in Chapter 4, I describe the optimization of conduction path using conductive additive and the quantitative evaluation of structural stress using full cell configuration. Anode composite materials were prepared with the weight ratio of nanoporous Si particles:SE:conductive additive=4:6:x (x=1, 2, 3, and 4). The electrical conductivity and charge capacity simply increased with the concentration of conductive additive. On the other hand, there was an optimum amount of conductive additive for cycle performance. Full cells were composed of composite cathode with $LiNi_{1/3}Mn_{1/3}Co_{1/3}O_2$:SE:conductive additive=70:30:5 wt% and composite anode with nanoporous Si particles:SE:conductive additive=40:60:10 wt%. The load change was extremely small during charge and discharge. In addition, no cracks were observed in the cross-sectional SEM and EDX images of electrodes. It was concluded that nanoporous structure acted as the buffer regions for large volume change of Si particles/aggregates during charge and discharge.

Chapter 5

This chapter summarizes all the conclusions in this thesis.

References

[1] M. S. Whittingham, *J. Electrochem. Soc.*, **123** (1976) 315-320.

[2] D. W. Murphy, J. Broadhead, and B. C. H. Steele, eds., *Materials for Advanced Batteries*, Plenum Press, New York (1980).

[3] M. Lazzari and B. Scrosati, *J. Electrochem. Soc.*, **127** (1980) 773-774.

[4] K. Mitzushima, P. C. Jones, P. J. Wiseman, and J. Goodenough, *Mater. Res. Bull.*, **15** (1980) 783-789.

[5] A. Yoshino, K. Sanechika, and T. Nakajima, "Secondary battery", *USP 4,668,595*, 1987-05-26.

[6] T. H. Park, J. S. Yeo, M. H. Seo, J. Miyawaki, I. Mochida, and S. H. Yoon, *Electrochim. Acta*, **93** (2013) 236-240.

[7] Y. Nishi, *Chem Rec*, **1** (2001) 406-413.

[8] Y. Nishi, *J. Power Sources*, **100** (2001) 101-106.

[9] C. C. Li and Y. W. Wang, *J. Power Sources*, **227** (2013) 204-210.

[10] S. Boyanov, K. Annou, C. Villevieille, M. Pelosi, D. Zitoun, and L. Monconduit, *Ionics*, **14** (2008) 183-190.

[11] M. Yashio, H. Wang, K. Fukuda, T. Umeno, T. Abe, and Z. Ogumi, *J. Mater. Chem.*, **14** (2004) 1754-1758.

[12] O. Haik, S. Ganin, G. Gershinsky, E. Zinigrad, B. Markovsky, D. Aurbach, and I. Halalay, *J. Electrochem. Soc.*, **158** (2011) A913-A923.

[13] H. Wang, M. Yoshio, T. Abe, and Z. Ogumi, *J. Electrochem. Soc.*, **149** (2002) A499-A503.

[14] M. Yoshio, H. Wang, K. Fukuda, Y. Hara, and Y. Adachi, *J. Electrochem. Soc.*, **147** (2000) 1245-1250.

[15] I. R. M. Kottegoda, Y. Kadoma, H. Ikuta, Y. Uchimoto, and M. Wakihara, *Electrochem. Solid-State Lett.*, **5** (2002) A275-A278.

[16] L. Qiao, X. Sun, Z. Yang, X. Wang, Q. Wang, and D. He, *Carbon*, **54** (2013) 29-35.

[17] F. Orsini, A. Pasquier, B. Beaudouin, J. M. Tarascon, M. Trentin, N. Langenhuizen, E. Beer, and P. Notten, *J. Power Sources*, **81-82** (1999) 918-921.

[18] B. J. Landi, M. J. Ganter, C. D. Cress, R. A. DiLeo, and R. P. Raffaelle, *Energy Environ. Sci.*, **2** (2009) 638-654.

[19] C. Kim, K. S. Yang, M. Kojima, K. Yoshida, Y. J. Kim, Y. A. Kim, and M. Endo, *Adv. Funct. Mater.*, **16** (2006) 2393-2397.

[20] J. Hou, Y. Shao, M. W. Ellis, R. B. Moore, and B. Yi, *Phys. Chem. Chem. Phys.*, **13** (2011) 15384-15402.

[21] G. Cui, L. Gu, L. Zhi, N. Kaskhedikar, P. A. Aken, K. Mullen, and J. Maier, *Adv. Mater.*, **20** (2008) 3079-3083.

[22] S. L. Candelaria, Y. Shao, W. Zhou, X. Li, J. Xiao, J. G. Zhang, Y. Wang, J. Liu, J. Li, and G. Cao, *Nano Energy*, **1** (2012) 195-220.

[23] A. L. M. Reddy, S. R. Gowda, M. M. Shaijumon, and P. M. Ajayan, *Adv. Mater.*, **24** (2012) 5045-5064.

[24] C. M. Park, J. H. Kim, H. Kim, and H. J. Sohn, *Chem. Soc. Rev.*, **39** (2010) 3115-3141.

[25] W. J. Zhang, *J. Power Sources*, **196** (2011) 13-24.

[26] H. Zhang and P. V. Braun, *Nano Lett.*, **12** (2012) 2778-2783.

[27] J. Gu, S. M. Collins, A. I. Carim, X. Hao, B. M. Bartlett, and S. Maldonado, *Nano Lett.*, **12** (2012) 4617-4623.

[28] L. Ji, Z. Lin, M. Alcoutlabi, and X. Zhang, *Energy Environ. Sci.*, **4** (2011) 2682-2699.

[29] X. Li and C. Wang, *J. Mater. Chem. A*, **1** (2013) 165-182.

[30] P. Poizot, S. Laruelle, S. Grugeon, and J. M. Tarascon, *J. Electrochem. Soc.*, **149** (2002) A1212-A1217.

[31] R. Marom, S. F. Amalraj, N. Leifer, D. Jacob, and D. Aurbach, *J. Mater. Chem.*, **21** (2011) 9938-9954.

[32] G. A. Nazri and G. Pistoia, eds., *Lithium Batteries: Science and Technology*,

Springer, Berlin (2003).

[33] G. Girishkumar, B. McCloskey, A. C. Luntz, S. Swanson, and W. Wilcke, *J. Phys. Chem. Lett.*, **1** (2010) 2193-2203.

[34] B. Scrosati and J. Garche, *J. Power Sources*, **195** (2010) 2419-2430.

[35] M. Armand and J. M. Tarascon, *Nature*, **451** (2008) 652-657.

[36] T. H. Kim, J. S. Park, S. K. Chang, S. Choi, J. H. Ryu, and H. K. Song, *Adv. Energy Mater.*, **2** (2012) 860-872.

[37] J. B. Goodenough and K. S. Park, *J. Am. Chem. Soc.*, **135** (2013) 1167-1176.

[38] V. Etacheri, R. Marom, R. Elazari, G. Salitra, and D. Aurbach, *Energy Environ. Sci.*, **4** (2011) 3243-3262.

[39] M. Winter and R.J. Brodd, *Chem. Rev.*, **104** (2004) 4245-4270.

[40] F. Cheng, J. Liang, Z. Tao, and J. Chen, *Adv. Mater.*, **23** (2011) 1695-1715.

[41] H. Li, Z. Wang, L. Chen, and X. Huang, *Adv. Mater.*, **21** (2009) 4593-4607.

[42] J. B. Goodenough and Y. Kim, *Chem. Mater.*, **22** (2009) 587-603.

[43] J. M. Tarascon and M. Armand, *Nature*, **414** (2001) 359-367.

[44] B. Xu, D. Qian, Z. Wang, and Y. S. Meng, *Mater. Sci. Eng. R Rep.*, **73** (2012) 51-65.

[45] J. Li, J. K. Barillas, C. Guenther, and M. A. Danzer, *J. Power Sources*, **230** (2013) 244-250.

[46] M. M. Thackeray, C. Wolverton, and E. D. Isaacs, *Energy Environ. Sci.*, **5** (2012) 7854-7863.

[47] J. B. Bates, N. J. Dudney, B. Neudecker, A. Ueda, and C. D. Evans, *Solid State Ion.*, **135** (2000) 33-45.

[48] J. W. Long, B. Dunn, D. R. Rolison, and H. S. White, *Chem. Rev.*, **104** (2004) 4463-4492.

[49] B. J. Neudecker, N. J. Dudney, and J. B. Bates, *J. Electrochem. Soc.*, **147** (2000) 517-523.

[50] S. H. Lee, P. Liu, and C. E. Tracy, *Electrochem. Solid-State Lett.*, **6** (2003) A275-

A277.

[51] N. J. Dudney and Y.I. Jang, *J. Power Sources*, **119** (2003) 300-304.

[52] N. J. Dudney, *Mater. Sci. Eng. B*, **116** (2005) 245-249.

[53] M. Baba, N. Kumagai, H. Fujita, K. Ohta, K. Nishidte, S. Komaba, B. Kaplan, H. Groult, and D. Devilliers, *J. Power Sources*, **119–121** (2003) 914-917.

[54] Y. S. Park, S. H. Lee, B. I. Lee, and S. K. Joo, *Electrochem. Solid-State Lett.*, **2** (1999) 58-59.

[55] Y. Iriyama, T. Kako, C. Yada, T. Abe, and Z. Ogumi, *Solid State Ion.*, **176** (2005) 2371-2376.

[56] Y. Iriyama, K. Nishimoto, C. Yada, T. Abe, Z. Ogumi, and K. Kikuchi, *J. Electrochem. Soc.*, **153** (2006) A821-A825.

[57] X. Yu, J. B. Bates, G. E. Jellison Jr., and F. X. Hart, *J. Electrochem. Soc.*, **144** (1997) 524-532.

[58] B. Wang, J. B. Bates, F. X. Hart, B. C. Sales, R. A. Zuhr, and J. D. Robertson, *J. Electrochem. Soc.*, **143** (1996) 3203-3213.

[59] N. J. Dudney and B. J. Neudecker, *Curr. Opin. Solid State Mater. Sci.*, **4** (1999) 479-482.

[60] M. A. Hickner, *Mater. Today*, **13** (2010) 34-41.

[61] N. Kuwata, J. Kawamura, K. Toribami, T. Hattori, and N. Sata, *Electrochem. Commun.*, **6** (2004) 417-421.

[62] S. Lee, P. Liu, C. E. Tracy, and D. K. Benson, *Electrochem. Solid-State Lett.*, **2** (1999) 425-427.

[63] Y. Park, S. Lee, B. Lee, and S. Joo, *Electrochem. Solid-State Lett.*, **2** (1999) 58-59.

[64] S. Zhao, Z. Fu, and Q. Qin, *Thin Solid Films*, **415** (2002) 108-113.

[65] S. Kakuda, T. Momma, T. Osaka, G. B. Appetecchi, and B. Scrosati, *J. Electrochem. Soc.*, **142** (1995) L1-L2.

[66] M. Baba, N. Kumagai, H. Kobayashi, O. Nakano, and K. Nishidate, *Electrochem. Solid-State Lett.*, **2** (1999) 320-322.

[67] S. Ohta, S. Komagata, J. Seki, T. Saeki, S. Morishita, and T. Asaoka, *J. Power Sources*, **238** (2013) 53-56.

[68] N. Ohta, K. Takada, L. Zhang, R. Ma, M. Osada, and T. Sasaki, *Adv. Mater.*, **18** (2006) 2226-2229.

[69] C. Lethien, M. Zegaoui, P. Roussel, P. Tilmant, N. Rolland, and P. A. Rolland, *Microelectron. Eng.*, **88** (2011) 3172-3177.

[70] N. J. Dudney, *Electrochem. Soc. Interface*, (2008) 44-48.

[71] W. C. West, J. F. Whitacre, V. White, and B. V. Ratnakumar, *J. Micromech. Microeng.*, **12** (2002) 58-62.

[72] M. Tatsumisago, M. Nagao, and A. Hayashi, *J. Asian Ceram. Soc.*, **1** (2013) 17-25.

[73] M. Tatsumisago, F. Mizuno, and A. Hayashi, *J. Power Sources*, **159** (2006) 193-199.

[74] H. Muramatsu, A. Hayashi, T. Ohtomo, S. Hama, and M. Tatsumisago, *Solid State Ion.*, **182** (2011) 116-119.

[75] M. Tatsumisago and A. Hayashi, *Solid State Ion.*, **225** (2012) 342-345.

[76] M. Nagao, A. Hayashi, and M. Tatsumisago, *Electrochim. Acta*, **56** (2011) 6055-6059.

[77] A. Sakuda, A. Hayashi, and M. Tatsumisago, *Sci. Rep.*, **3-2261** (2013) 1-5.

[78] N. Kamaya, K. Homma, Y. Yamakawa, M. Hirayama, R. Kanno, M. Yonemura, T. Kamiyama, Y. Kato, S. Hama, K. Kawamoto, and A. Mitsui, *Nat. Mater.*, **10** (2011) 682-686.

[79] Y. Kato, S. Hori, T. Saito, K. Suzuki, M. Hirayama, A. Mitsui, M. Yonemura, H. Iba, and R. Kanno, *Nat. Energy*, **1** (2016) 16030-16032.

[80] K. Minami, A. Hayashi, S. Ujiie, and M. Tatsumisago, *Solid State Ion.*, **192** (2011) 122-125.

[81] B. Kumar, J. Kumar, R. Leese, J. P. Fellner, S. J. Rodrigues, and K. M. Abraham, *J. Electrochem. Soc.*, **157** (2010) A50-A54.

[82] H. Kitaura and H. Zhou, *Energy Environ. Sci.*, **5** (2012) 9077-9084.

[83] F. Li, H. Kitaura and H. Zhou, *Energy Environ. Sci.*, **6** (2013) 2302-2311.

[84] E. Kobayashi, L. S. Plashnitsa, T. Doi, S. Okada, and J. Yamaki, *Electrochem. Commun.*, **12** (2010) 894-896.

[85] Y. Iriyama, C. Yada, T. Abe, Z. Ogumi, and K. Kikuchi, *Electrochem. Commun.*, **8** (2006) 1287-1291.

[86] Y. Lin, J. Li, K. Liu, Y. X. Liu, J. Liu, and X. M. Wang, *Green Chem.*, **18** (2016) 3796-3803.

[87] K. Takada, *Acta Mater.*, **61** (2013) 759-770.

[88] Y. Inaguma, L. Chen, M. Itoh, T. Nakamura, T. Uchida, H. Ikuta, and M. Wakihara, *Solid State Commun.*, **86** (1993) 689-693.

[89] T. Abe, M. Ohtsuka, F. Sagane, Y. Iriyama, and Z. Ogumi, *J. Electrochem. Soc.*, **151** (2004) A1950-A1953.

[90] O. Bohnke, *Solid State Ion.*, **179** (2008) 9-15.

[91] M. Kotobuki, Y. Suzuki, H. Munakata, K. Kanamura, Y. Sato, K. Yamamoto, and T. Yoshida, *J. Electrochem. Soc.*, **157** (2010) A493-A498.

[92] M. Kotobuki, Y. Suzuki, H. Munakata, K. Kanamura, Y. Sato, K. Yamamoto, and T. Yoshida, *J. Power Sources*, **195** (2010) 5784-5788.

[93] K. Fu, Y. Gong, J. Dai, A. Gong, X. Han, Y. Yao, C. Wang, Y. Wang, Y. Chen, C. Yan, Y. Li, E. D. Wachsman, and L. Hu, *Proc. Natl. Acad. Sci. USA*, **113** (2016) 7094-7099.

[94] M. Kotobuki, H. Munakata, K. Kanamura, Y. Sato, and T. Yoshida, *J. Electrochem. Soc.*, **157** (2010) A1076-A1079.

[95] S. Ohta, T. Kobayashi, J. Seki, and T. Asaoka, *J. Power Sources*, **202** (2012) 332-335.

[96] S. Ohta, S. Komagata, J. Seki, T. Saeki, S. Morishita, and T. Asaoka, *J. Power Sources*, **238** (2013) 53-56.

[97] F. Du, N. Zhao, Y. Li, C. Chen, Z. Liu, and X. Guo, *J. Power Sources*, **300** (2015) 24-28.

[98] C. Ahn, J. Choi, J. Ryu, B. Hahn, J. Kim, W. Yoon, J. Choi, J. Lee, and D. Park, *J. Power Sources*, **272** (2014) 554-558.

[99] Y. Li, B. Y. Xu, H. H. Xu, H. N. Duan, X. J. Lv, S. Xin, W. D. Zhou, L. G. Xue, G. T. Fu, A. Manthiram, and J. B. Goodenough, *Angew. Chem. Int. Ed.*, **56** (2017) 753-756.

[100] J. Chen and F. Cheng, *Acc. Chem. Res.*, **42** (2009) 713-723.

[101] K. Zhang, Z. Hu, Z. Tao, and J. Chen, *Sci. China Mater.*, **57** (2014) 42-58.

[102] R. Schmuch, R. Wagner, G. Hörpel, T. Placke, and M. Winter, *Nat. Energy*, **3** (2018) 267-278.

[103] J. Hao, H. Liu, Y. Ji, and S. Bi, *Sci. China Mater.*, **60** (2017) 315-323.

[104] F. Cheng, J. Liang, Z. Tao, and J. Chen, *Adv. Mater.*, **23** (2011) 1695-1715.

[105] Y. Lu, Q. Zhang, and J. Chen, *Sci. China Chem.*, **62** (2019) 533-548.

[106] S. Zheng, H. Sun, B. Yan, J. Hu, and W. Huang, *Sci. China Mater.*, **61** (2018) 1285-1290.

[107] Y. Lu, X. Hou, L. Miao, L. Li, R. Shi. L. Liu, and J. Chen, *Angew. Chem. Int. Ed.*, **58** (2019) 7020-7024.

[108] Y. Zhu, T. Cao, Z. Li, C. Chen, Q. Peng, D. Wang, and Y. Li, *Sci. China Mater.*, **61** (2018) 1527-1535.

[109] L. Lou, X. Kong, T. Zhu, J. Lin, S. Liang, F. Liu, G. Cao, and A. Pan, *Sci. China Mater.*, **62** (2019) 465-473.

[110] W. J. Zhang, *J. Power Sources*, **196** (2011) 13-24.

[111] H. Wu, G. Zheng, N. Liu, T. J. Carney, Y. Yang, and Y. Cui, *Nano Lett.*, **12** (2012) 904-909.

[112] J. R. Szczech and S. Jin, *Energy Environ. Sci.*, **4** (2011) 56-72.

[113] M. Gu, Z. Wang, J. G. Connell, D. E. Perea, L. J. Lauhon, F. Gao, and C. Wang, *J. Am. Chem. Soc.*, **7** (2013) 6303-6309.

[114] X. H. Liu, J. W. Wang, S. Huang, F. Fan, X. Huang, Y. Liu, S. Krylyuk, J. Yoo, S. A. Dayeh, A. V. Davydov, S. X. Mao, S. T. Picraux, S. Zhang, J. Li, T. Zhu, and J.

Y. Huang, *Nat. Nanotechnol.*, **7** (2012) 749-756.

[115] M. Gu, Z. Wang, J. G. Connell, D. E. Perea, L. J. Lauhon, F. Gao, and C. Wang, *ACS Nano*, **7** (2013) 6303-6309.

[116] https://materialsproject.org, Retrieved June 8, 2020.

[117] H. Wu and Y. Cui, *Nano Today*, **7** (2012) 414-429.

[118] H. Wu, G. Chan, J. W. Choi, I. Ryu, Y. Yao, M. T. McDowell, S. W. Lee, A. Jackson, Y. Yang, L. Hu, and Y. Cui, *Nat. Nanotechnol.*, **7** (2012) 310-315.

[119] L. Baggetto, D. Danilov, and P. H. L. Notten, *Adv. Mater.*, **23** (2011) 1563-1566.

[120] N. Lin, Y. Han, L. Wang, J. Zhou, J. Zhou, Y. Zhu, and Y. Qian, *Angew. Chem. Int. Ed.*, **54** (2015) 3822-3825.

[121] H. Jia, P. Gao, J. Yang, J. Wang, Y. Nuli, and Z. Yang, *Adv. Energy Mater.*, **1** (2011) 1036-1039.

[122] J. K. Yoo, J. Kim, Y. S. Jung, and K. Kang, *Adv. Mater.*, **24** (2012) 5452-5456.

[123] X. Li, M. Gu, S. Hu, R. Kennard, P. Yan, X. Chen, C. Wang, M. J. Sailor, J. G. Zhang, and J. Liu, *Nat. Commun.*, **5** (2014) 4105-4111.

[124] B. Peng, F. Cheng, Z Tao, and J. Chen, *J. Chem. Phys.*, **133** (2010) 034701.

[125] J. Ryu, T. Chen, T. Bok, G. Song, J. Ma, C. Hwang, L. Luo, H. K. Song, J. Cho, C. Wang, S. Zhang, and S. Park, *Nat. Commun.*, **9** (2018) 2924-2931.

[126] H. Shang, Z. Zuo, L. Yu, F. Wang, F. He, and Y. Li, *Adv. Mater.*, **30** (2018) 1801459.

[127] Y. Han, J. Zou, Z. Li, W. Wang, Y. Jie, J. Ma, B. Tang, Q. Zhang, X. Cao, S. Xu, and Z. L. Wang, *ACS Nano*, **12** (2018) 4835-4843.

[128] Q. Xu, J. Y. Li, J. K. Sun, Y. X. Yin, L. J. Wan, and Y. G. Guo, *Adv. Energy Mater.*, **7** (2017) 1601481.

[129] R. Xu, G. Wang, T. Zhou, Q. Zhang, H. P. Cong, S. Xin, J. Rao, C. Zhang, Y. Liu, Z. Guo, and S. H. Yu, *Nano Energy*, **39** (2017) 253-261.

[130] I. H. Son, J. H. Park, S. Park, K. Park, S. Han, J. Shin, S. G. Doo, Y. Hwang, H. Chang, and J. W. Choi, *Nat. Commun.*, **8** (2017) 1561-1571.

[131] M. Ko, S. Chae, J. Ma, N. Kim, H. W. Lee, Y. Cui, and J. Cho, *Nat. Energy*, **1** (2016)

16113-16120.

[132] S. Yin, D. Zhao, Q. Ji, Y. Xia, S. Xia, X. Wang, M. Wang, J. Ban, Y. Zhang, E. Metwalli, X. Wang, Y. Xiao, X. Zuo, S. Xie, K. Fang, S. Liang, L. Zheng, B. Qiu, Z. Yang, Y. Lin, L. Chen, C. Wang, Z. Liu, J. Zhu, P. M. Buschbaum, and Y. J. Cheng, *ACS Nano*, **12** (2018) 861-875.

[133] G. T. Kim, T. Kennedy, M. Brandon, H. Geaney, K. M. Ryan, S. Passerini, and G. B. Appetecchi, *ACS Nano*, **11** (2017) 5933-5943.

[134] Y. Jin, Y. Tan, X. Hu, B. Zhu, Q. Zheng, Z. Zhang, G. Zhu, Q. Yu, Z. Jin, and J. Zhu, *ACS Appl. Mater. Interfaces*, **9** (2017) 15388-15393.

[135] H. Li, F. Cheng, Z. Zhu, H. Bai, Z. Tao, and J. Chen, *J. Alloys Compd.*, **509** (2011) 2919-2923.

[136] T. Ma, X. Yu, H. Li, W. Zhang, X. Cheng, W. Zhu, and X. Qiu, *Nano Lett.*, **17** (2017) 3959-3964.

[137] Z. Li, F. Wang, and X. Wang, *Small*, **13** (2017) 1603076.

[138] E. Park, H. Yoo, J. Lee, M. S. Park, Y. J. Kim, and H. Kim, *ACS Nano*, **9** (2015) 7690-7696.

[139] L. Luo, H. Yang, P. Yan, J. J. Travis, Y. Lee, N. Liu, D. M. Piper, S. H. Lee, P. Zhao, S. M. George, J. G. Zhang, Y. Cui, S. Zhang, C. Ban, and C. M. Wang, *ACS Nano*, **9** (2015) 5559-5566.

[140] H. Kim, M. Seo, M. H. Park, and J. Cho, *Angew. Chem. Int. Ed.*, **49** (2010) 2146-2149.

[141] X. H. Liu, L. Zhong, S. Huang, S. X. Mao, T. Zhu, and J. Y. Huang, *ACS Nano*, **6** (2012) 1522-1531.

[142] N. Lin, Y. Han, J. Zhou, K. Zhang, T. Xu, Y. Zhu, and Y. Qian, *Energy Environ. Sci.*, **8** (2015) 3187-3191.

[143] C. K. Chan, H. Peng, G. Liu, K. Mcllwrath, X. F. Zhang, R. A. Huggins, and Y. Cui, *Nat. Nanotechnol.*, **3** (2008) 31-35.

[144] X. Wang, L. Huang, Y. Zhang, F. Yin, Z. Bakenov, N. Umirov, M. Jin, and G. Zhou,

Ionics, **24** (2018) 373-378.

[145] S. Chen, Z. Chen, X. Xu, C. Cao, M. Xia, and Y. Luo, *Small*, **14** (2018) 1703361.

[146] J. Liu, Y. Yang, P. Lyu, P. Nachtigall, and Y. Xu, *Adv. Mater.*, **30** (2018), 1800838.

[147] X. Zuo, Y. Xia, Q. Ji, X. Gao, S. Yin, M. Wang, X. Wang, B. Qiu, A. Wei, Z. Sun, Z. Liu, J. Zhu, and Y. J. Cheng, *ACS Nano*, **11** (2017) 889-899.

[148] Q. Xiao, M. Gu, H. Yang, B. Li, C. Zhang, Y. Liu, F. Liu, F. Dai, L. Yang, Z. Liu, X. Xiao, G. Liu, P. Zhao, S. Zhang, C. Wang, Y. Lu, and M. Cai, *Nat. Commun.*, **6** (2015) 8844-8851.

[149] I. H. Son, J. H. Park, S. Park, K. Park, S. Han, J. Shin, S. G. Doo, Y. Hwang, H. Chang, and J. W. Choi, *Nat. Commun.*, **8** (2017) 1561-1571.

[150] M. Ko, S. Chae, J. Ma, N. Kim, H. W. Lee, Y. Cui, and J. Cho, *Nat. Energy*, **1** (2016) 16113-16120.

[151] P. Nie, X. Liu, R. Fu, Y. Wu, J. Jang, H. Dou, and X. Zhang, *ACS Energy Lett.*, **2** (2017) 1279-1287.

[152] S. Guo, X. Hu, Y. Hou, and Z. Wen, *ACS Appl. Mater. Interfaces*, **9** (2017) 42084-42092.

[153] S. Chen, L. Shen, P. A. van Aken, J. Maier, and Y. Yu, *Adv. Mater.*, **29** (2017) 1605650.

[154] W. An, B. Gao, S. Mei, B. Xiang, J. Fu, L. Wang, Q. Zhang, P. K. Chu, and K. Huo, *Nat. Commun.*, **10** (2019) 1447-1457.

[155] B. Li, S. Yang, S. Li, B. Wang, and J. Liu, *Adv. Energy Mater.*, **5** (2015) 1500289.

[156] H. Song, H. X. Wang, Z. Lin, X. Jiang, L. Yu, J. Xu, Z. Yu, X. Zhang, Y. Liu, P. He, L. Pan, Y. Shi, H. Zhou, and K. Chen, *Adv. Funct. Mater.*, **26** (2016) 524-531.

[157] Y. Yang, S. Liu, X. Bian, J. Feng, Y. An, and C. Yuan, *ACS Nano*, **12** (2018) 2900-2908.

[158] Q. Zhang, H. Chen, L. Luo, B. Zhao, H. Luo, X. Han, J. Wang, C. Wang, Y. Yang, T. Zhu, and M. Liu, *Energy Environ. Sci.*, **11** (2018) 669-681.

[159] S. Fang, L. Shen, G. Xu, P. Nie, J. Wang, H. Dou, and X. Zhang, *ACS Appl. Mater.*

Interfaces, **6** (2014) 6497-6503.

[160] J. Yang, Y. Wang, W. Li, L. Wang, Y. Fan, W. Jiang, W. Luo, Y. Wang, B. Kong, C. Selomulya, H. K. Liu, S. X. Dou, and D. Zhao, *Adv. Mater.*, **29** (2017) 1700523.

[161] C. Wang, Y. Han, S. Li, T. Chen, J. Yu, and Z. Lu, *ACS Appl. Mater. Interfaces*, **10** (2018) 12750-12758.

[162] A. Kato, M. Nose, M. Yamamoto, A. Sakuda, A. Hayashi, and M. Tatsumisago, *J. Ceram. Soc. Jpn.*, **126** (2018) 719-727.

2. PREPARATION OF NANOPOROUS Si PARTICLES

2.1. Introduction

Porous Si can be fabricated both by ‘top-down’ techniques from solid Si and by ‘bottom-up’ routes from Si atoms and Si-based molecules [1]. Electrochemical etching has been the most studied approach for chip-based applications and has been utilized to produce highly directional mesoporous and macroporous materials. Chemical conversion of porous or solid SiO_2 is currently attracting much attention for applications that require inexpensive mesoporous Si in powder form. In contrast, very few techniques are available to fabricate microporous Si with pore sizes below 2 nm.

Regarding the anodes for LIBs with liquid electrolytes, following methods have been reported to prepare the porous Si-based materials. Bang fabricated macroporous-Si particles via Ag deposition and chemical etching with HF and H_2O_2, after C coating [2]. The 3D porous Si exhibited a capacity of 400 mAh g^{-1} after 50 cycles. Nanoporous Si networks with controllable porosity and thickness were fabricated by a simple and scalable electrochemical process [3]. These served as high performance anodes with an initial discharge capacity of 2570 mAh g^{-1}, above 1000 mAh g^{-1} after 200 cycles. Liu directly derived pure Si nanoparticles from rice husks [4]. Such recovered materials exhibited high reversible capacity (2790 mAh g^{-1}) and long cycle life (86% capacity retention over 300 cycles). Porous Si-C composites were prepared by Rochow reaction, which is commonly used to produce organosilane monomers in chemical industry [5]. The interconnection between porous structure and conductive C-coated layer induced an initial discharge capacity of 2646 mAh g^{-1} and 997 mAh g^{-1} after100 cycles. Jiang developed a novel and simple method to prepare porous Si by acid etching Al-Si alloy powder [6]. The discharge capacity retained 66% as 1368 mAh g^{-1} after 258 charge and discharge cycles. Li used various conducting agents to build electrical bridges between porous Si-C composites, which significantly improved the structural stability and hence the cycle life (capacity retention of 80% at 80 cycles) [7].

Converting Mg_2Si into Si is an interesting route to obtain porous Si materials. Hwa proposed new method to synthesis mesoporous Si-C composites. Si nanoparticles were obtained through Mg_2Si reduction of amorphous Si using high energy mechanical milling process [8]. Mesoporous C matrix was fabricated via C coating method on Si nanoparticles followed by chemical etching of preexisting MgO nanoparticles. This composite anode showed excellent electrochemical performance, achieving a reversible capacity of 1600 mAh g^{-1} over 50 cycles. Nanoporous Si particles were synthesized through the reaction of Mg_2Si and molten Bi in high-purity He gas [9]. Their anodes presented a capacity retention of 1500 mAh g^{-1} after 500 cycles. Porous Si nanoparticles were prepared by a 'metathesis' reaction of Mg_2Si and $ZnCl_2$ in an autoclave at 300°C [10]. The as-prepared Si exhibited a reversible capacity of 795 mAh g^{-1} over 250 cycles. Nanoporous Si has been prepared through the air-oxidation demagnesiation of Mg_2Si at 600°C for 10 hours, followed by HCl washing [11]. The as-prepared Si exhibited a reversible capacity of 1200 mAh g^{-1} after 400 cycles.

The choice of fabrication technique for porous Si is very much dictated by application area, which has differing requirements on porosity levels, pore morphology, skeleton purity, physical form, cost, and volume. Low-cost and simple preparation process is desired in this study, because the porous Si is applied to ASSLIBs. Therefore, I firstly focused on the conversion reaction of Mg_2Si in air. This method is very simple and suitable for mass production. Mesoporous SiO_2 and SiO_2 fumes were also selected as the oxidizing agents instead of air. These conversion reactions in a vacuum should provide high-purity Si particles. In addition, Si derived from SiO_2 possibly forms unique pore structure. This chapter reviews the fabrication processes and structural properties of three kinds of nanoporous Si particles.

2.2. Air Oxidation of Mg_2Si

2.2.1. Experimental

Nanoporous Si particles were prepared through the air-oxidation demagnesiation of Mg_2Si [11]. Mg_2Si (1000 mg; Kojundo Chemical Laboratory; 99%) and Mg (30 mg; Mitsuwa Chemicals; 99%) were mechanically milled at 1800 rpm for 15 min by using a high-speed mixer (CM-1000, EYELA). The mixture was heated to 700°C with a ramp rate of 100°C min^{-1}, and it was held at 700°C for 12 hours in air. The products were soaked in 1M HCl under Ar atmosphere to remove MgO and unreacted Mg_2Si, and then collected by centrifugation. Finally, the precipitates were rinsed by deionized water and ethanol three and two times, respectively. After drying under vacuum at room temperature, nanoporous Si particles were obtained with a yield of 300 mg (82%). Hereinafter, nanoporous Si particles prepared by this process is referred to as NPS-A.

XRD patterns and Raman scattering spectra were obtained using an X-ray diffractometer (SmartLab, Rigaku) with CuKα radiation and a laser Raman spectrometer (NRS-3100, JASCO), respectively. The chemical bonding states of the products were analyzed using XPS (Kratos AXIS-ULTRA, SHIMADZU). The microstructures were examined using FE-SEM (JSM-7800F, JEOL) and TEM (JEM-2100, JEOL). The surface area and pore distribution were measured using an accelerated surface area and porosimetry system (ASAP 2020, Shimadzu).

2.2.2. Results and Discussion

Figure 2-1(a-I) and (a-II) show XRD patterns of Mg_2Si raw material and air-oxidized sample, respectively. In the pattern of the air-oxidized sample, sharp and intense Si (111) reflection, accompanied by higher-order reflections, was observed together with some diffraction peaks attributable to MgO and a small amount of unreacted Mg_2Si. These findings indicate that the air oxidation of Mg_2Si particles almost proceeded as follows:

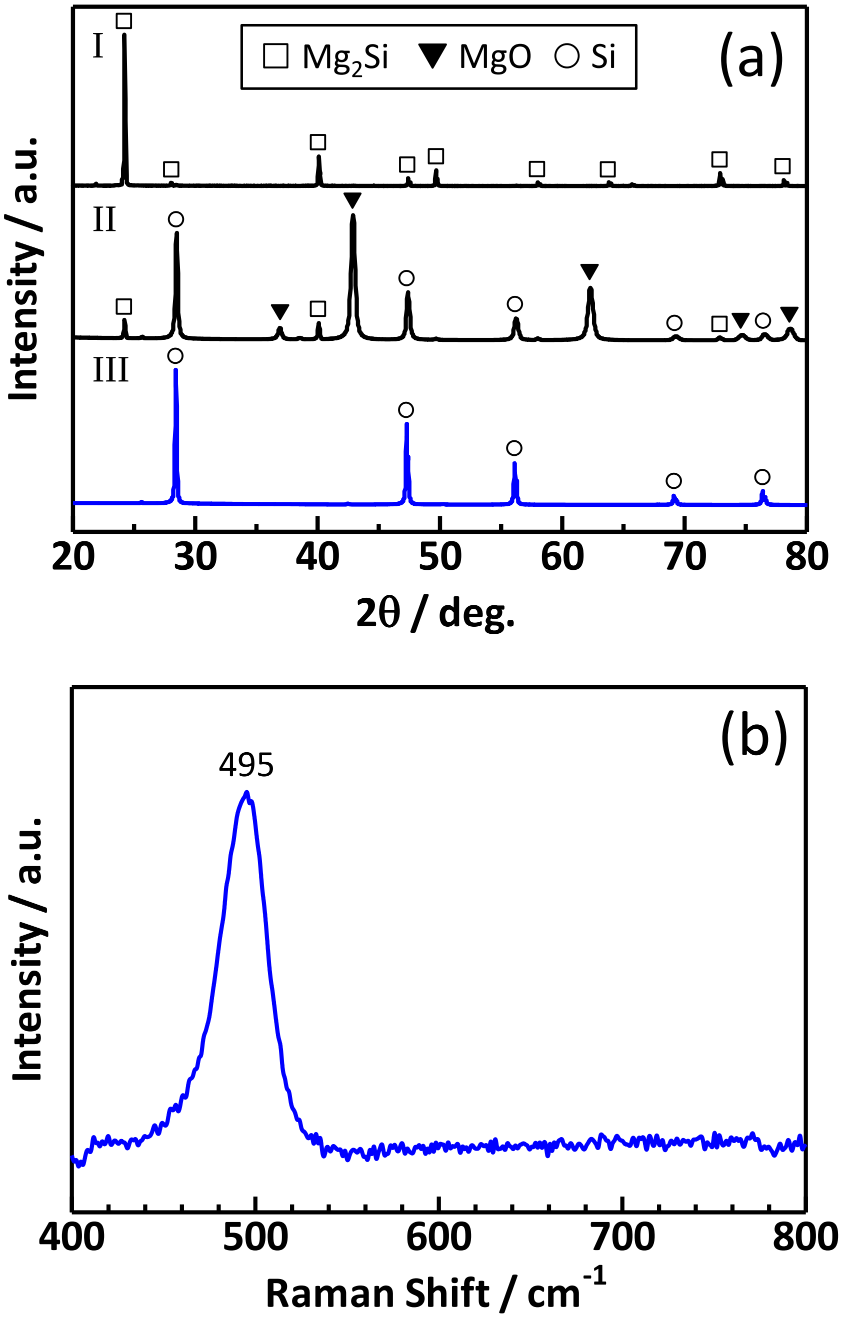

Figure 2-1. (a) XRD patterns of Mg2Si (I), air-oxidized sample (II), HCl-soaked sample (III) and (b) Raman scattering of HCl-soaked sample.

$$Mg_2Si + O_2 \text{ (air)} \rightarrow Si + 2MgO.$$

XRD pattern of HCl-soaked sample is shown in Figure 2-1(a-III). Note that all the diffraction peaks due to MgO and Mg_2Si disappeared in this process, while the observed peaks can be indexed to diamond cubic Si. The calculated lattice constant of a=0.544 nm was close to the reported value of a=0.543 nm (JCPDS 27-1402). By using Scherrer equation, the average crystallite size was estimated to be 55 nm. In Raman spectrum, Figure 2-1(b), there was a broad peak at 495 cm^{-1}. Compared with the strong scattering at 520 cm^{-1} in single crystal Si, assignable to k~0 transverse optical mode, the signal shifts to lower frequency with broadening. This is due to the decrease in the crystallite size. In fact, a shift of 10 cm^{-1} has been reported to correspond to a size change of 11 nm [12]. Figure 2-2 shows XPS spectra of NPS-A and non-porous Si particles. The feature of O 1s and Si 2p electrons indicates that the surface of NPS-A is more oxidized than that of non-porous Si. Both samples showed the similar peaks of elemental Si (at 98.9 eV and 99.1 eV), which is attributed to Si cores. On the other hand, the signals of Si oxides were observed at various binding energies: 103.4 eV and 101.2 eV for NPS-A and 103.1 eV, 100.2 eV, and 99.5 eV for non-porous Si. These results suggest that two kinds of Si particles suffered the different passivation because of their dissimilar surface activities. Some SiO_x with the binding energies near 100 eV are probably O-doped oxides, because the binding energy for Si 2p in pure SiO_2 is about 104 eV [13]. As shown in SEM image (Figure 2-3(a)), the disordered nano-sized pores were observed on the surface of NPS-A. I found the aggregation of particles with several ten nanometers in TEM image, Figure 2-3(b). Based on BET analysis, the specific surface area and pore size were approximately 140 $m^2\ g^{-1}$ and 9.4 nm, respectively (Figure 2-4). These experimental results indicate that NPS-A were successfully prepared by the air-oxidation demagnesiation of Mg_2Si.

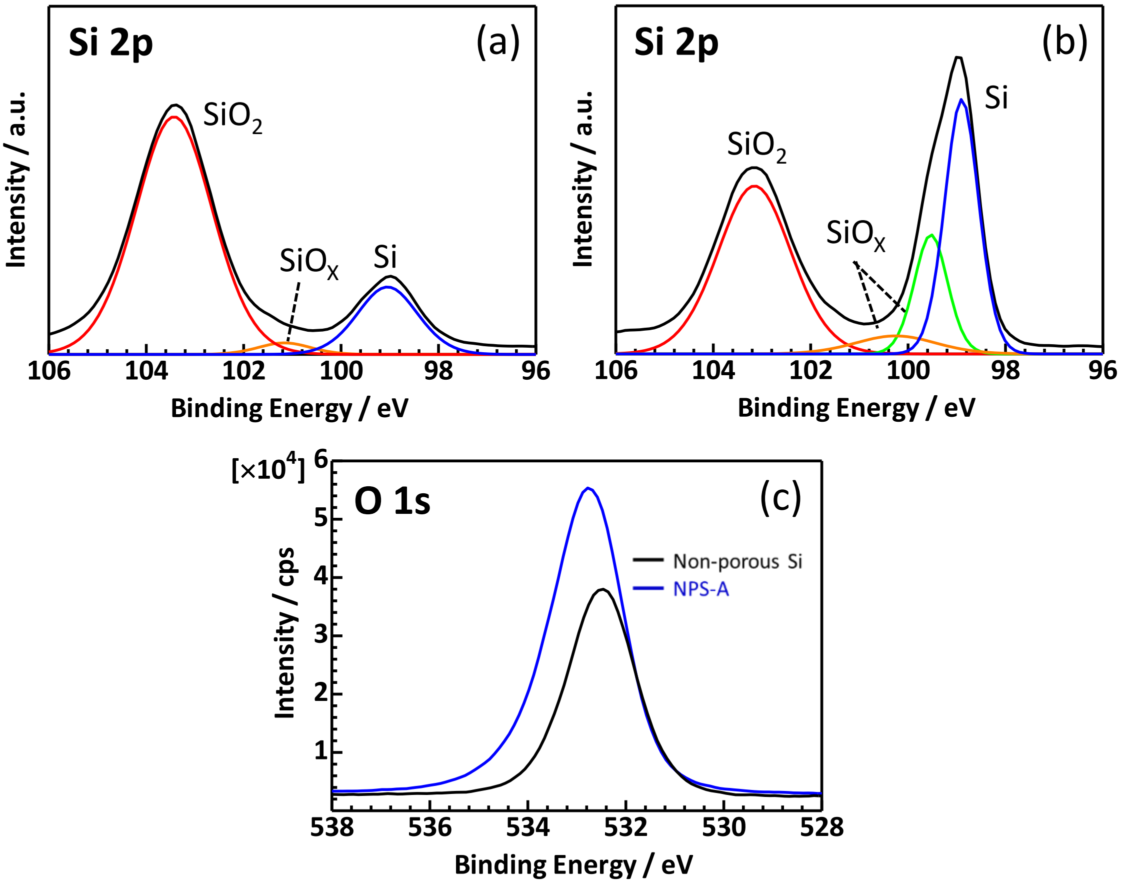

Figure 2-2. XPS spectra for Si 2p electrons of (a) NPS-A, (b) Non-porous Si, and (c) O 1s electrons of both samples.

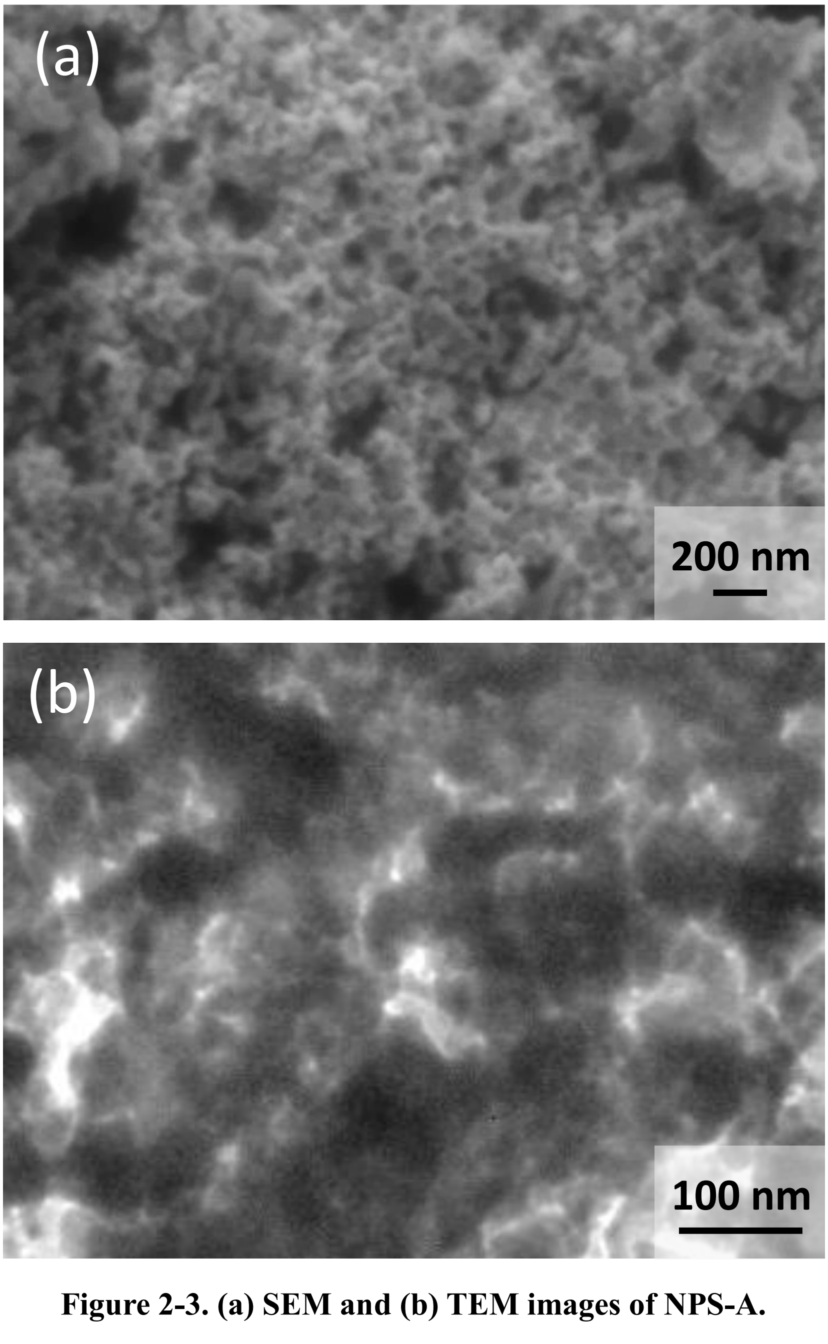

Figure 2-3. (a) SEM and (b) TEM images of NPS-A.

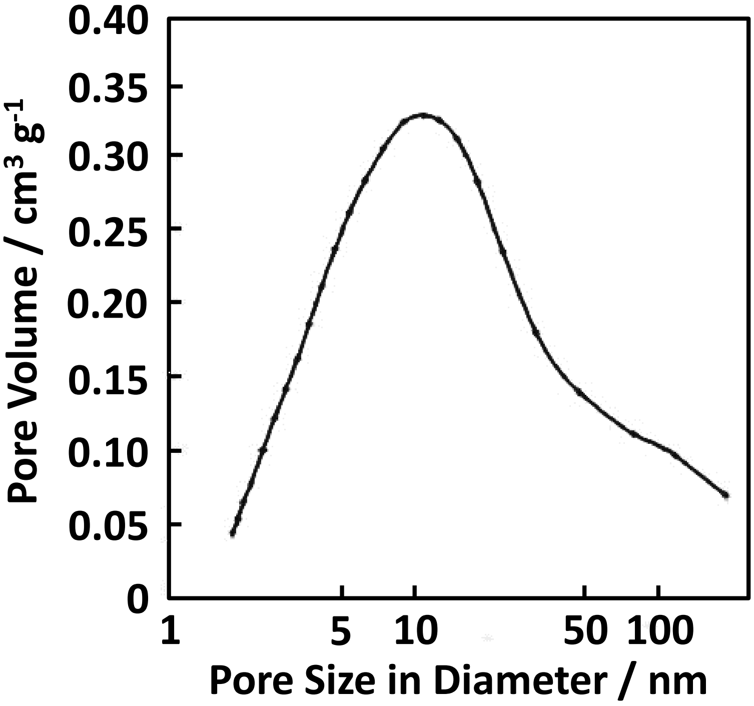

Figure 2-4. Pore size distribution of NPS-A.

2.3. Mg_2Si Reduction of Mesoporous SiO_2

2.3.1. Experimental

Nanoporous Si particles were prepared by Mg_2Si reduction of mesoporous SiO_2. First, mesoporous SiO_2 spheres were synthesized by following Fang's method [14]. Tetraethyl orthosilicate (TEOS: 6 ml; Nacalai Tesque; 95%) was rapidly added to a mixture of ethanol (74 ml), deionized water (10 ml), and ammonium solution (3.15 ml; Nacalai Tesque; 28%). The mixture was then stirred at 25°C for 6 hours to give a white SiO_2 colloidal suspension. SiO_2 particles were centrifuged from the suspension and washed 3 and 2 times with deionized water and ethanol, respectively. As-prepared 1000 mg of SiO_2 spheres were homogeneously dispersed by sonication in 180 ml of deionized water for 15 min. The suspension was added to a solution containing cetyltrimethyl ammonium bromide (CTAB: 1.5 g; Tokyo Chemical Industry; 98%), deionized water (300 ml), ethanol (300 ml), and ammonia solution (5.5 ml). The mixture was stirred at 25°C for 30 min and then TEOS (2.5 ml) was added rapidly. After reaction with stirring for 6 hours, the product, SiO_2 spheres/CTAB/SiO_2, was collected by centrifugation and re-dispersed in 200 ml of deionized water. With vigorous stirring, Na_2CO_3 (4.24 g; Futaba Pure Chemicals) were added into the well-sonicated water suspension of SiO_2 spheres/CTAB/SiO_2. After the reaction was stirred at 50°C for 10 hours, nanoporous Si particles were collected by centrifugation and extensively washed with deionized water and ethanol. Hereinafter, nanoporous Si particles prepared by this process is referred to as NPS-M.

NPS-M were prepared in the following manner under an Ar atmosphere, unless otherwise specified. Mg_2Si (255.2 mg, 3.3 mmol; Kojundo Chemical Laboratory; 99%), mesoporous SiO_2 (200.0 mg, 3.3 mmol), and Mg (8.1 mg, 0.33 mmol; Mitsuwa Chemicals; 99%) were mechanically milled at 1800 rpm for 15 min using a high-speed mixer (CM-1000, EYELA) with ZrO_2 balls (ϕ4 mm (12 g) and ϕ1 mm (5 g)). Mg was added to inhibit the peroxidation. The mixture was heated to 700°C with a ramp rate of

100°C min^{-1} and sintered at 700°C in vacuum for 12 hours. The products were immersed in 1M HCl to remove MgO and unreacted Mg_2Si, and then collected by centrifugation. Subsequently, the precipitate was rinsed with deionized water and ethanol three times and twice, respectively. Finally, after drying under vacuum at room temperature, NPS-M were obtained in a yield of 150 mg, 5.3 mmol (80%).

The measurement methods of XRD, Raman scattering, XPS, SEM, TEM, surface area, and pore distribution were described in Paragraph 2.2.1.

2.3.2. Results and Discussion

Figure 2-5(a) shows XRD patterns of NPS-M. All the peaks were indexed to diamond cubic Si. This result indicates that Mg_2Si reduction of mesoporous SiO_2 particles almost proceeded as follows:

$$Mg_2Si + SiO_2 \rightarrow 2Si + 2MgO$$

The calculated lattice constant of a=0.544 nm was close to the reported value of a=0.543 nm (JCPDS 27-1402). By using Scherrer equation, the average crystallite size was estimated to be 55 nm. In Raman spectrum, Figure 2-5(b), there was a broad peak at 513 cm^{-1}. Compared with the similar scattering at 495 cm^{-1} in NPS-A, the signal shifts to the higher frequency. This is due to the increase in the crystallite size [12]. Figure 2-6 shows XPS spectra of NPS-M. For comparison, O 1s profile includes NPS-A signal. Si 2p peak at 98.8 eV is attributed to the Si cores. SiO_2 and oxygen-doped oxides exhibited other peaks at 102.8 eV, 100.5 eV, and 99.5 eV. The vertical axis represents the relative photoelectron intensity in cps (counts per second). O 1s intensity of NPS-M (14824 cps) decreased to about 27% of NPS-A value (55350 cps). Compared with the air oxidation of Mg_2Si to prepare NPS-A, the oxygen source is limited to SiO_2 under vacuum conditions. As a result, higher-purity NPS-M were obtained using this process. SEM and TEM measurements revealed that nano-sized pores were present on the surface and inside of Si

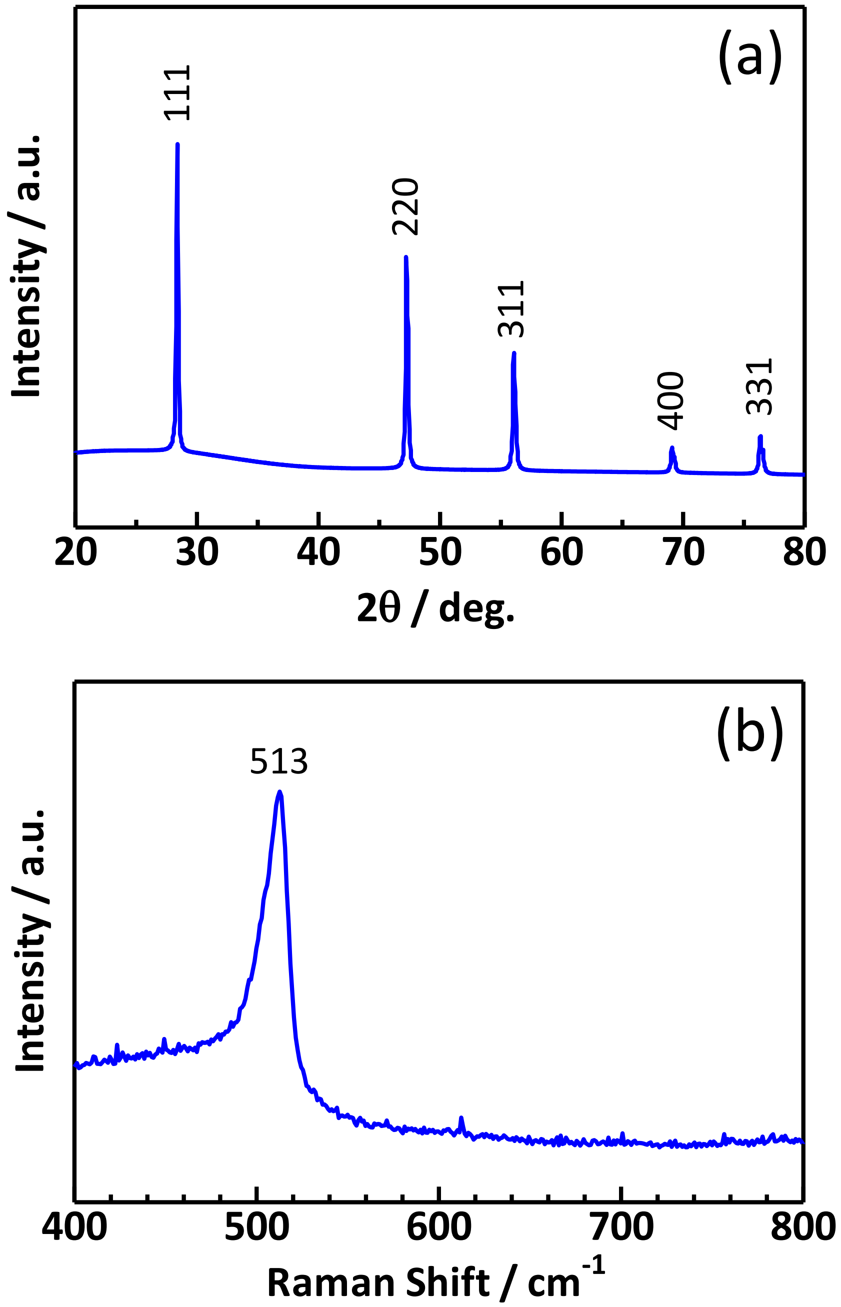

Figure 2-5. (a) XRD pattern and (b) Raman scattering spectrum of NPS-M.

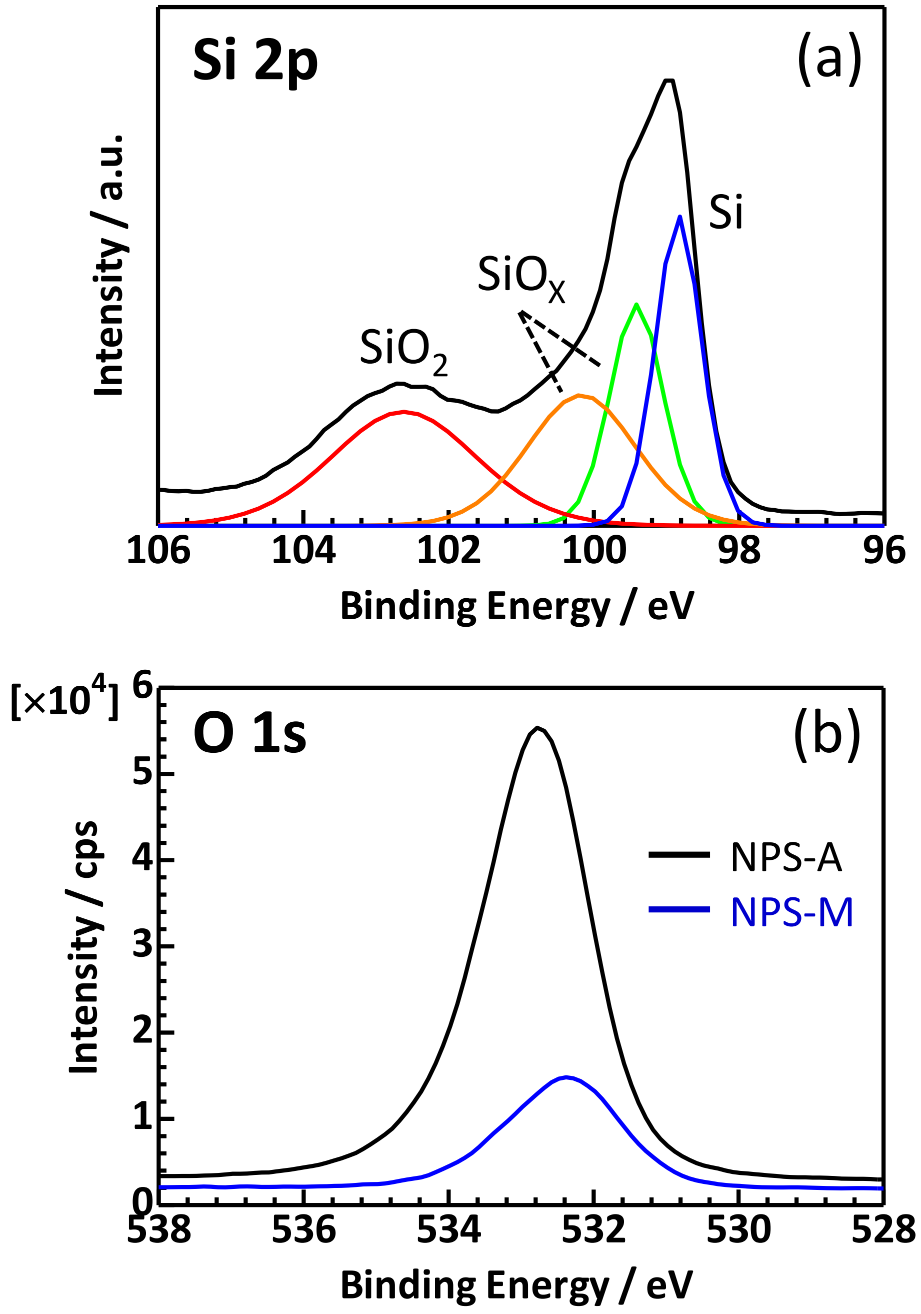

Figure 2-6. XPS spectra for (a) Si 2p electrons of NPS-M and (b) O 1s electrons of NPS-M and NPS-A.

particles (Figure 2-7). BET specific surface area and pore size were 200 m^2 g^{-1} and 6.0 nm, respectively (Figure 2-8). Compared with the air oxidation of Mg_2Si, the surface area increased by 1.4 times and the pore size decreased by 37%. The experimental results described above indicate that NPS-M were successfully prepared by Mg_2Si reduction of mesoporous SiO_2 and demagnesification.

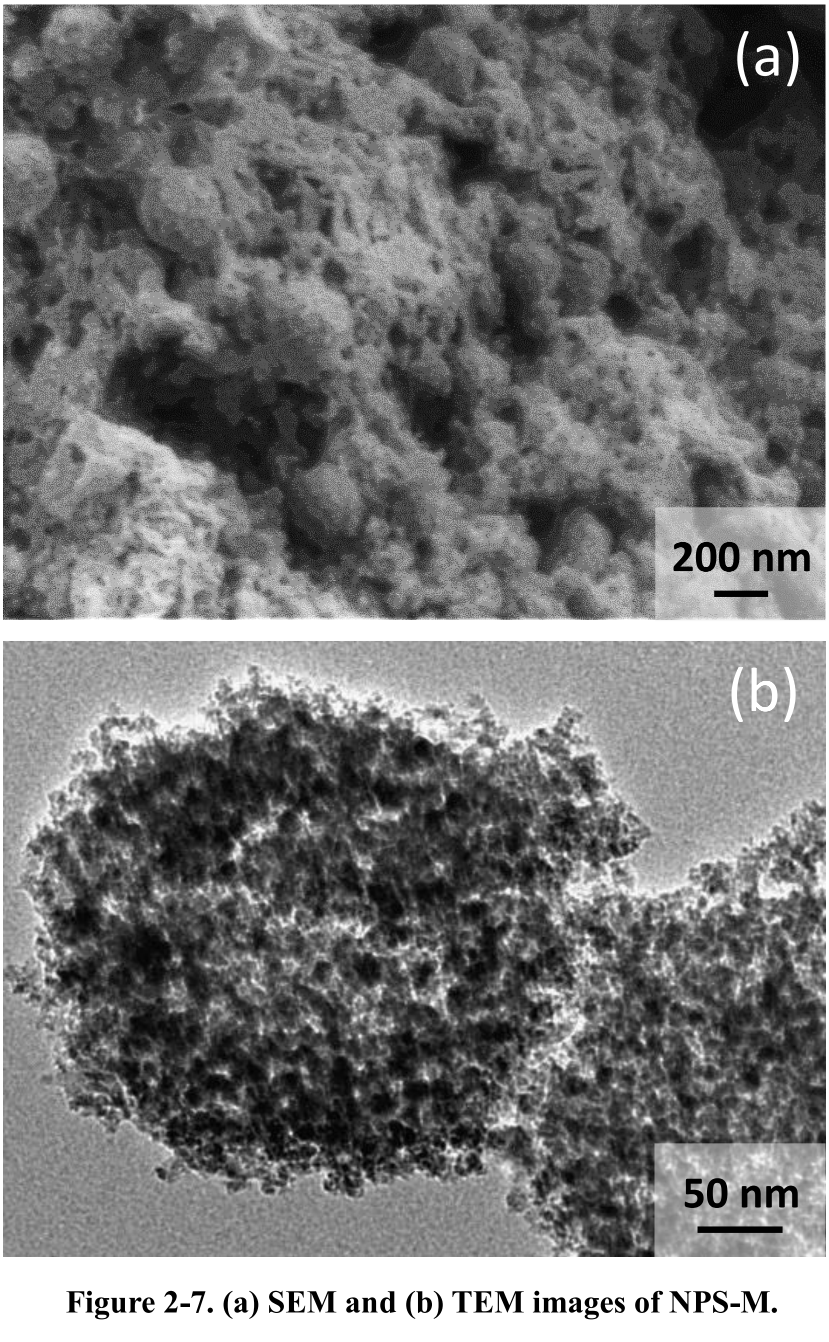

Figure 2-7. (a) SEM and (b) TEM images of NPS-M.

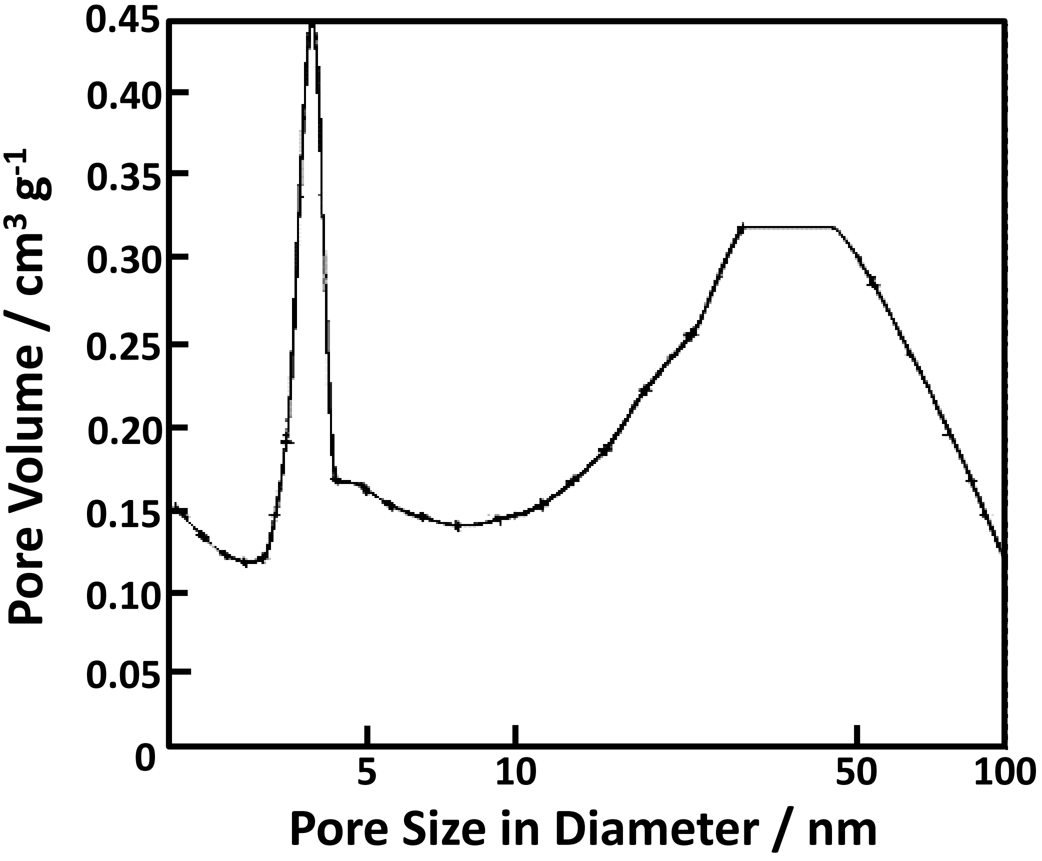

Figure 2-8. Pore size distribution of NPS-M.

2.4. Mg_2Si Reduction of SiO_2 Fume

2.4.1. Experimental

Nanoporous Si particles were prepared as follows under Ar atmosphere, unless otherwise specified, by using Mg_2Si reduction of SiO_2 fumes [15]. Mg_2Si (382.9 mg, 5.0 mmol; Kojundo Chemical Laboratory; 99%), SiO_2 fumes (300.0 mg, 5.0 mmol; Sigma Aldrich; 0.2-0.3 μm in diameter), and Mg (12.1 mg, 0.50 mmol; Mitsuwa Chemicals; 99%) were mechanically milled at 1800 rpm for 15 min by using a high-speed mixer. The mixture was heated to 700°C with a ramp rate of 100°C min^{-1}, and it was held at 700°C for 12 hours in vacuum. The products were soaked in 1M HCl under Ar atmosphere to remove MgO and unreacted Mg_2Si, and then collected by centrifugation. Finally, the precipitates were rinsed by deionized water and ethanol three and two times, respectively. After drying under vacuum at room temperature, nanoporous Si particles were obtained with a yield of 225 mg, 8.0 mmol (81%). Hereinafter, nanoporous Si particles prepared by this process is referred to as NPS-F.

The measurement methods of XRD, Raman scattering, XPS, SEM, TEM, surface area, and pore distribution were described in Paragraph 2.2.1.

2.4.2. Results and Discussion

Figure 2-9(a) shows XRD patterns of NPS-F. All the peaks were indexed to diamond cubic Si. This finding indicates that Mg_2Si reduction of SiO_2 fumes proceeds as follows, similar to NPS-M.

$$Mg_2Si + SiO_2 \rightarrow 2Si + 2MgO$$

The calculated lattice constant of a=0.544 nm was close to the reported value of a=0.543 nm (JCPDS 27-1402). By using Scherrer equation, the average crystallite size was estimated to be 55 nm. In Raman spectrum, Figure 2-9(b), there was a broad peak at 496

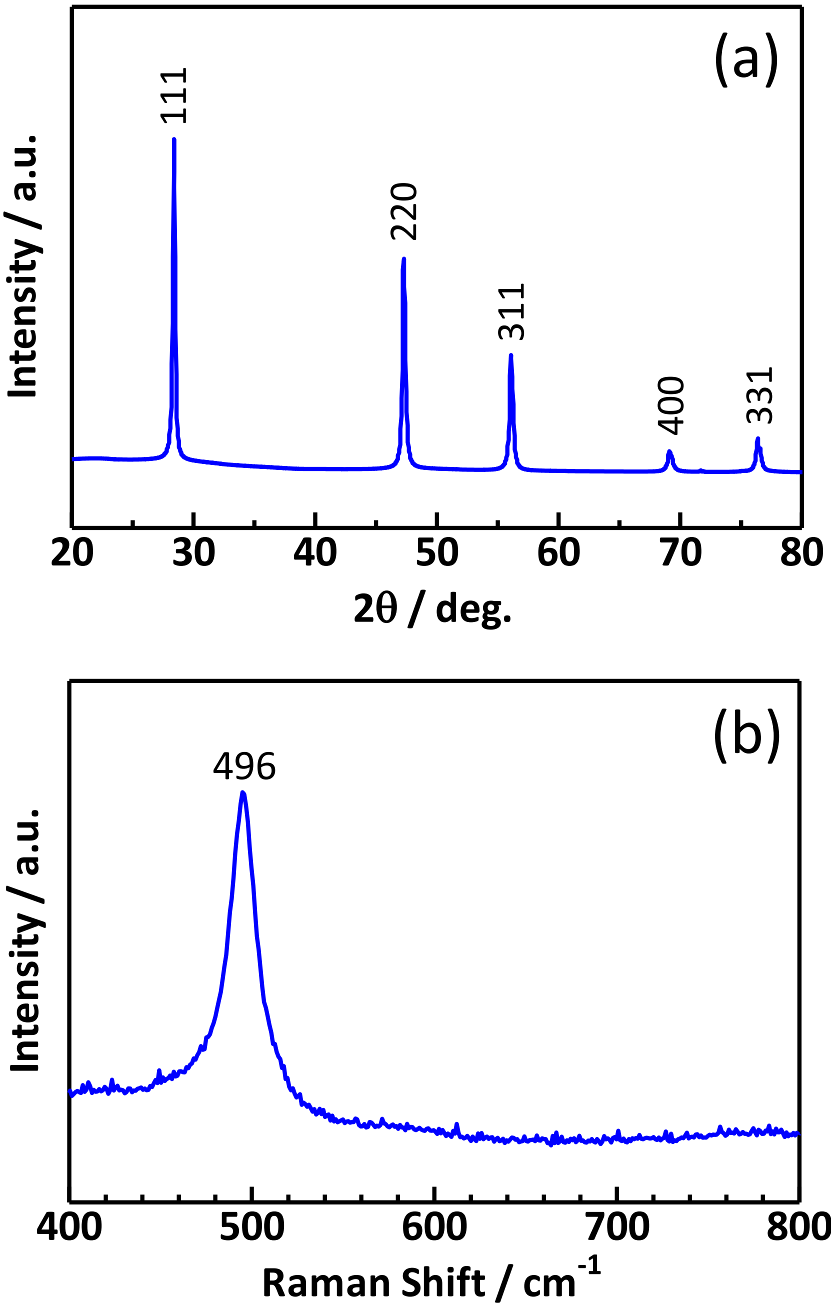

Figure 2-9. (a) XRD pattern and (b) Raman scattering spectrum of NPS-F.

cm^{-1}. This wavelength is close to 495 cm^{-1} in NPS-A. Therefore, NPS-F and NPS-A have similar crystallite sizes. XPS spectra of NPS-F are shown in Figure 2-10. For comparison, O 1s profile includes the signals of NPS-A and NPS-M. Si 2p peak at 98.9 eV is attributed to Si cores. SiO_2 and oxygen-doped oxides exhibited other peaks at 102.6 eV, 100.2 eV, and 99.4 eV. This feature of O 1s and Si 2p electrons indicates the slight oxidation on NPS-F surface. O 1s intensity of NPS-F (14431 cps) is nearly equal to that of NPS-M (14824 cps). On the other hand, the intensity of NPS-A O1s (55350 cps) is extremely large. These results demonstrate that Mg_2Si reduction of SiO_2 is superior to the air oxidation of Mg_2Si in the preparation of high-purity nanoporous Si particles. As shown in SEM image (Figure 2-11(a)), the disordered nano-sized pores were observed on the surface of powder. I found the aggregation of particles with several ten nanometers in the TEM image, Figure 2-11(b). Based on BET analysis, the specific surface area and pore size of NPS-F were approximately 213 m^2 g^{-1} and 5.9 nm (Figure 2-12), respectively. These experimental results indicate that NPS-F were successfully prepared by Mg_2Si reduction of SiO_2 fumes and demagnesification.

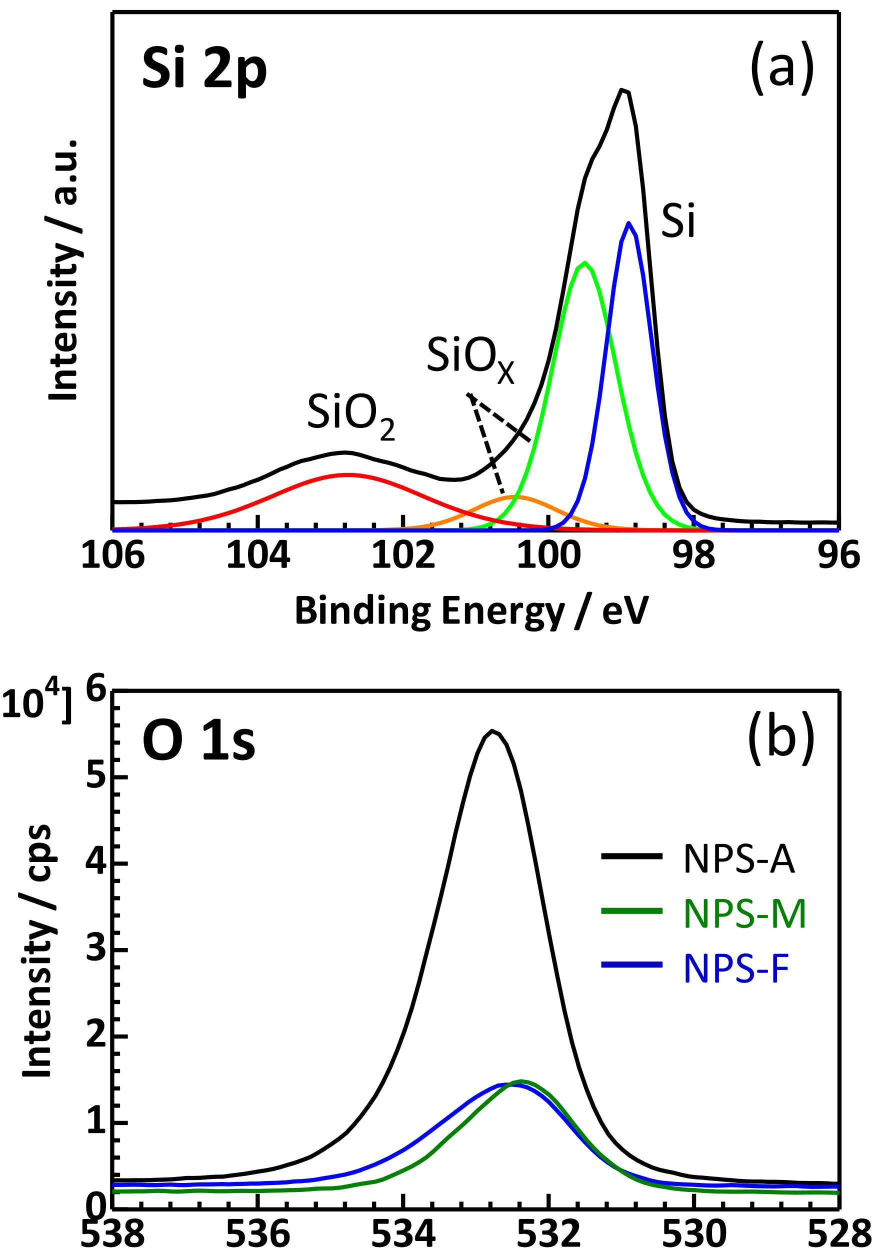

Figure 2-10. XPS spectra for (a) Si 2p electrons of NPS-F and (b) O 1s electrons of NPS-F, NPS-M, and NPS-A.

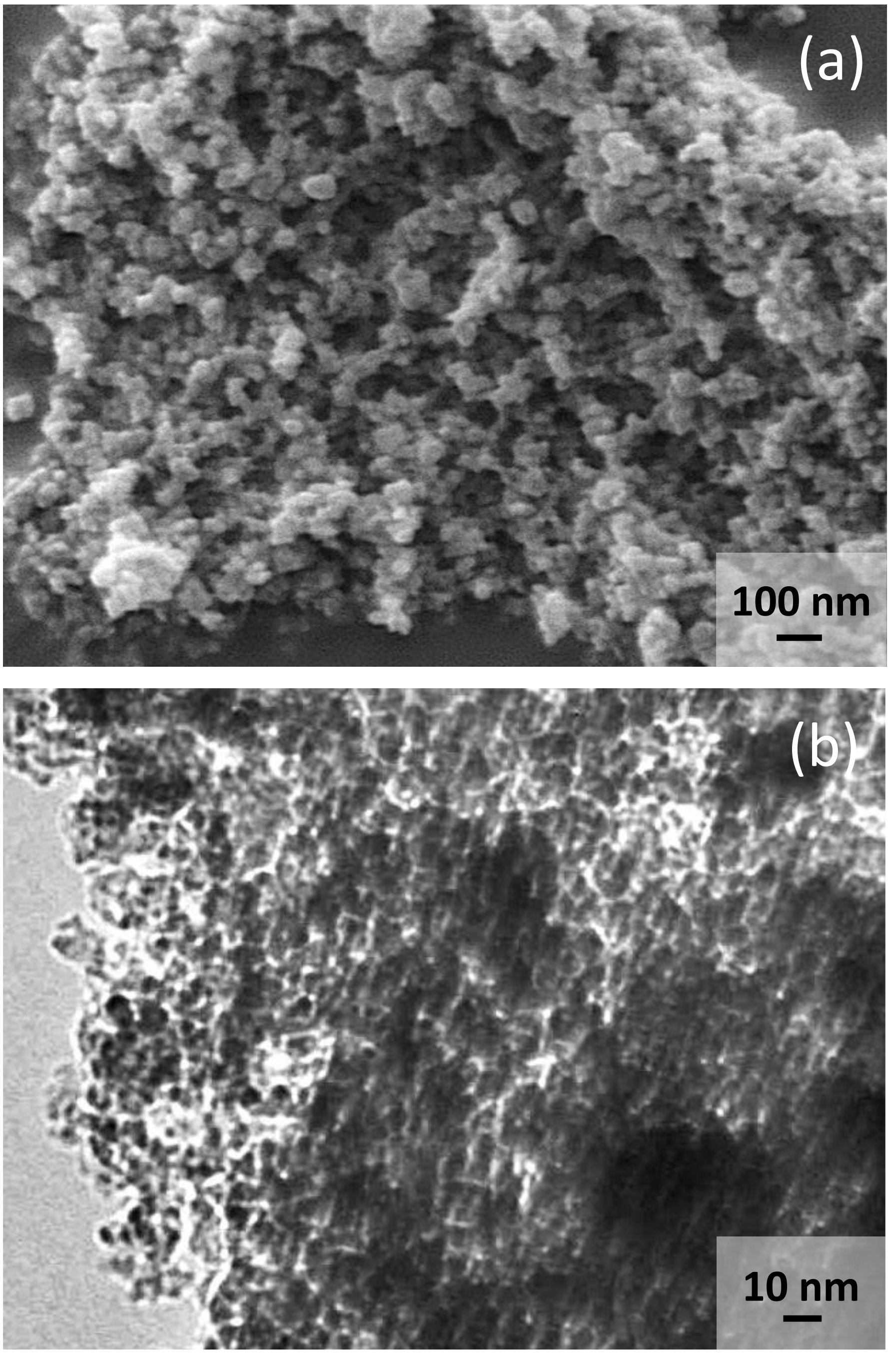

Figure 2-11. (a) SEM and (b) TEM images of NPS-F.

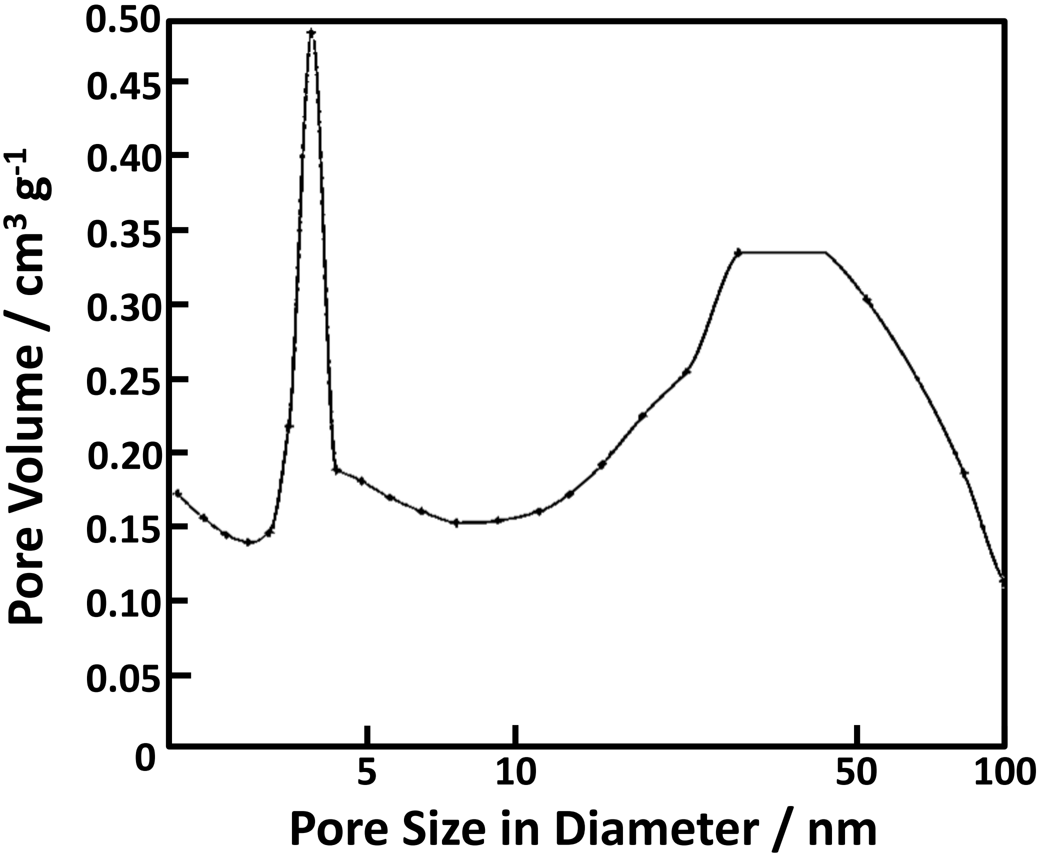

Figure 2-12. Pore size distribution of NPS-F.

2.5. Summary

Nanoporous Si particles could be successfully prepared by three methods: air oxidation of Mg_2Si (for NPS-A), Mg_2Si reduction of mesoporous SiO_2 (for NPS-M), and Mg_2Si reduction of SiO_2 fumes (for NPS-F). These processes based on the mixing of reactants are very simple and suitable for mass production. In comparison with other techniques such as anodization, etching, and deposition, the merits are as follows:

1) No special environments or equipments required
2) No acids or alkalis required
3) No toxic solvents required
4) Easy batch modification
5) Low running cost and low risk

All the peaks in XRD patterns of NPS-A, NPS-M, and NPS-F were indexed to diamond cubic Si. The calculated lattice constants for the three NPSs were exactly the same at a=0.544 nm. This is close to the reported value of 0.543 nm for Si (JCPDS 27-1402). The average crystal size evaluated using the Scherrer equation also agreed at 55 nm among the three NPSs. These results indicate that all the prepared nanoporous particles are composed of a similar Si single phase.

Raman spectra showed a broad peak at 495 cm^{-1}, 513 cm^{-1} and 496 cm^{-1} for NPS-A, NPS-M, and NPS-F, respectively. This can be assigned to k~0 transverse optical mode. Compared with the strong scattering of single crystal Si at 520 cm^{-1}, the signal shifts to lower frequencies with broadening. This is due to the decrease in the crystallite size. Among the three NPSs, NPS-M had the largest size, and NPS-F and NPS-A had similar sizes.

The features of O 1s and Si 2p electrons in XPS profiles indicate the presence of oxide layers on the surface of the prepared nanoporous Si particles. Based on the comparison between the relative photoelectron intensities of O 1s, NPS-A was strongly oxidized because of the preparation in air. On the other hand, O 1s intensities of NPS-M

(14824 cps) and NPS-F (14431 cps) were about 27% and 26% of NPS-A values (55350 cps), respectively. This is because the oxygen source is limited to SiO_2 under vacuum conditions. These results indicate that Mg_2Si reduction of SiO_2 is suitable for the preparation of high-purity nanoporous Si particles.

In SEM and TEM measurements, the disordered nano-sized pores and the aggregation of particles with several ten nanometers were similarly observed for the three NPSs. Based on BET analysis, the specific surface areas and pore sizes of NPS-A, NPS-M, and NPS-F were about 140 m^2 g^{-1} and 9.4 nm, 200 m^2 g^{-1} and 6.0 nm, and 213 m^2 g^{-1} and 5.9 nm, respectively. It was reasonably confirmed that the smaller the pore size, the larger the surface area.

Based on the structural data evaluated by XPS, DLS, and BET analyses (Table 2-1), the electrochemical characteristics of nanoporous Si cells are expected as follows. The intensity of O1s signals in XPS profiles reflects the amount of oxides near the surface of Si particles. Therefore, NPS-A with O1s intensity of 55350 cps contains a lot of Si oxides. Here, the theoretical capacities of Si oxides are smaller than that of Si. On the other hand, the particle size of NPS-M (354 nm), which has the similar O1s intensity as NPS-F, is obviously smaller than that of NPS-F (479 nm). Such small Si particles that are not in contact with the conductive additive cannot involve in charging and discharging. The results describe above suggest that NPS-F cell show the largest capacity among three kinds of nanoporous Si cells. In addition, Si oxides form several Li oxides (Li_2O, Li_4SiO_4, and $Li_2Si_2O_5$) during charging, which show no reversible reactions. Therefore, NPS-F cell with the smallest O1s intensity (14431 cps) is expected to have less loss of Li^+ ions, resulting in the largest CE. In NPS-A cell, where the pore size is 9.4 nm, the volume change during charging and discharging is possibly mitigated by the shrinkage and expansion of the pores. In contrast, the volume change cannot be completely absorbed in NPS-F cell with a small pore size (5.9 nm), which should decrease the capacity retention.

Table 2-1. Structural data of nanoporous Si particles.

Active Material	Intensity of O 1s (cps)	Particle Size (nm)	Pore Size (nm)
Nanoporous Si: NPS-F	14431	479	5.9
Nanoporous Si: NPS-M	14824	354	6
Nanoporous Si: NPS-A	55350	506	9.4
Non-porous Si	37984	466	-

References

[1] L. Canham, ed., *Handbook of Porous Silicon*, Springer, Switzerland (2014).

[2] B. M. Bang, J. I. Lee, H. Kim, J. Cho, and S. Park, *Adv. Energy Mater.*, **2** (2012) 878-883.

[3] J. Zhu, C. Gladden, N. A. Liu, Y. Cui, and X. Zhang, *Phys. Chem. Chem. Phys.*, **15** (2013) 440-443.

[4] N. Liu, K. Huo, M. T. McDowell, J. Zhao, and Y. Cui, *Sci. Rep.*, **3** (2013) 1919.

[5] Z. Zhang, Y. Wang, W. Ren, Q. Tan, Y. Chen, H. Li, Z. Zhong, and F. Su, *Angew. Chem. Int. Ed.*, **53** (2014) 5165-5169.

[6] Z. Jiang, C. Li, S. Hao, K. Zhu, and P. Zhang, *Electrochim. Acta*, **115** (2014) 393-398.

[7] Z. Z. Li, W. Wang, Z. H. Li, Z. H. Qin, J. Wang, and Z. P. Liu, *J. Power Sources,* **286** (2015) 534-539.

[8] Y. Hwa, W. S. Kim, B. C. Yu, J. H. Kim, S. H. Hong, and H. J. Sohn, *J. Power Sources*, **252** (2014) 144-149.

[9] L. Wang, N. Lin, J. Zhou, Y. Zhu, and Y. Qian, *ChemComm*, **51** (2015) 2345-2348.

[10] T. Wada, T. Ichitsubo, K. Yubuta, H. Segawa, H. Yoshida, and H. Kato, *Nano Lett.*, **14** (2014) 4505-4510.

[11] J. Liang, X. Li, Z. Hou, C. Guo, Y. Zhu, and Y. Qian, *ChemComm*, **51** (2015) 7230-7233.

[12] R. P. Wang, G. W. Zhou, Y. L. Liu, S. H. Pan, H. Z. Zhang, D. P. Yu, and Z. Zhang, *Phys. Rev. B*, **61** (2000) 16827-16832.

[13] H. Nakano, M. Nakano, K. Nakanishi, D. Tanaka, Y. Sugiyama, T. Ikuno, H. Okamoto, and T. Ohta, *J. Am. Chem. Soc.*, **134** (2012) 5452-5455.

[14] X. Fang, C. Chen, Z. Liu, P. Liu, and N. Zheng, *Nanoscale*, **3** (2011) 1632-1639.

[15] T. Zhang, L. Hu, J. Liang, Y. Han, Y. Lu, Y. Zhu, and Y. Qian, *RSC Adv.*, **6** (2016) 30577-30581.

3. APPLICATION TO SULFIDE-BASED ALL-SOLID-STATE LITHIUM-ION BATTERIES

3.1. Introduction

In LIBs with liquid electrolytes, a lot of Si-based anodes with different structures and compositions have been explored to improve battery performance, as described in Section 1.3. In contrast, there have been a few reports concerning ASSLIBs, because of the extreme volumetric change of Si during lithiation and delithiation. Multiwalled-carbon-nanotubes (MWCNTs) were studied as a conductive additive for ASSLIBs using Si nanoparticle anodes [1]. For over 100 cycles, reversible capacities over 900 mAh g^{-1} were measured for these anodes. MWCNTs were shown to be a superior conducting additive for LIBs with a solid-state construction. In addition, Si nanoparticles demonstrated reversible cycling over bulk Si anode material. Pure amorphous Si films prepared by r.f. sputtering process exhibited excellent anode performance in all-solid-state electrochemical systems [2]. They kept high capacity of 2400 mAh g^{-1} even under high current discharge of 10 mA cm^{-2}. Cycle properties under 0.1 mA cm^{-2} were stable with high coulombic efficiency nearly unity. Kato reported that Li_2S-P_2S_5 glasses with lithium halides, especially LiI, exhibited both high ionic conductivity and favorable mechanical properties [3]. The addition of lithium halides decreased the Young's modulus of the electrolytes. In addition, fewer pores and grain boundaries were observed in the powder-pressed pellets of Li_2S-P_2S_5 glasses with lithium halides. ASSLIBs using Si anodes and glass electrolytes with lithium halides exhibited a larger capacity (1500 mAh g^{-1}) of 20 cycles compared to those without lithium halides. These results provided guidelines for the construction of ASSLIBs from the viewpoint of the mechanical properties of solid electrolytes. Yamamoto presented a slurry-mixing method for fabricating homogeneously dispersed composite sheets containing micrometer-sized Si particles [4]. Subsequent removal of the volatile binder from the stacked-sheet cells was demonstrated to reduce their internal resistance. Si composite sheets exhibited high initial coulombic efficiencies of 95%, with practical areal capacities of 2.0-4.4 mAh cm^{-2} at the 47th cycle under 0.30 mA cm^{-2}, a reversible specific capacity of 2300 mAh g^{-1} after 100 cycles, and long-term cycling stability (specific capacity above 1700 mAh g^{-1} after 375 cycles). Cracks vertical to Si composite layer after cycling was suggested to buffer the internal strain originating from Si volume changes, providing excellent cycling stability. These results assisted the rational design of Si anodes for high-cell-performance ASSLIBs. Piper showed that Si alloyed with fewer moles of Li as the confinement pressure increased [5]. This limited Si particles' expansion and improved their cycling stability. Si-C composites consisting of Si particles embedded in a dense and non-porous C matrix were prepared by the pyrolysis of intimate mixtures of poly (vinyl chloride) and Si powder at 900°C under a flow of N_2 [6]. A capacity of 1000 mAh g^{-1} was achieved for 20 cycles (0-2.0 V vs. Li^+/Li) for a Si-C composite containing nano-sized Si particles. Son reported a Si-Ti-Ni ternary alloy developed for commercial application as an anode material for lithium ion batteries [7]. The alloy exhibited a stable capacity above 900 mAh g^{-1} after 50 cycles and a high coulombic efficiency of up to 99.7% during cycling. To enable a highly reversible nano-sized Si anode, melt spinning was employed to embed nano-sized Si particles in a $Ti_4Ni_4Si_7$ matrix. Whitley presented a proof-of-concept: pairing high capacity anode materials by imbedding Si in Sn matrix [8]. The cell exhibited with a reversible capacity of 700 mAh g^{-1} for 50 cycles. Si-C composite anodes were formed through the pyrolysis of coal-tar-pitch [9]. ASSLIB half cell displayed stable specific capacities of 654 mAh g^{-1} (per mass electrode) and 1089 mAh g^{-1} (per mass Si-C composite) after 100 discharge-charge cycles.

In this study, nanoporous Si particles were applied to ASSLIBs with half cell configuration. This is because the nano-sized pores are expected to act as buffer regions for large volume changes. In addition, a sulfide-based solid electrolyte was used to prepare the composites. Sulfides exhibit excellent adhesion with Si particles via plastic deformation by pressing at room temperature. Furthermore, their low Young's modulus probably facilitates elastic deformation, resulting in a good response to volume changes [10]. In general, the performance of ASSLIBs is strongly dependent on the microstructural features of the electrodes. Therefore, it is important to optimize the dispersibility of Si particles. In this regard, the mixing methods of composite materials were also investigated to control the ion and/or electron conduction paths in the anodes. This chapter reviews the electrochemical behavior and microscopic structures of sulfied-based ASSLIBs with three kinds of nanoporous Si composite anodes.

3.2. Composite Anodes comprising Nanoporous Si Particles Prepared by Air Oxidation of Mg_2Si

3.2.1. Experimental

$75Li_2S\cdot25P_2S_5$ (mol %) solid electrolyte, abbreviated as SE, was prepared from Li_2S (Furuuchi Chemical; 99.9%) and P_2S_5 (Sigma-Aldrich; 99%) using a high-energy planetary ball mill (Pulverisette 7, Fritsch). Li_2S (30 mmol) and P_2S_5 (10 mmol) with a molar ratio of 75:25 were dry mixed using an agate mortar for 10 min. The mixture was added to ZrO_2 pot (80 ml) with ZrO_2 balls (5 mm in diameter, 106 g) and 8 g of heptane and mechanically milled under a rotating speed of 500 rpm for 20 hours at room temperature. Fine SE powder (approximately 1 μm in diameter) used as the basis for half cells was prepared by pulverizing the as-prepared SE (approximately 10 μm in diameter, 1 g) in heptane (8.9 g) and butyl ether (0.2 g) with ZrO_2 balls (1 μm in diameter, 40 g) under a rotating speed of 200 rpm for 20 hours. Anode composite materials consisted of nanoporous Si particles (NPS-A; 36 wt%), SE (55 wt%), and acetylene black (AB; 9 wt%; Denka; 99.99%). Here, commercially available non-porous Si particles (Alfa Aesar; 1-5 μm in diameter) were used as a reference material. I adopted two mixing methods, namely mechanical milling and hand milling, to vary the dispersibility of Si particles. The mechanical milling was conducted using a high-speed mixer with ZrO_2 balls (ϕ4 mm (6 g) and ϕ1 mm (2.5 g)) under a rotation speed of 1800 rpm for 60 min. The hand milling was carried out by hand with an agate mortar and pestle for 10 min. Half cells were fabricated as shown in Figure 3-1. In an electric insulation tube (10 mm in diameter), SE (80 mg) and anode composite material (2 mg) were pressed under 330 MPa to obtain a two-layered pellet. As the counter electrode, Li-In foil was attached on SE side. Finally, the three-layered pellet was compressed at 148 MPa using stainless-steel disks. Half cells thus fabricated had high areal mass loadings of about 0.90 mg cm^{-2}, which are applicable to practical batteries. All these procedures, including the preparation of SE, anode composite materials, and half cells, were performed in a dry Ar atmosphere.

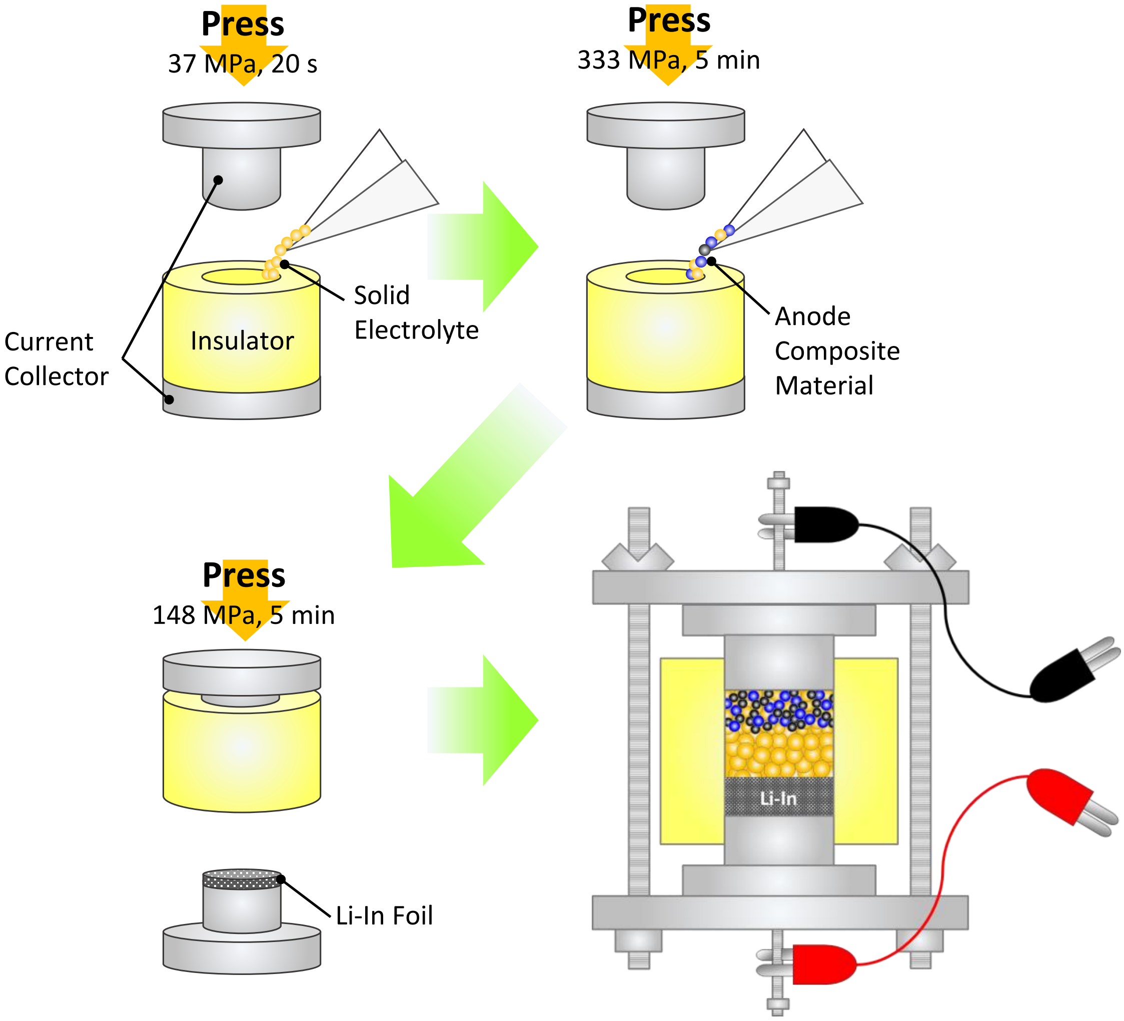

Figure 3-1. Fabrication process of all-solid-state half cells.

To accurately analyze the cross section, half cells were transferred to a polishing machine (IB-19520CCP, JEOL) using a transfer vessel to prevent exposure of the samples to air. A smooth surface was obtained by ion milling under a 4 keV Ar^+ ion beam with a current of 70-80 μA at -70ºC. The cross-sectional structure and composition were evaluated using an FE-SEM equipped with an energy-dispersive X-ray spectrometer (EDX). Dynamic light scattering (DLS; ELSZ-2000, Otsuka Electronics) was used to determine the size distribution profile of Si particles.

Electrochemical tests were conducted in constant current (CC) mode of 0.127 mA cm^{-2} (0.03 C) for the first three cycles and 0.3 mA cm^{-2} (0.08 C) for the subsequent cycles at 30ºC using a charge/discharge measurement device (BTS-2004, Nagano). The cut-off voltages were 0.88 and -0.58 V vs. Li-In, corresponding to 1.50 and 0.04 V vs. Li^+/Li, respectively. Electrochemical impedance spectroscopy (EIS) was performed using an AC impedance analyzer (FRA 1455, Solartron) in the charging state at -0.58 V in a frequency range of 2 mHz to 1 MHz with an applied amplitude voltage of 10 mV at 30ºC. Note that lithiation, i.e., alloying of Si with Li, is expressed as charging in this thesis.

3.2.2. Results and Discussion

The cross-sectional EDX mapping images of NPS-A composite anodes are shown in Figure 3-2. Si, S, and C are colored in blue, yellow, and red, respectively. In the mechanical-milled NPS-A (MM-NPS-A) anode, Si particles were highly dispersed in SE matrix. On the other hand, some Si particles were aggregated to form μm-sized grains in the hand-milled (HM-NPS-A) anode (see the dashed circle in Figure 3-2(b)). Since both the anodes contain the same quantity of NPS-A, the observed difference is caused by the mixing methods. Namely, the dispersibility of Si particles in the composite anodes can be improved by adapting the mechanical milling.

Figure 3-3 and Table 3-1 show the charge and discharge characteristics of half cells with various Si composite anodes during the first three cycles. MM-NPS-A and HM-NPS-A half cells exhibited the initial charge capacities of 2543 mAh g^{-1} and 3259 mAh g^{-1},

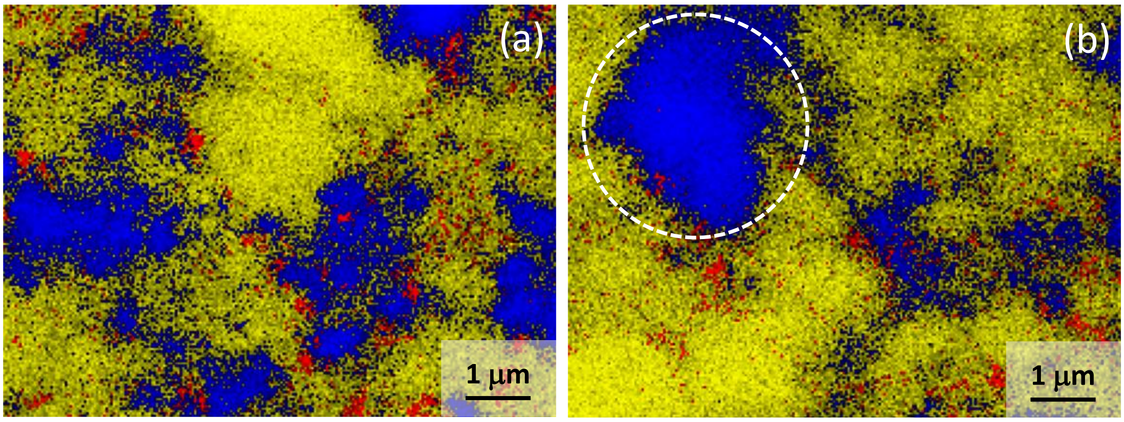

Figure 3-2. EDX mapping images of (a) mechanical-milled and (b) hand-milled NPS-A composite anodes. Si, S, and C are colored in blue, yellow, and red, respectively. Dashed circle indicates NPS-A aggregate.

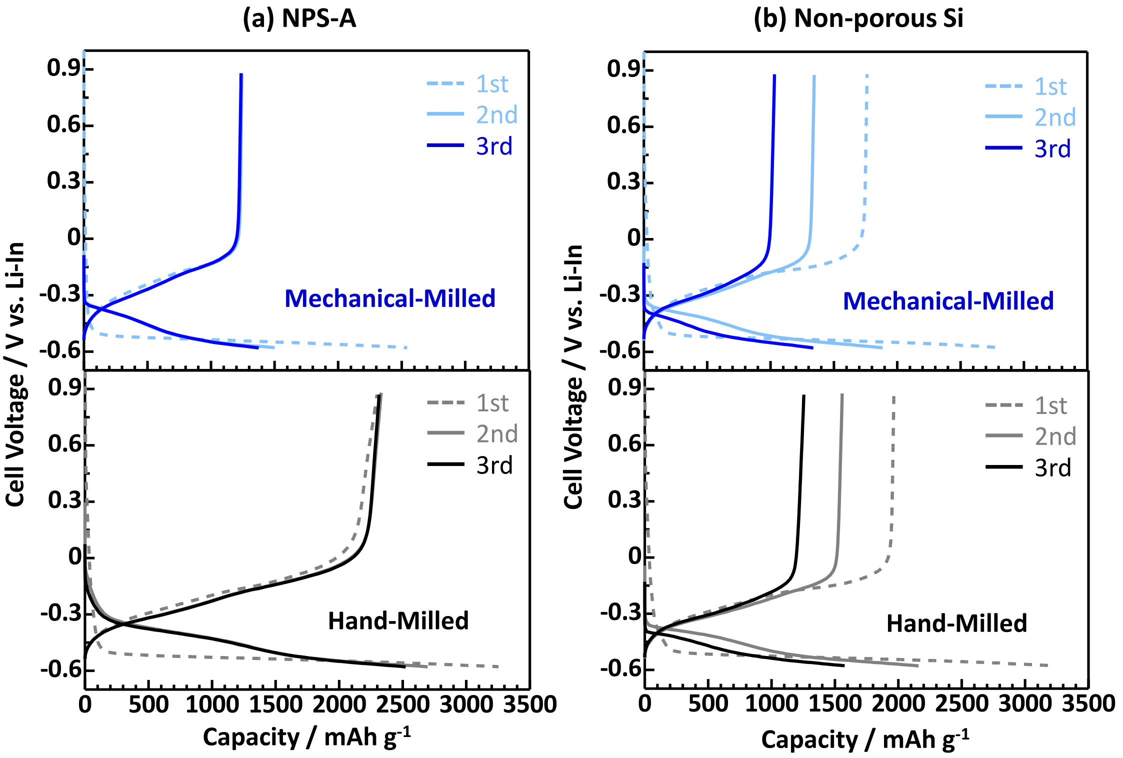

Figure 3-3. Charge and discharge curves of half cells with various Si composite anodes.

Table 3-1. Charge and discharge characteristics of half cells with various Si composite anodes.

Active Material	Mixing Method	Charge / Discharge Capacities (mAh g^{-1})			Coulombic Efficiency (%)		
		1st cycle	2nd cycle	3rd cycle	1st cycle	2nd cycle	3rd cycle
Nanoporous Si: NPS-A	Mechanical Milling	2543 / 1240	1510 / 1242	1375 / 1236	49	82	90
	Hand Milling	3259 / 2300	2696 / 2330	2523 / 2315	71	86	92
Non-porous Si	Mechanical Milling	2829 / 1761	1885 / 1344	1337 / 1031	62	71	77
	Hand Milling	3244 / 1964	2169 / 1557	1591 / 1255	61	72	79

respectively. These values are smaller than a theoretical capacity (4199 mAh g^{-1}) of $Li_{22}Si_5$ in its fully lithiated state. In this regard, it is important to understand the change in Li-Si alloy phase with the insertion of Li^+ ions. Although the crystalline phases normally have lower Gibbs free energy than their amorphous counterparts, the initial products in the electrochemical lithiation process are always amorphous Li_xSi (with $0<x<3.75$). Then, at $x=3.75$, the amorphous phase suddenly crystallizes to form $Li_{15}Si_4$ with a theoretical capacity of 3579 mAh g^{-1} [11]. This is the highest lithiated phase achievable at ambient temperature. In fact, initial charge capacities of around 3500 mAh g^{-1} have been confirmed in the case of many LIBs with liquid electrolytes [12]. Although the capacity of HM-NPS-A half cell is close to that of $Li_{15}Si_4$, there is a difference of 320 mAh g^{-1}. This is probably because some of Si particles/aggregates are not in contact with AB (conductive assistant). The large difference (>700 mAh g^{-1}) between the initial charge capacities of HM-NPS-A and MM-NPS-A half cells should be due to the same reason. In other words, AB with a volume fraction of 45% was possibly too small to construct the electronic conduction path for the highly dispersed Si particles in MM-NPS-A anode, as observed in the cross-sectional EDX mapping images. SiO_2 and SiO_x which were confirmed by XPS measurement (see Paragraph 2.3.2), also cause the observed low charge capacities. This is because Si oxides have the theoretical capacities as 1873, 749 mAh g^{-1}, and so on [13,14].

MM-NPS-A and HM-NPS-A half cells exhibited initial discharge capacities of 1240 mAh g^{-1} and 2300 mAh g^{-1}, corresponding to coulombic efficiency (CE) of 49% and 71%, respectively. I note the oxide layers as the origin of these low CE, because they irreversibly consume Li. The air-oxidation process in the preparation of NPS-A promotes the formation of the oxide layers. In particular, numerous oxide layers may be formed owing to the large specific surface area attributable to the nanoporous structure. The lower capacity (nearly half) of MM-NPS-A half cell compared to HM-NPS-A half cell is probably due to the contribution from the oxide layer and solid electrolyte interphase (SEI). In other words, the pulverization of Si particles by mechanical milling inevitably produces fresh surfaces for the regeneration of the oxide layer and SEI, resulting in excessive consumption of Li compared to HM-NPS-A half cell.

As shown in Figure 3-3(b) and Table 3-1, the discharge capacities of non-porous Si half cells, which were prepared as a reference, rapidly decreased as the number of cycles increased, regardless of the mixing method. The electrochemical deterioration is due to the large volume change in the alloying/dealloying process. Meanwhile, the discharge capacities of MM-NPS-A and HM-NPS-A half cells were nearly constant regardless of the increase in the number of cycles (Figure 3-3(a)). These results strongly suggest that the pores buffer the volumetric expansion of Si particles/aggregates, as discussed below. Here, the initial charge/discharge capacities of the half cells hand-milled separately using the same NPS-A were 3259/2300 mAh g^{-1} and 3213/2279 mAh g^{-1}. These results indicate that the reproducibility in experiments using hand-milling is high.

Figure 3-4 compares the cycle performance of half cells with various Si composite anodes, while Table 3-2 summarizes their discharge capacities and capacity retentions. The maximum discharge capacity is defined as the highest value after four cycles, which is measured in the constant current/constant voltage (CCCV) mode. The capacity retention is the ratio of the discharge capacity at the 150th cycle to the maximum discharge capacity. MM-NPS-A and HM-NPS-A half cells maintained the capacity retentions of 80% and 44%, respectively. Note that MM-NPS-A half cells with highly dispersed Si components achieved extremely high capacity retention. Regardless of the mixing method, the discharge capacities of NPS-A half cells were around three times higher than the theoretical discharge capacity of graphite (372 mAh g^{-1}) even at 150 cycles. Non-porous Si half cells used as a reference exhibited poorer cycle stability with a capacity retention of 19% or less. The increase in the discharge capacity at the fourth cycle for MM-NPS-A and HM-NPS-A half cells is due to the increase in the number of Si particles/aggregates responsible for charging and discharging in CCCV mode. The gradual increase in the discharge capacity from cycles 4 to 15 in MM-NPS-A half cell can be explained by a similar mechanism. Meanwhile, such an increase in the capacities was

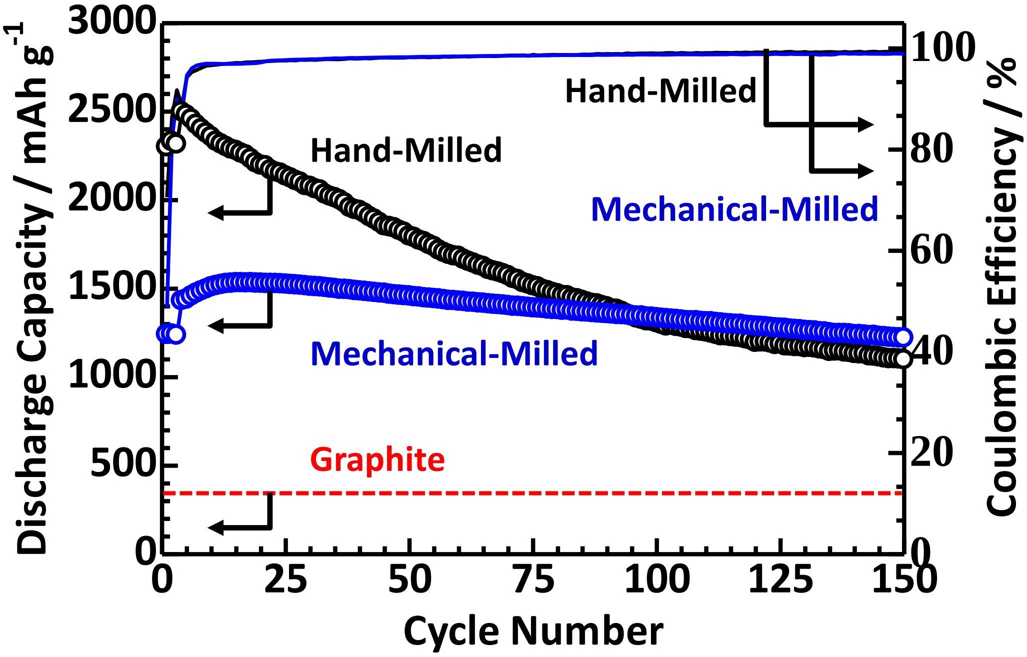

(a) NPS-A

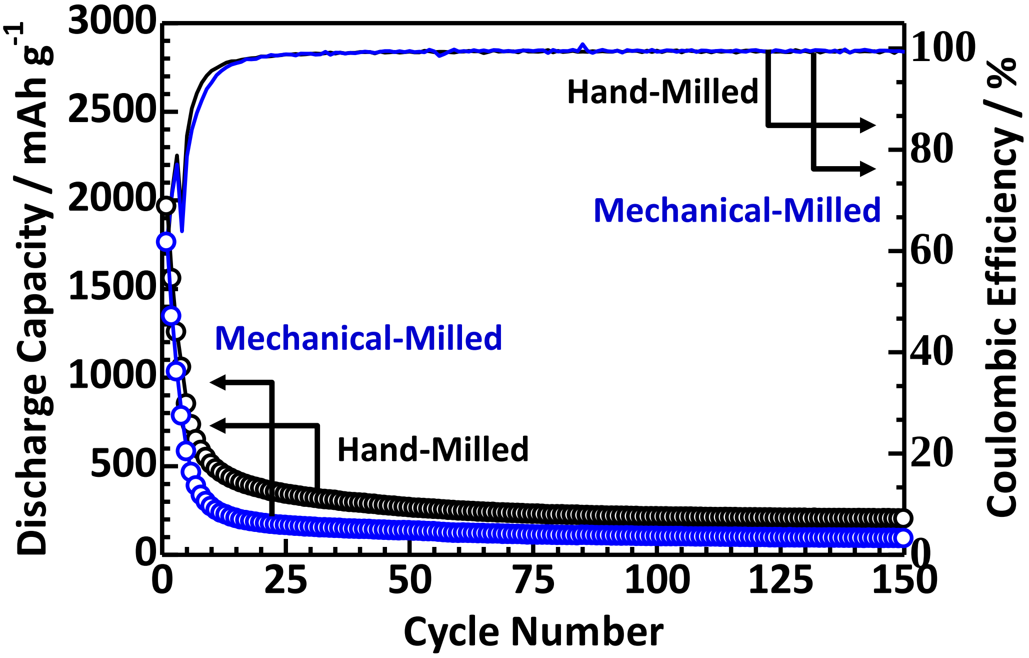

(b) Non-porous Si

Figure 3-4. Cycle performance of half cells with various Si composite anodes.

Table 3-2. Cycle performance of half cells with various Si composite anodes.

Active Material	Mixing Method	Maximum Discharge Capacity[*1] (mAh g^{-1})	Discharge Capacity at 150th cycle (mAh g^{-1})	Capacity Retention[*2] (%)
Nanoporous Si: NPS-A	Mechanical Milling	1532	1220	80
	Hand Milling	2498	1097	44
Non-porous Si	Mechanical Milling	782	90	12
	Hand Milling	1056	201	19

*1 Maximum discharge capacity is the highest discharge capacity after the fourth cycle.
*2 Capacity retention is the ratio of the discharge capacity at the 150th cycle to the maximum discharge capacity.

not observed in the case of non-porous Si half cells because of the large-scale and rapid deterioration.

Figure 3-5 shows Cole-Cole plots for MM-NPS-A and HM-NPS-A half cells. The horizontal and vertical axes represent the real and imaginary numbers of impedance components, respectively. The intersections with the real axis at 2 kHz can be attributed to the bulk and grain boundary resistance (R_{SE}) of SE, when the electrical conductivity in the electrodes is sufficiently high. The resistances (R_I) at the arcs from 2 kHz to 0.40 and 0.16 Hz correspond to the charge transfer at the interface between Si and SE [4]. The start point of the arc was determined by the intersection with the real axis. The end was the point where the imaginary number of impedance component changes from decreasing to increasing. In the first cycle, there was nearly no difference between R_I values of MM-NPS-A and HM-NPS-A anodes. However, in the 20th cycle, the increase in R_I was remarkable in the case of HM-NPS-A anode. This results in rapid capacity fading compared to MM-NPS-A anode. These findings suggest that the contact area between Si and SE rapidly decreases in the case of HM-NPS-A anode. In addition, HM-NPS-A anode shows a larger increase in R_{SE} with cycling, compared to MM-NPS-A anode. This is due to the structural relaxation in SE layers and/or the decrease in the electrical conductivity of Si composites.

The most important finding in the present study is the high capacity retention observed in MM-NPS-A half cell. Such excellent cyclability is not due to the size effect of Si particles. Through in-situ TEM studies, Liu showed that Si particles neither crack nor fracture upon lithiation below a particle diameter of 150 nm, which appears to be the size effect [15]. The mechanical-milled non-porous Si half cell with a particle size of 466 nm, which was measured by DLS, exhibited a low capacity retention of 12%. According to Liu's observation, this is probably due to the cracks and/or fractures. By contrast, MM-NPS-A half cell showed a high capacity retention over 80% at 150 cycles in spite of being 506 nm in diameter. These results strongly suggest that the nanoporous structure relaxes the volume change of Si components.

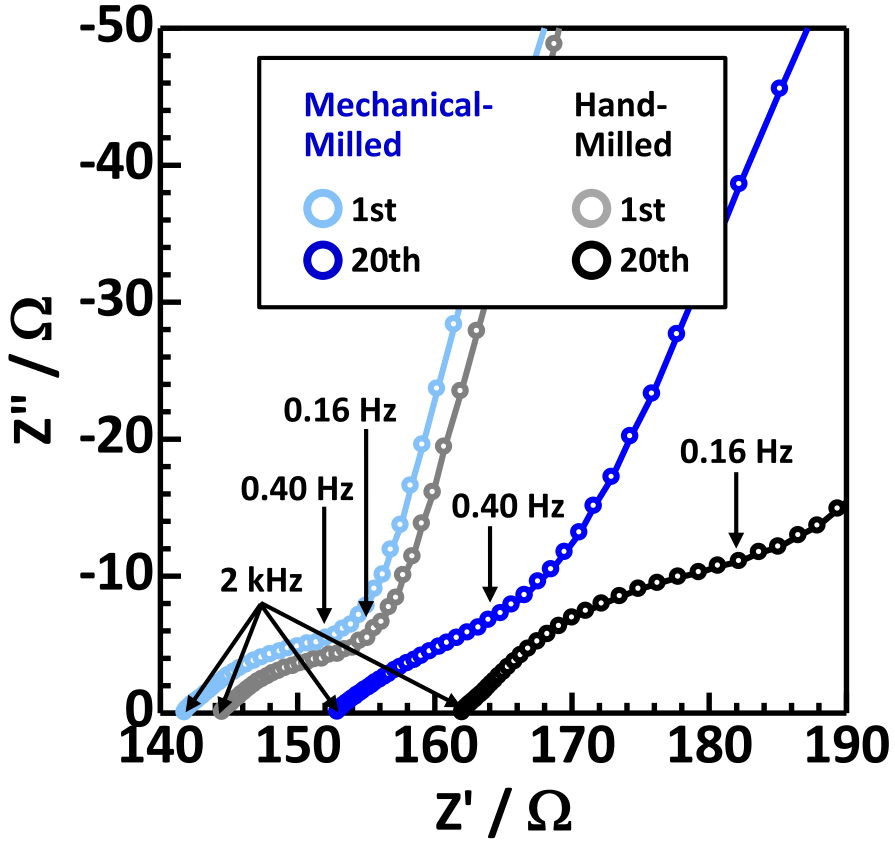

Figure 3-5. Cole-Cole plots of half cells with mechanical-milled and hand-milled NPS-A composite anodes.

The difference between the cycle performance of MM-NPS-A and HM-NPS-A half cells is due to the contact state between SE and NPS-A. Although the volumetric expansion is mainly buffered by the shrinkage of pores, NPS-A expand outward slightly during lithiation. In the case of high dispersion as in MM-NPS-A half cells (Figure 3-6(a)), the stress arising from the isolated Si particles is relieved by the elastic deformation of the surrounding SE. During delithiation, the elastically deformed SE reverts to its original shape and retains contact with each Si particle. Therefore, high capacity retention is maintained in MM-NPS-A half cells. By contrast, the micrometer-sized NPS-A aggregates in HM-NPS-A half cells expand outward considerably to afford significant stress to the surrounding SE, leading to plastic deformation. Thus, in the delithiation process, voids are formed between Si aggregates and the plastically deformed SE, resulting in lower capacity retention (Figure 3-6(b)). The occurrence of voids leads to a decrease in the contact area between Si and SE, which is consistent with the increase in the interfacial resistance indicated by EIS measurement results.

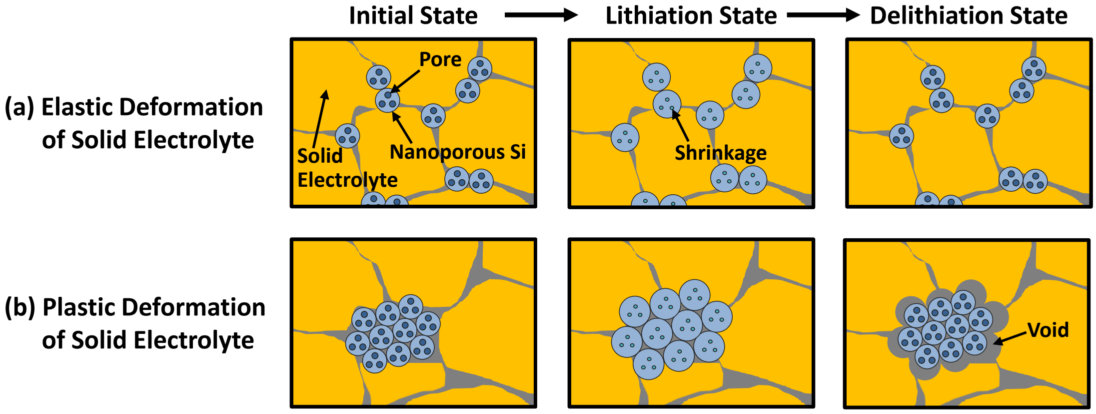

Figure 3-6. Microstructural behavior of (a) mechanical-milled and (b) hand-milled NPS-A composite anodes.

3.3. Composite Anodes comprising Nanoporous Si Particles Prepared by Mg_2Si Reduction of Mesoporous SiO_2

3.3.1. Experimental

Anode composite materials consisted of nanoporous Si particles (NPS-M; 36 wt%), SE (55 wt%), and AB (9 wt%). Mechanical milling was adopted as the mixing method. The fabrication processes of SE and half cells, and the measurement methods of structural and electrochemical characteristics are explained in Paragraph 3.2.1. The fabricated half cells had a high areal mass loading of 0.90 mg cm^{-2}, which is applicable to practical batteries.

3.3.2. Results and Discussion

Figure 3-7 shows the charge and discharge curves of NPS-M half cell during the first three cycles. The charge/discharge capacities and CE are summarized in Table 3-3, including NPS-A and non-porous Si half cells as references. The initial charge capacity, 2357 mAh g^{-1}, of NPS-M half cell was significantly smaller than the theoretical capacities, 4199 mAh g^{-1} and 3579 mAh g^{-1} [11], of the high-lithiated phases such as $Li_{22}Si_5$ and $Li_{15}Si_4$, respectively. This result is due to two reasons. First, the amount of conductive assistant is possibly too small to construct the electronic conduction path for highly dispersed Si particles/aggregates in the mechanical-milled NPS-M composite anodes. As a result, the isolated Si cannot contribute to the charging. Second, Si oxides having the theoretical capacities as 1873, 749 mAh g^{-1}, and so on are present inside or on the surface of Si particles [13,14]. This is reasonable because the signals from SiO_2 and SiO_x are clearly observed in XPS profile, as shown in Paragraph 2.3.2. On the other hand, the initial discharge capacity was 1394 mAh g^{-1}, corresponding to 59% CE. The low CE is due to Si oxide and SEI which consume Li irreversibly. As shown in Table 3-3, the discharge capacities of non-porous Si half cell decreased drastically from 1761 mAh g^{-1} to 1031 mAh g^{-1} in only three cycles. On the other hand, those of NPS-M half cell

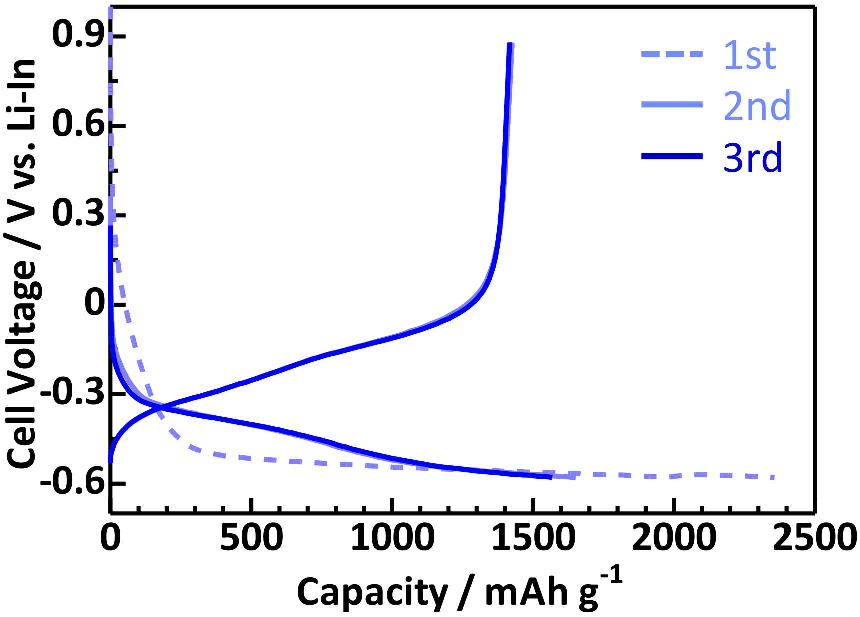

Figure 3-7. Charge and discharge curves of NPS-M half cell.

Table 3-3. Charge and discharge characteristics of half cells with various Si composite anodes.

Active Material	Mixing Method	Charge / Discharge Capacities ($mAh\ g^{-1}$)			Coulombic Efficiency (%)		
		1st cycle	2nd cycle	3rd cycle	1st cycle	2nd cycle	3rd cycle
Nanoporous Si: NPS-M	Mechanical Milling	2357 / 1394	1651 / 1426	1568 / 1416	59	86	90
Nanoporous Si: NPS-A	Mechanical Milling	2543 / 1240	1510 / 1242	1375 / 1236	49	82	90
Non-porous Si	Mechanical Milling	2829 / 1761	1885 / 1344	1337 / 1031	62	71	77

remained constant regardless of the increase in the number of cycles, similar to NPS-A half cell. These results indicate that the nanoporous structure buffers the volume expansion of Si particles/aggregates.

Figure 3-8 shows the cycle performance of NSP-M half cell, including NPS-A and non-porous Si half cells as references. Table 3-4 summarizes their discharge capacities and capacity retentions. The maximum discharge capacity is defined as the highest discharge capacity after four cycles. The capacity retention is the ratio of the discharge capacity at the 150th cycle to the maximum discharge capacity. As expected, the cycle stability of NPS-M half cell was extremely superior to that of non-porous Si half cell. Namely, the discharge capacity in NPS-M half cell was maintained to obtain the capacity retention of 63% after 150 cycles. As a result, the discharge capacity of 1058 mAh g^{-1} was about 12 and 3 times higher than the observed capacity of non-porous Si (90 mAh g^{-1}) and a theoretical capacity of graphite (372 mAh g^{-1}), respectively. As discussed in Paragraph 3.2.2, such an excellent cyclability is not due to the size effect proposed by Liu. This is because their critical size is less than 150 nm in diameter [15], whereas the size of Si particles/aggregates in NPS-M half cell was estimated to be 354 nm by DLS. These experimental results were almost the same as those obtained in NPS-A half cells. Therefore, the pores of Si particles should effectively mitigate the volume change.

Figure 3-9 shows Cole-Cole plots for NPS-M and non-porous Si half cells. The charge transfer resistance (R_I) at Si-SE interface in NPS-M half cell were 8 Ω and 22 Ω at 1st and 20th cycles, respectively. These small values indicate that the good contact state between Si and SE hardly changes with the increase of cycle number. On the other hand, in non-porous Si half cell, R_I value considerably increased from 30 Ω to 190 Ω. This results in rapid capacity fading, corresponding to poor cycle performance (see Figure 3-8). Figure 3-10 shows the cross-sectional SEM and EDX images of both half cells at the 50th cycle. In EDX mapping images, Si, S, and C are colored in blue, yellow, and red, respectively. Referring to Figure 3-10(a) and (c), I found that Si particles/aggregates entangle the surrounding SE in NPS-M half cell. As the result, microcracks are generated

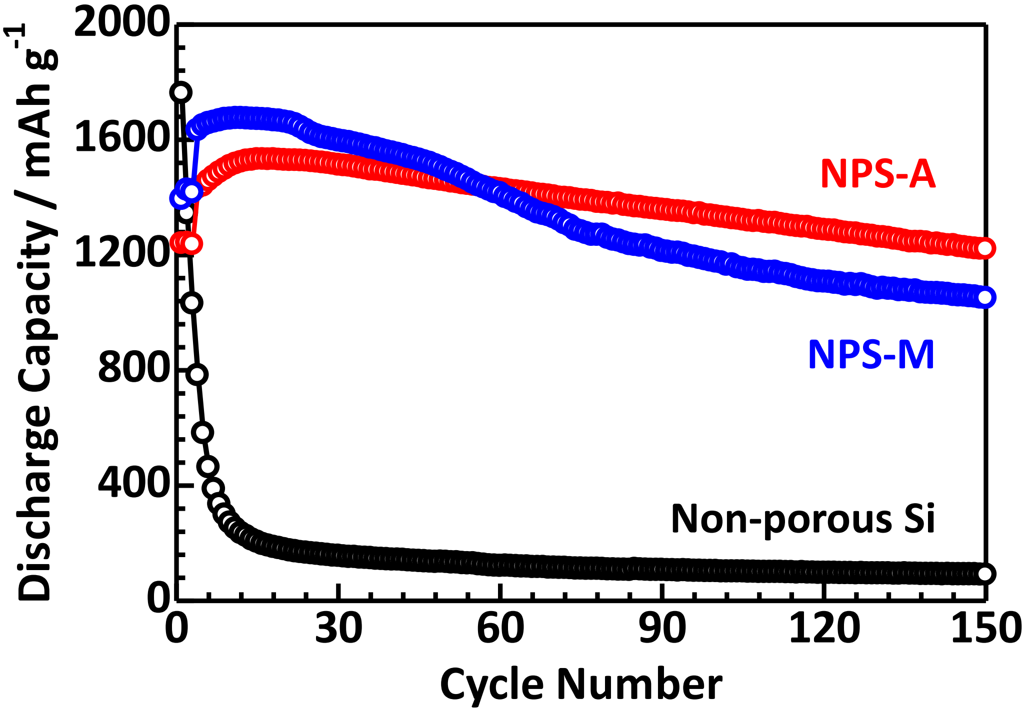

Figure 3-8. Cycle performance of half cells with various Si composite anodes.

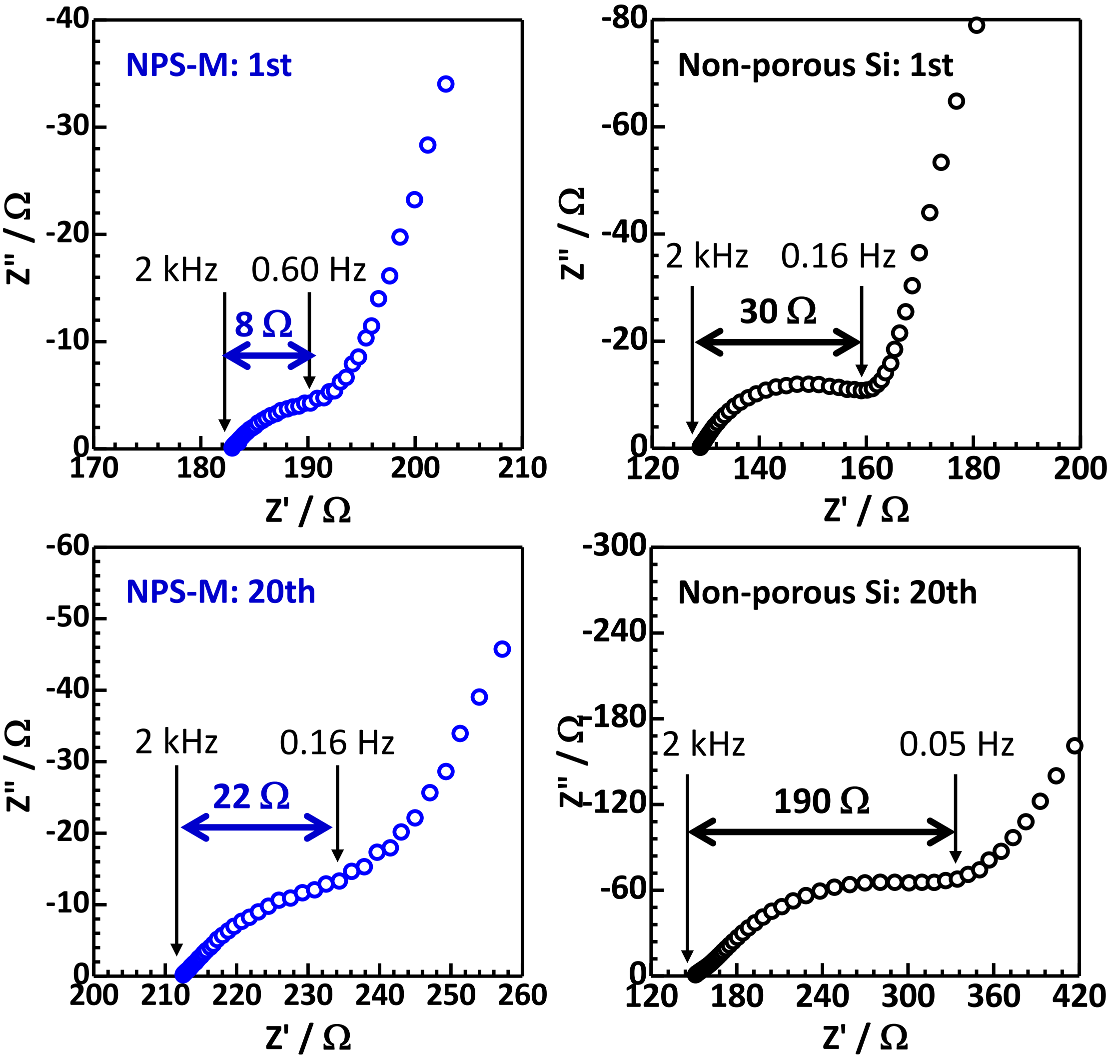

Figure 3-9. Cole-Cole plots of NPS-M and non-porous Si half cells.

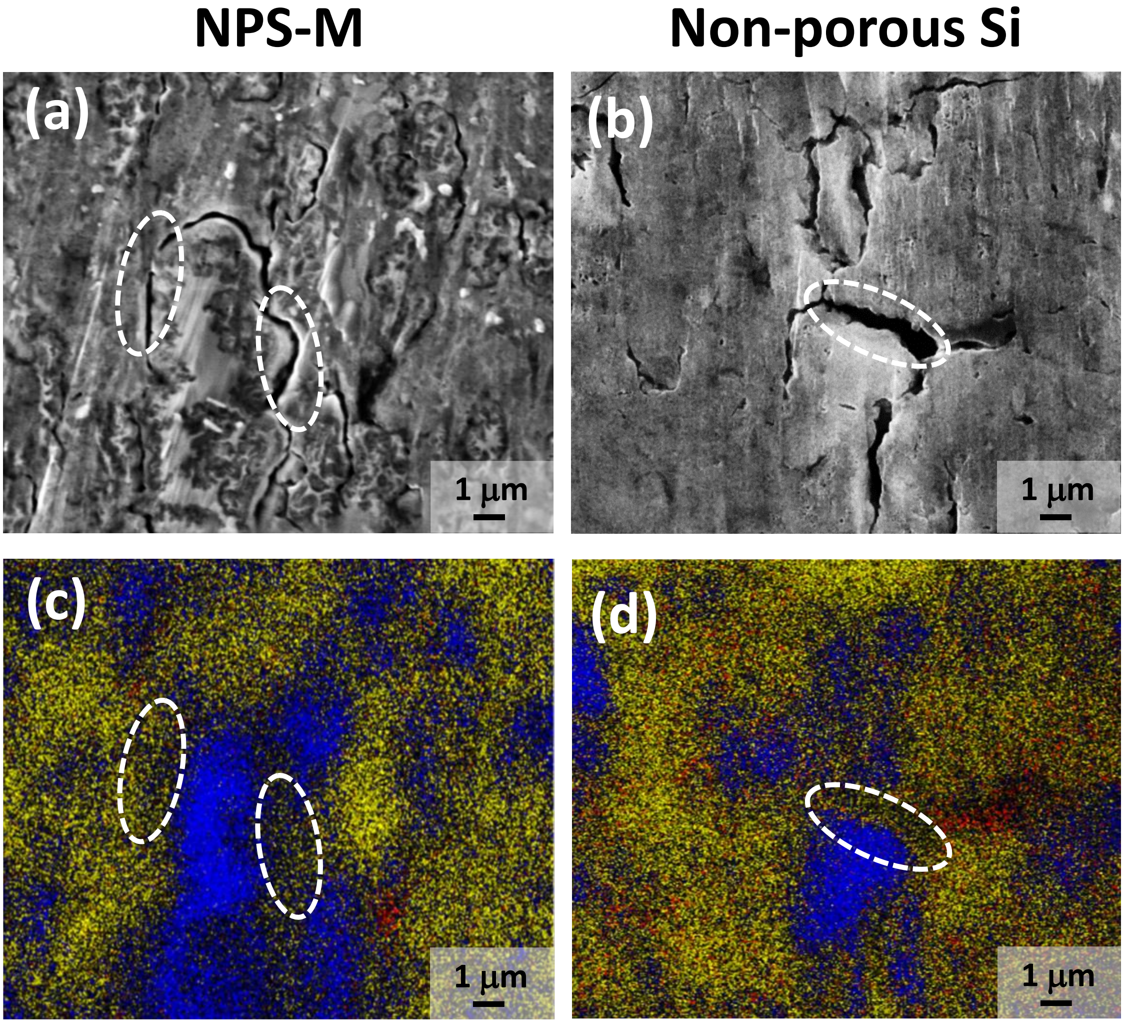

Figure 3-10. (a, b) Cross-sectional SEM images and (c, d) EDX mapping images of NPS-M and non-porous Si composite anodes. Dashed ellipses represent cracks. In EDX mapping images, Si, S, and C are colored in blue, yellow, and red, respectively.

Table 3-4. Cycle performance of half cells with various Si composite anodes.

Active Material	Mixing Method	Maximum Discharge Capacity*1 (mAh g^{-1})	Discharge Capacity at 150th cycle (mAh g^{-1})	Capacity Retention*2 (%)
Nanoporous Si: NPS-M	Mechanical Milling	1674	1058	63
Nanoporous Si: NPS-A	Mechanical Milling	1532	1220	80
Non-porous Si	Mechanical Milling	782	90	12

*1 Maximum discharge capacity is the highest discharge capacity after the fourth cycle.
*2 Capacity retention is the ratio of the discharge capacity at the 150th cycle to the maximum discharge capacity.

not at Si-SE interface but inside SE, as shown by dashed ellipses. These microstructural features are consistent with the invariant interfacial resistance, R_I, in EIS measurement. Since SE is originally high in conductivity, microcracks have negligible effect on the electrochemical characteristics. Therefore, the high capacity retention was achieved in NPS-M half cells. On the other hand, many large cracks were observed in non-porous Si half cells. It is worthy to note that they are formed at the boundary between Si and SE grains (see the dashed ellipses in Figure 3-10(b) and (d)). This finding is fully consistent with the marked increase in R_I, resulting in the low capacity retention.

3.4. Composite Anodes comprising Nanoporous Si Particles Prepared by Mg_2Si Reduction of SiO_2 Fume

3.4.1. Experimental

Anode composite materials consisted of nanoporou Si particles (NPS-F; 36 wt%), SE (55 wt%), and AB (9 wt%). Mechanical milling was adopted as the mixing method. The fabrication processes of SE and half cells, and the measurement methods of structural and electrochemical characteristics are explained in Paragraph 3.2.1. The fabricated half cells had a high areal mass loading of 0.90 mg cm^{-2}, which is applicable to practical batteries.

3.4.2. Results and Discussion

Figure 3-11 shows the charge and discharge curves of NPS-F half cell during the first three cycles. The charge/discharge capacities and CE are summarized in Table 3-5, including NPS-M, NPS-A, and non-porous Si half cells as references. Among the half cells with three kinds of nanoporous Si composite anodes, NPS-F half cell showed the highest charge capacity, discharge capacity, and CE at all the cycles. The rate characteristics of nanoporous Si half cells are shown in Figure 3-12. NPS-F half cell also exhibited the best rate characteristics, achieving the reversible capacities of 2380 mAh g^{-1}, 2221 mAh g^{-1}, 2060 mAh g^{-1}, and 1680 mAh g^{-1} at the current densities of 0.3 mA cm^{-2}, 0.75 mA cm^{-2}, 1.5 mA cm^{-2}, and 3.0 mA cm^{-2}, respectively. These values were 6.4, 6.0, 5.5, and 4.5 times higher than the theoretical capacity of graphite (372 mAh g^{-1}), respectively. Figure 3-13 compares the cycle performance of half cells with various Si composite anodes, while Table 3-6 summarizes their discharge capacities and capacity retentions. The first three cycles were measured using CC mode. CCCV mode was used after the fourth cycle. The maximum discharge capacity is defined as the highest value after four cycles. The capacity retention is the ratio of the discharge capacity at the 150th cycle to the maximum discharge capacity. The discharge capacity of 1323 mAh g^{-1} in

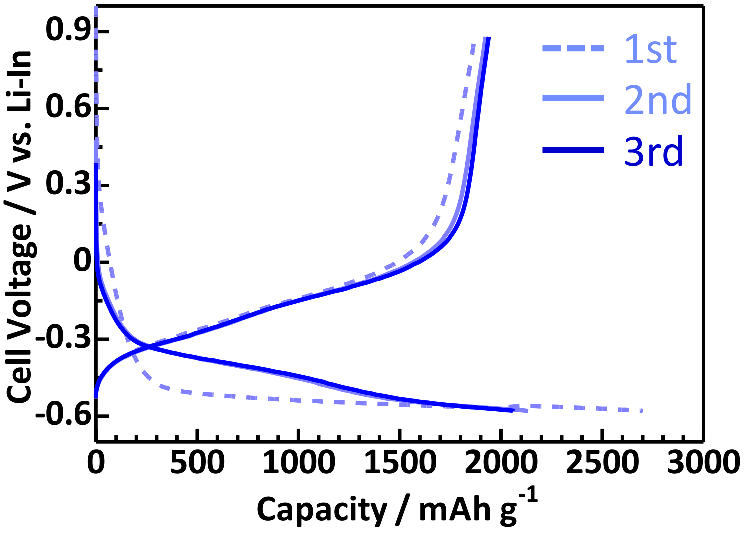

Figure 3-11. Charge and discharge curves of NPS-F half cell.

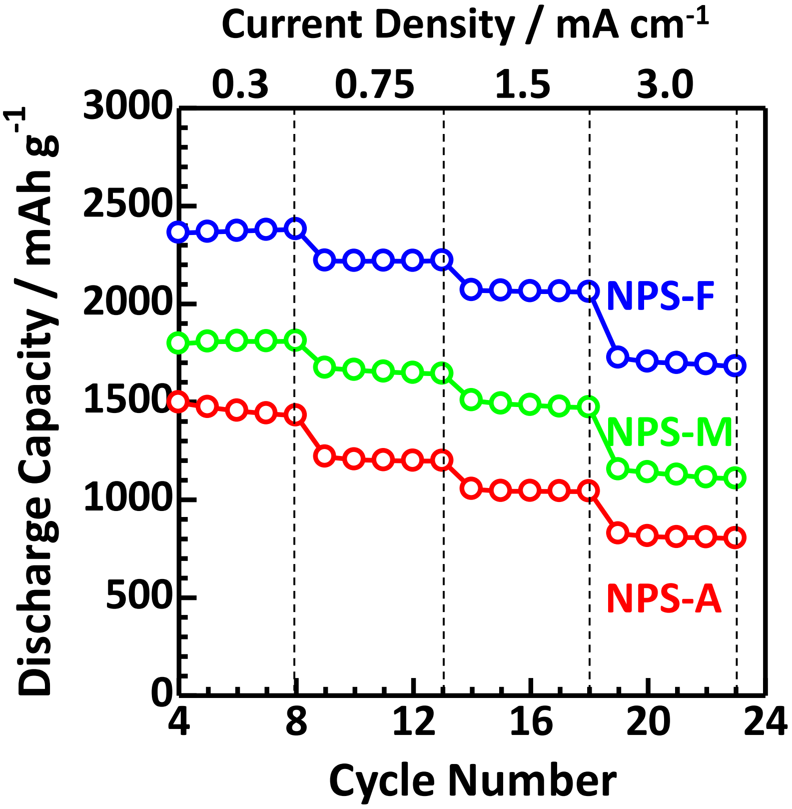

Figure 3-12. Rate performance of half cells with various Si composite anodes.

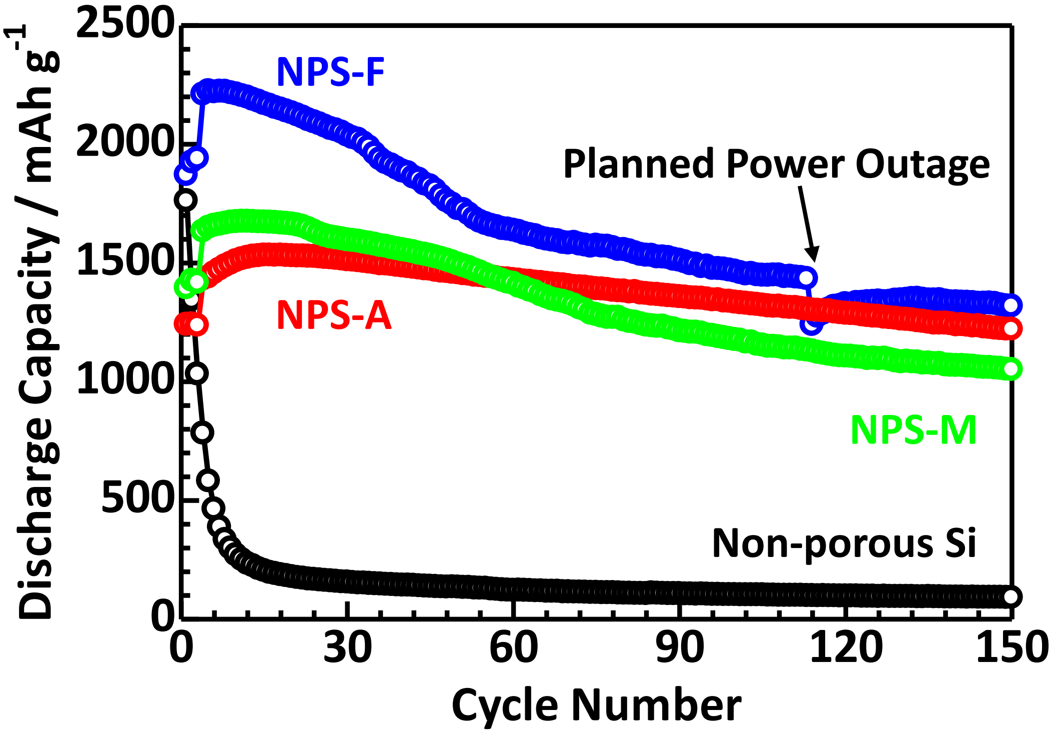

Figure 3-13. Cycle performance of half cells with various Si composite anodes.

Table 3-5. Charge and discharge characteristics of half cells with various Si composite anodes.

Active Material	Mixing Method	Charge / Discharge Capacities ($mAh\ g^{-1}$)			Coulombic Efficiency (%)		
		1st cycle	2nd cycle	3rd cycle	1st cycle	2nd cycle	3rd cycle
Nanoporous Si: NPS-F	Mechanical Milling	2700 / 1871	2135 / 1924	2063 / 1940	69	90	94
Nanoporous Si: NPS-M	Mechanical Milling	2357 / 1394	1651 / 1426	1568 / 1416	59	86	90
Nanoporous Si: NPS-A	Mechanical Milling	2543 / 1240	1510 / 1242	1375 / 1236	49	82	90
Non-porous Si	Mechanical Milling	2829 / 1761	1885 / 1344	1337 / 1031	62	71	77

Table 3-6. Cycle performance of half cells with various Si composite anodes.

Active Material	Mixing Method	Maximum Discharge Capacity[*1] (mAh g^{-1})	Discharge Capacity at 150th cycle (mAh g^{-1})	Capacity Retention[*2] (%)
Nanoporous Si: NPS-F	Mechanical Milling	2224	1323	60
Nanoporous Si: NPS-M	Mechanical Milling	1674	1058	63
Nanoporous Si: NPS-A	Mechanical Milling	1532	1220	80
Non-porous Si	Mechanical Milling	782	90	12

*1 Maximum discharge capacity is the highest discharge capacity after the fourth cycle.

*2 Capacity retention is the ratio of the discharge capacity at the 150th cycle to the maximum discharge capacity.

NPS-F half cell at the 150th cycle was approximately 1.3, 1.1, 15 and 3.6 times higher than the observed capacity of NPS-M (1058 mAh g^{-1}), NPS-A (1220 mAh g^{-1}), non-porous Si (90 mAh g^{-1}) and theoretical capacity of graphite (372 mAh g^{-1}), respectively. In addition, the capacity retention of NPS-F half cell (60%) was extremely larger than that of non-porous Si half cell (12%). The diameter of NPS-F was estimated as 479 nm by DLS; this excellent cycling property is not attributed to the size effect that occurs at diameter below 150 nm [15]. The experimental results of NPS-F, NPS-M, and NPS-A half cells conclude that the nanoporous structure effectively relieves the large volume change of Si during charge and discharge.

Based on the structural data estimated by DLS, BET, and XPS analyses (Table 3-7), the electrochemical characteristics of NPS-F, NPS-M, and NPS-A half cells are explained as follows. The intensity of O1s signals in XPS profiles reflects the amount of oxides near the surface of Si particles. Therefore, NPS-A with O1s intensity of 55350 cps contains a lot of Si oxides. Here, the theoretical capacities of Si oxides are smaller than that of Si [13,14]. Therefore, it is reasonable that the initial charge capacity of NPS-A half cell is smaller than that of NPS-F half cell. On the other hand, the initial charge capacity of NPS-M half cell, which has the similar O1s intensity as NPS-F, is the smallest among three kinds of half cells. This is probably due to the fact that the particle size of NPS-M (354 nm) is obviously smaller than those of NPS-F (479 nm) and NPS-A (506 nm). Such small Si particles that are not in contact with the conductive additive cannot involve in charging and discharging. Regarding CE, it should be noted that Si oxides form several Li oxides (Li_2O, Li_4SiO_4, and $Li_2Si_2O_5$) during charging. These do not show the reversible reactions. Therefore, NPS-F half cell with the smallest O 1s intensity (14431 cps) has less loss of Li^+ ions, resulting in the largest initial CE (69%). As shown in Tables 3-6 and 3-7, the larger the pore size, the higher the capacity retention. In NPS-A half cell, where the pore size is 9.4 nm, the volume change during charging and discharging is mostly mitigated by the shrinkage and expansion of the pores. On the other hand, in NPS-F half cell with a small pore size (5.9 nm), the volume change that cannot be absorbed causes plastic

Table 3-7. Structural data of NPS-F, NPS-M, and NPS-A.

Active Material	Mixing Method	Intensity of O 1s (cps)	Particle Size (nm)	Pore Size (nm)
Nanoporous Si: NPS-F	Mechanical Milling	14431	479	5.9
Nanoporous Si: NPS-M	Mechanical Milling	14824	354	6
Nanoporous Si: NPS-A	Mechanical Milling	55350	506	9.4
Non-porous Si	Mechanical Milling	37984	466	-

deformation of the surrounding SE. As a result, voids generated at Si-SE interface decrease the capacity retention.

Figure 3-14 shows Cole-Cole plots for NPS-F and non-porous Si half cells. The resistances at the arcs from 2 kHz to 0.40, 0.16, and 0.05 Hz correspond to the charge transfer resistance (R_I) at the interface between Si and SE [4]. In NPS-F half cell, R_I was constant at 16 Ω for the 1st and 20th cycles, whereas in non-porous Si half cell, the value increased considerably from 30 Ω to 190 Ω. Thus, the contact area between Si and SE decreased in non-porous Si half cell but not in NPS-F half cell. The increase in R_I for the non-porous half cell resulted in the capacity fading, which is consistent with the poor cycle performance shown in Figure 3-13. Figure 3-15 shows the cross-sectional SEM and EDX images of NPS-F and non-porous Si half cells at the 50th cycle. In EDX mapping images, Si, S, and C are shown in blue, yellow, and red, respectively. Based on the magnified SEM and EDX images of NPS-F half cell, I found that Si particles/aggregates entangle the surrounding SE. As a result, microcracks are generated not at Si-SE interface but inside SE, as shown by dashed ellipses. These microstructural features are consistent with the invariant interfacial resistance, R_I, in EIS measurement. As SE is intrinsically high in conductivity, microcracks have a negligible effect on its electrochemical characteristics. Therefore, the high capacity retention was achieved in NPS-F half cell. On the other hand, large cracks were observed in non-porous Si half cell; notable, these formed at the boundary between Si and SE grains (see the dashed ellipses in Figure 3-10(b) and (d)). This result is in perfect agreement with a considerable increase in R_I, resulting in low capacity retention.

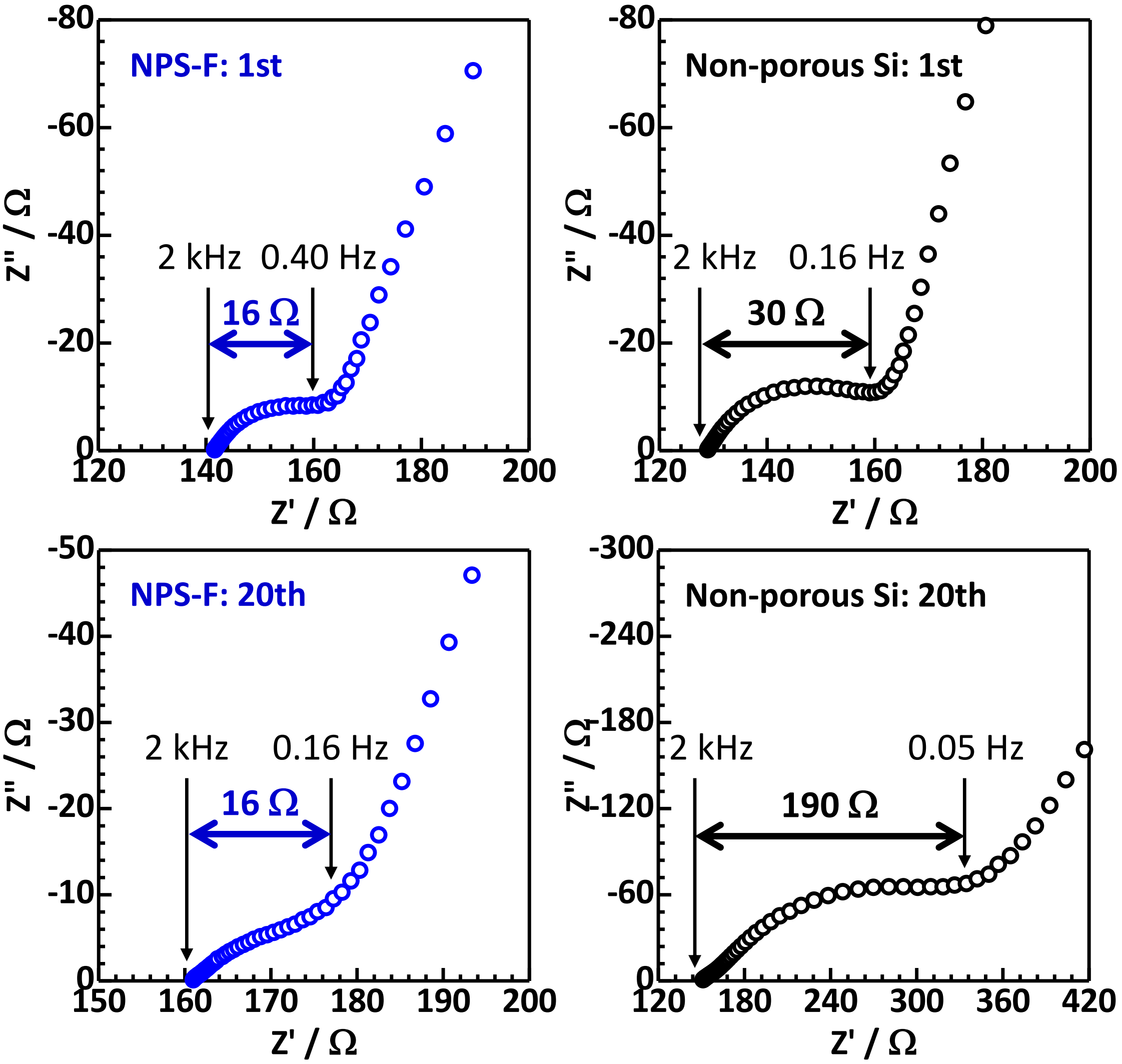

Figure 3-14. Cole-Cole plots of NPS-F and non-porous Si half cells.

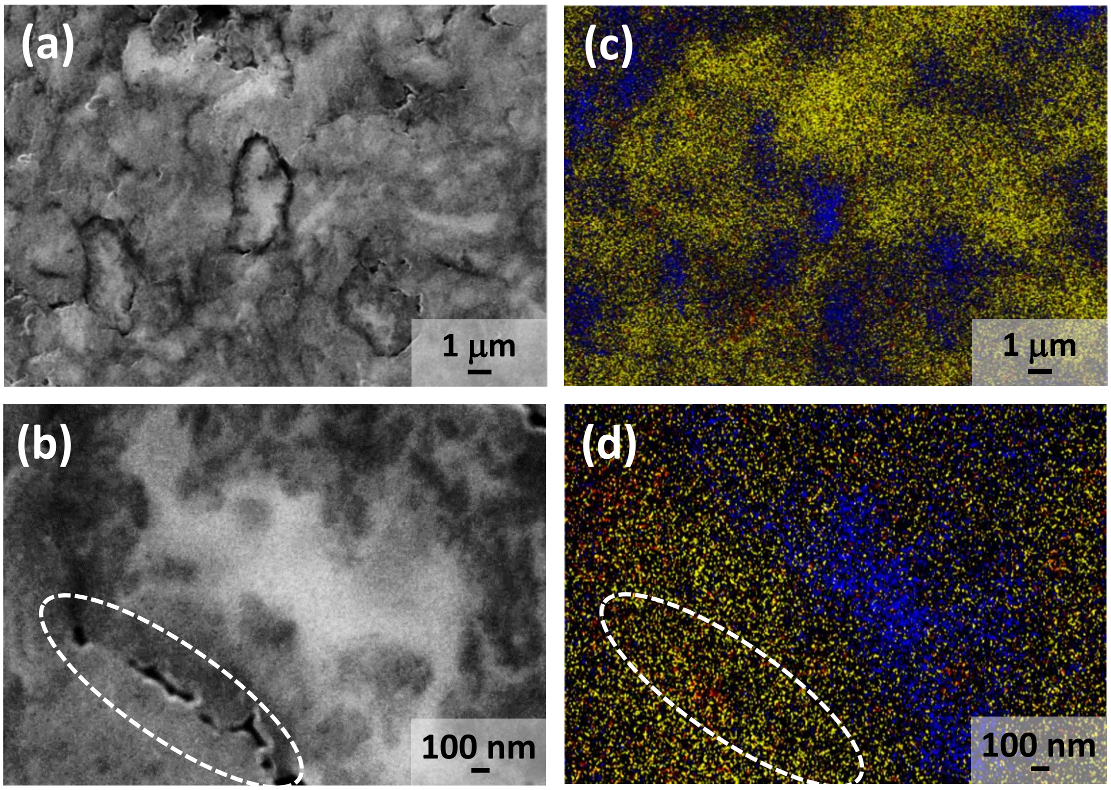

Figure 3-15. (a, b) Cross-sectional SEM images and (c, d) EDX mapping images of NPS-F composite anode. Dashed ellipses represent microcracks. In EDX mapping images, Si, S, and C are colored in blue, yellow, and red, respectively.

3.5. Summary

The electrochemical and structural studies on NPS-A, NPS-M, NPS-F, and non-porous Si half cells demonstrated that nanoporous structure acted as the buffer regions for large volume change of Si particles/aggregates during charge and discharge. Namely, the volume expansion of Si during lithiation is mainly buffered by the shrinkage of pores. The stress from Si expanded slightly outward is relieved by elastic deformation of the surrounding SE. During delithiation, the elastically deformed SE returns to its original shape and retains contact with Si particles/aggregates. The good response to volume change is possibly owing to the low Young's modulus (22.9 GPa) of $75Li_2S{\cdot}25P_2S_5$ solid electrolyte used in this study.

The important achievements are as follows:

1) 3.6 times higher discharge capacities versus graphite at 150th cycles

2) 15 times higher discharge capacities versus non-porous Si at 150th cycles

3) Capacity retentions of 80% at 150th cycles

Here, anode composite materials were prepared by simply mixing nanoporous Si particles, SE, and conductive additive. In addition, the half cells possessed a simple three-layered structure; anode composite material, SE, and Li-In counter electrode were pressed in an electric insulation tube. Therefore, there are the advantages in the manufacturing cost and handling compared to other Si-based cells.

Excellent electrochemical properties were obtained by using nanoporous Si particles under the following conditions:

a) O 1s intensity in XPS profile: small (large capacity, large CE)

b) Particle size: large (large capacity)

c) Pore size: large (high capacity retention)

d) Dispersibility in composites: high (high capacity retention)

The small intensity of O1s signals in XPS profiles indicates that there are few oxides near the surface of Si particles. Therefore, Mg_2Si reduction of SiO_2 is more suitable for the preparation of nanoporous Si particles compared with the air oxidation of Mg_2Si. On the other hand, the air oxidation of Mg_2Si is appropriate to increase the particle size and pore size of nanoporous Si. As the result, it is necessary to explore a new preparation process that satisfies all the requirements. In order to increase the dispersibility of Si particles, mechanical milling should be used to mix the composite materials. The findings described above provide valuable information to design Si-based composite anodes for ASSLIBs, enabling them to meet the energy demands of next-generation applications.

References

[1] J. E. Trevey, K. W. Rason, C. R. Stoldt, and S. H. Lee, *ECS Solid State Lett.*, **13** (2010) A154-A157.

[2] R. Miyazaki, N. Ohta, T. Ohnishi, I. Sakaguchi, and K. Takada, *J. Power Sources*, **272** (2014) 541-545.

[3] A. Kato, M. Yamamoto, A. Sakuda, A. Hayashi, and M. Tatsumisago, *ACS Appl. Energy Mater.*, **1** (2018) 1002-1007.

[4] M. Yamamoto, Y. Terauchi, A. Sakuda, and M. Takahashi, *J. Power Sources*, **402** (2018) 506-512.

[5] D. M. Piper, T. A. Yersak, and S. H. Lee, *J. Electrochem. Soc.*, **160** (2013) A77-A81.

[6] J. Saint, M. Morcrette, D. Larcher, L. Laffont, S. Beattie, J. P. Pérès, D. Talaga, M. Couzi, and J. M. Tarascon, *Adv. Funct. Mater.*, **17** (2007) 1765-1774.

[7] S. B. Son, S. C. Kim, C. S. Kang, T. A. Yersak, Y. C. Kim, C. G. Lee, S. H. Moon, J. S. Cho, J. T. Moon, K. H. Oh, and S. H. Lee, *Adv. Energy Mater.*, **2** (2012) 1226-1231.

[8] J. M. Whiteley, J. W. Kim, D. M. Piper, and S. H. Lee, *J. Electrochem. Soc.*, **163** (2016) A251-A254.

[9] N. A. Dunlap, S. Kim, J. J. Jeong, K. H. Oh, and S. H. Lee, *Solid State Ion.*, **324** (2018) 2017-217.

[10] A. Kato, M. Nose, M. Yamamoto, A. Sakuda, A. Hayashi, and M. Tatsumisago, *J. Ceram. Soc. Jpn.*, **126** (2018) 719-727.

[11] M. Gu, Z. Wang, J. G. Connell, D. E. Perea, L. J. Lauhon, F. Gao, and C. Wang, *ACS Nano*, **7** (2013) 6303-6309.

[12] J. P. Maranchi, A. F. Hepp, and P. N. Kumta, *ECS Solid State Lett.*, **6** (2003) A198-A201.

[13] B. Guo, J. Shu, Z. Wang, H. Yang, L. Shi, Y. Liu, and L. Chen, *Electrochem Commun.*, **10** (2008) 1876-1878.

[14] Q. Sun, B. Zhang, and Z. W. Fu, *Appl. Surf. Sci.*, **254** (2008) 3774-3779.

[15] X. H. Liu, L. Zhong, S. Huang, S. X. Mao, T. Zhu, and J. Y. Huang, *ACS Nano*, **6** (2012) 1522-1531.

4. FURTHER EFFORTS FOR PRATICAL APPLICATION

4.1. Introduction

As shown in Chapter 3, the charge capacities of NPS-A, NPS-M, and NPS-F half cells were smaller than the theoretical capacities of the highly lithiated states: $Li_{22}Si_5$ and $Li_{15}Si_4$. In addition, there was a large difference in the charge capacity between the mechanical-milled and hand-milled NPS-A half cells. To understand these experimental results, I proposed a mechanism, in which some of Si particles/aggregates are not in contact with conductive additives (CAs). CAs are generally used to form the effective electrical network among the embedded active materials throughout the electrode [1-3]. Their remarkable effect has been confirmed in cathodes [4-6] and graphite anodes [7,8]. On the other hand, there are few studies on Si anodes. The performance of Si anodes was investigated by adopting graphite flakes or nano-sized carbon black (CB) of 15wt% and 30 wt% [9]. Cyclic voltammetry and charge-discharge tests established that the cycle life and irreversible capacity increased and decreased, respectively, with increasing additive content. Using reduced graphene oxide or graphite nanoplatelets as CA brought pronounced improvement of the electrochemical performance for electrodes prepared with high active mass loading of Si nanoparticles (2.5 mg of Si cm^{-2}) [10,11]. CE (up to 99.9% versus 98.5% for CB), and cycle life (more than 500 cycles versus less than 400 for CB) were improved with a capacity limitation of 1200 mAh g^{-1}. Upon cycling without capacity limitation, high discharge capacity was maintained at 1800 mAh g^{-1} after 200 cycles (versus less than 1000 mAh g^{-1} for CB). Karkar prepared Si-based anodes of various areal capacities using different CAs (CB, carbon nanofibers, and carbon nanoplatelets) [12]. The sensitivity of cycling performance to the active mass loading was significant, with a major decrease of the capacity retention with increasing the loading in all cases. Regarding a challenge associated with electrical conduction, Si particles have been also coated with several conductive materials. Yoshio demonstrated that graphite coating of Si by thermal vapor deposition enabled tens cycles to be sustained at charging depths up to 1000 mAh g^{-1} [13]. This performance was far superior to non-coated Si that gave a cycle life of typically less than a few cycles. Dimov synthesized C-coated Si by a thermal vapor deposition method using Si powder and toluene/benzene vapors carried by N_2 gas [14]. The materials showed a high reversible capacity over 600 mAh g^{-1} for the first 25 cycles. The benzene or toluene vapors as reactants decomposed on the surface of the mechanically milled mixture of Si and graphite to form the C-coating layer [15]. Composite anodes containing C-coated Si (90%) and PVDF binder (10%) could be cycled at high current density (1.5 mA cm^{-2}) for several dozens of cycles. All the previous studies described above were done on Si anodes in LIBs using liquid electrolytes. In this chapter, the effect of CA on the performance, particularly conductivity and capacity, was examined using ASSLIBs with nanoporous Si composite anodes.

In Chapter 3, based on the cyclic characteristics of NPS-A, NPS-M, and NPS-F half cells, I demonstrated that nanoporous structures were effective to accommodate the large volumetric change of Si. From the viewpoint of practical application, it is important to quantitatively evaluate the stress caused by Si anodes. Piper systematically investigated the electrochemical performance of Si anodes as a function of externally applied compressive stress using all-solid-state cells [16]. The volume confinement of Si particles was manifested as an overpotential, resulting in a stable anode for LIBs. Applying finite element model to ASSLIBs, Bucci predicted that stresses up to 2 GPa induced 64% of capacity loss for Si composite anodes [17]. Increasing the volume ratio of Si beyond 25-30% decreased the total capacity, because of the interaction between neighboring particles. The electrochemical measurements of ASSLIBs were performed under varying external pressures (140, 20, and 5 MPa) upon cycling [18]. At 20 MPa, Si composite anodes using micro-sized Si and polyvinylidene fluoride showed marginal degradation of performance. Here, the effect of the counter cathode is ignored in the previous studies described above. In order to strictly discuss the stress, the electrochemical characteristics should be evaluated by full cell configuration. In this chapter, the structural stress from nanoporous

Si particles was quantitatively measured using full cells equipped with a load cell.

4.2. Optimization of Conduction Path using Conductive Additive

4.2.1. Experimental

Anode composite materials, in which the weight ratio of nanoporous Si particles (NPS-F), SE, and CA (acetylene black: AB) was 4:6:x (x=1, 2, 3, and 4), were prepared by the method described in Paragraph 3.2.1. Mechanical milling was adopted as the mixing method. The fabrication processes of SE and half cells are also explained in Paragraph 3.2.1.

To measure I-V curves from -0.05 to 0.05 V at 0.01 V intervals, the anode composite materials (80 mg) were inserted between two stainless steel disks in an insulation tube under 333 MPa. Electrical conductivity was calculated using the following equation:

$$\sigma = G \times \frac{L}{A}$$

where σ: electrical conductivity (S cm^{-1}), G: slope of I-V curve (Ω), L: thickness (cm), and A: area (cm^2). The measurement methods of structural and electrochemical characteristics are described in Paragraph 3.2.1.

4.2.2. Results and Discussion

Figure 4-1 shows the cross-sectional SEM and EDX images of nanoporous Si half cells with the different amounts of CA at the 50th cycle. Based on EDX mapping images, in which Si, S, and C are colored in blue, yellow, and red, respectively, Si particles/aggregates were highly dispersed in $75Li_2S{\cdot}25P_2S_5$ matrix. As we prepared, the red dots representing C element increased with the amount of CA. In addition, cracks were observed between Si aggregates and SE as indicated by dashed ellipses in Figure 4-1(c), (d), (g), and (h). The number and size of cracks appear to increase as CA content increases.

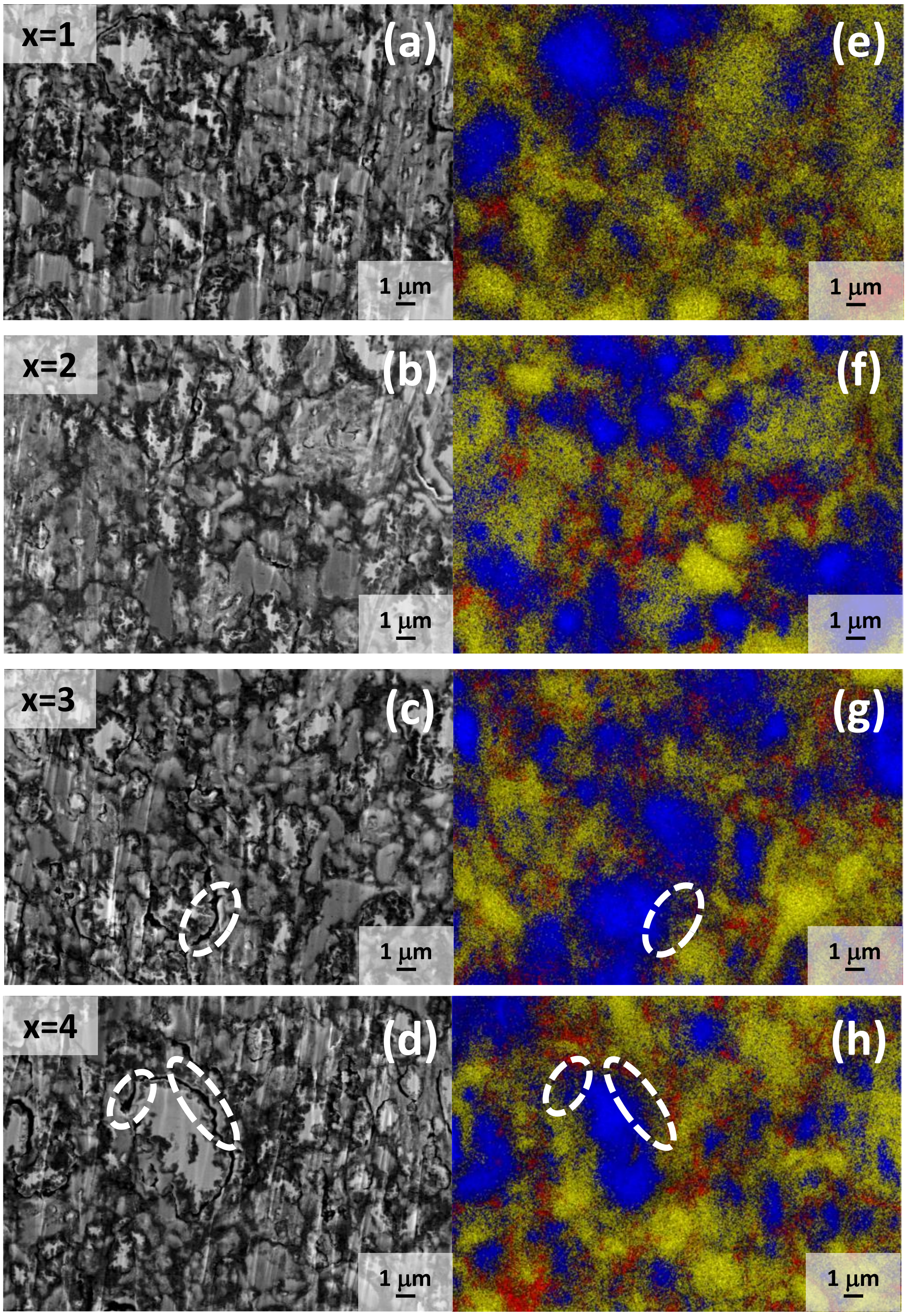

Figure 4-1. (a, b, c, d) Cross-sectional SEM images and (e, f, g, h) EDX mapping images of nanoporous Si half cells with various amounts of CA (nanoporous Si particles:SE:CA=4:6:x weight ratio). In EDX mapping images, Si, S, and C are colored in blue,

I-V characteristics of two half cells with the different CA contents are shown in Figure 4-2. The electrical conductivities calculated from the linear changes were 4.1×10^{-4} S cm^{-1} and 6.8×10^{-4} S cm^{-1} at x=1 and 4, respectively. Namely, the electrical conductivity increased about 1.7 times when the weight ratio of CA was 4 times. Table 4-1 shows the initial charge/discharge capacities and CE of the half cells with CA weight ratio of x=1, 2, 3, and 4. The charge capacity proportionately increased from 2700 mAh g^{-1} to 3015 mAh g^{-1} with CA content (Figure 4-3). The experimental results of electrical conductivity and charge capacity show that the conduction paths can be newly constructed in nanoporous Si composite anodes by adding CA. Regarding charge capacity, it is important to understand the change in Li-Si phase with the insertion of Li$^+$ ions. Although the crystalline phases normally have lower Gibbs free energy than their amorphous counterparts, the initial products in the electrochemical lithiation process are always amorphous Li_ySi ($0<y<3.75$). Then, at y=3.75, the amorphous phase suddenly crystallizes to form $Li_{15}Si_4$ with a theoretical capacity of 3579 mAh g^{-1} [19]. This is the highest lithiated phase achievable at ambient temperature. In fact, initial charge capacities of around 3500 mAh g^{-1} have been confirmed in many LIBs with liquid electrolytes [20]. Although the capacity (3015 mAh g^{-1}) of nanoporous Si half cell with x=4 is close to that of $Li_{15}Si_4$, there is a difference over 500 mAh g^{-1}. This is probably because the isolated Si particles/aggregates outside the conduction channels are not involved in charging. Namely, the amount of CA should be further increased to reach an intrinsic high capacity of Si. As summarized in Table 4-1, all the half cells exhibited CE below 70%. We note the oxide layers as the origin of these low CE, because they irreversibly consume Li. This is reasonable because the signals from SiO_x were clearly observed in XPS profiles of Si particles, as shown in Figure 2-10 (see Paragraph 2.4.2). In particular, numerous oxide layers are possibly formed owing to the large specific surface area attributable to the nanoporous structure.

Figure 4-4 compares the cycle performance of nanoporous Si half cells with various CA contents, including non-porous Si half cell as a reference. The discharge capacities

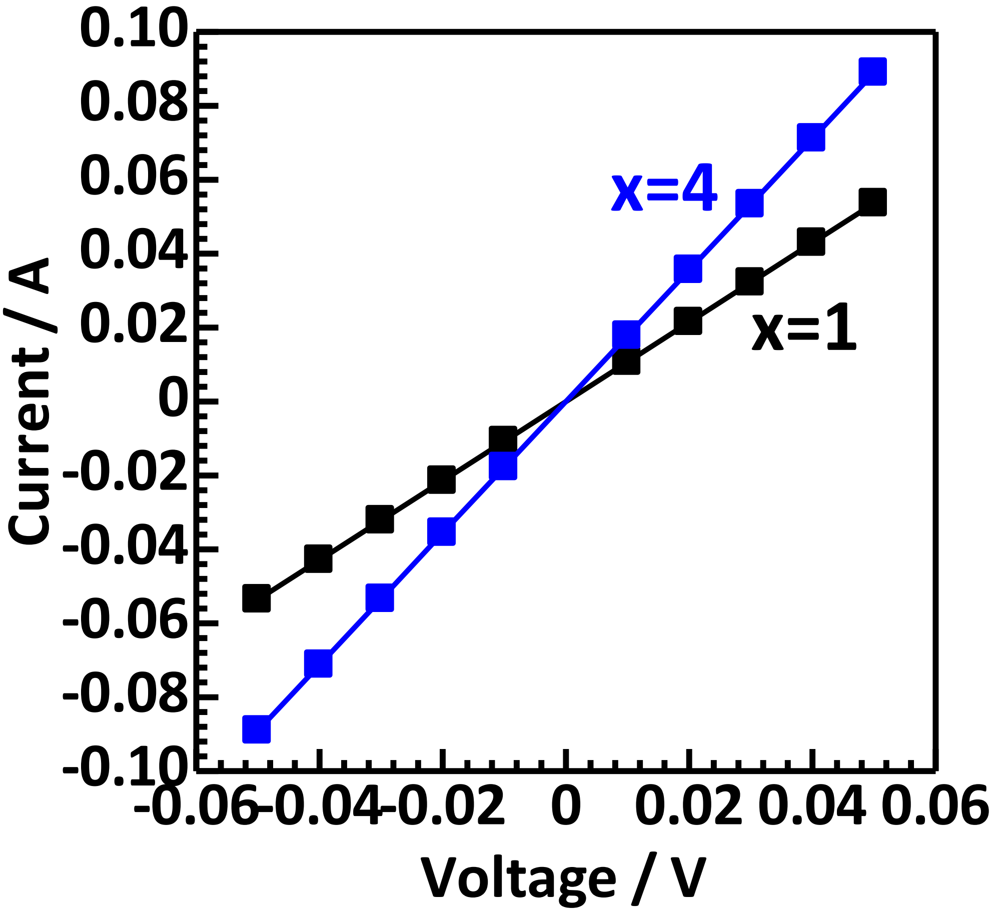

Figure 4-2. I-V characteristics of nanoporous Si half cells with different amounts of CA (nanoporous Si particles:SE:CA=4:6:x weight ratio).

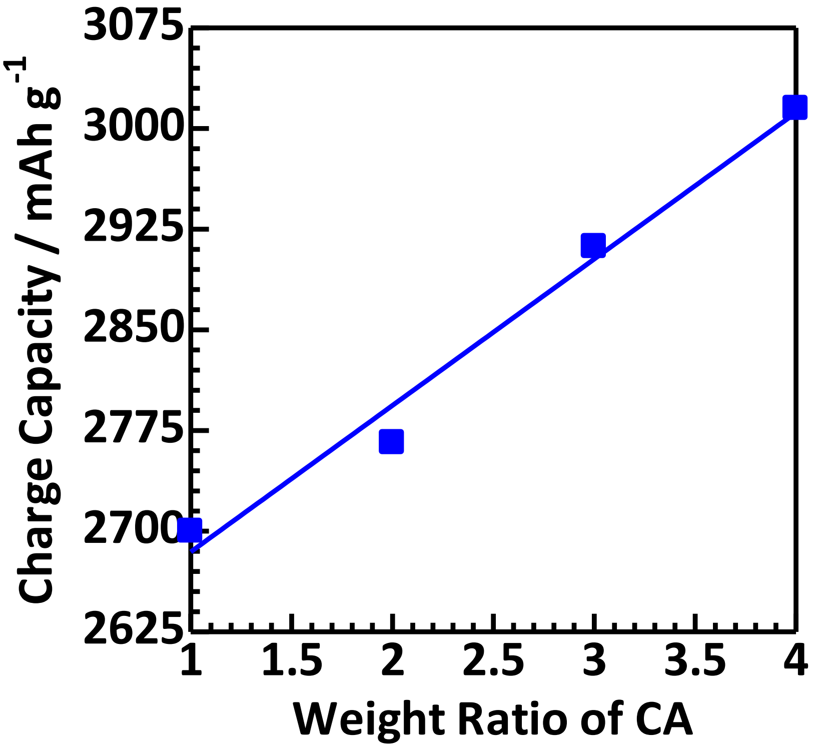

Figure 4-3. Relationship between CA content and initial charge capacity of nanoporous Si half cells.

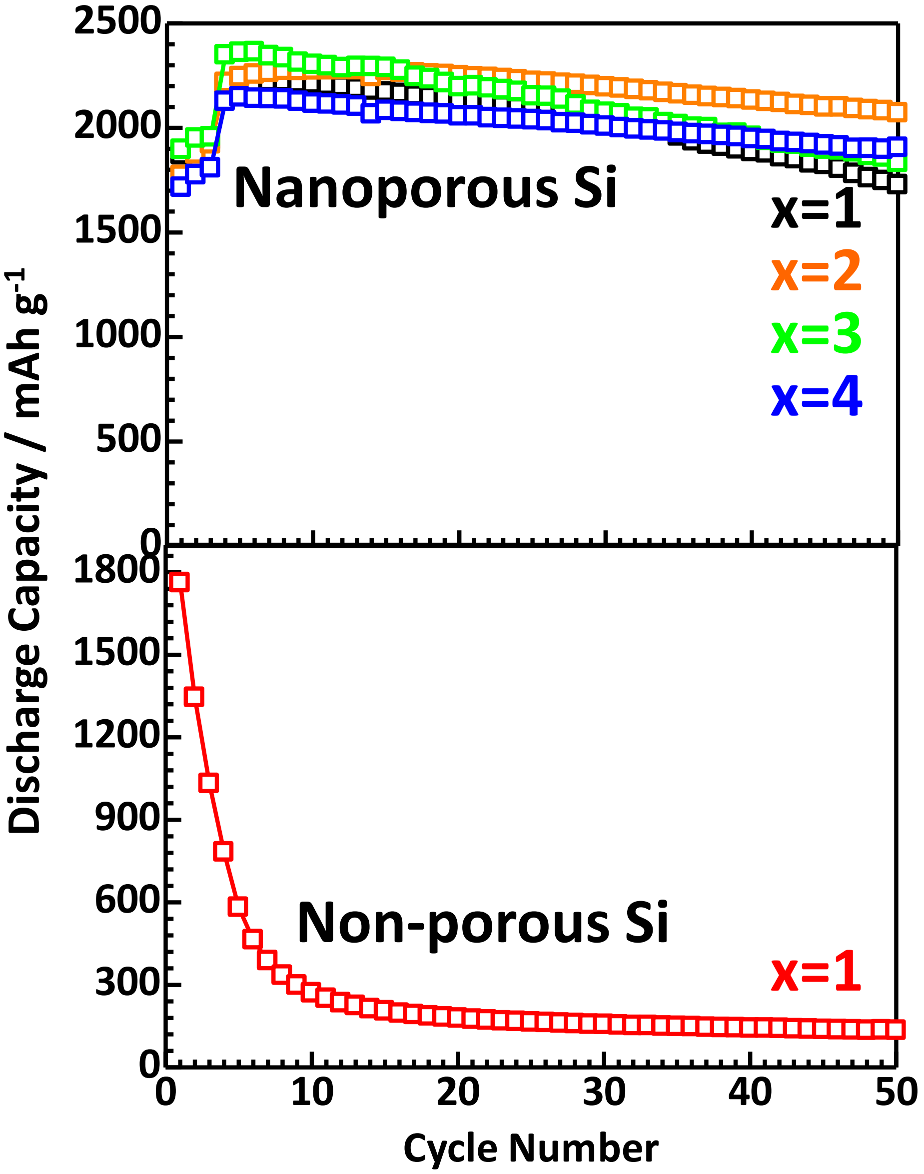

Figure 4-4. Cycle performance of nanoporous Si half cells with various amounts of CA (nanoporous Si particles:SE:CA=4:6:x weight ratio). The data of non-porous Si half cell with CA weight ratio of x=1 are shown as reference.

Table 4-1. Initial charge/discharge performance of nanoporous Si half cells with various amounts of CA (nanoporous Si particles:SE:CA=4:6:x weight ratio). The data of non-porous Si half cell with CA weight ratio of x=1 are shown as reference.

Si Particles	Weight Ratio (Si:SE:CA=4:6:x)	Initial Charge Capacity (mAh g^{-1})	Initial Discharge Capacity (mAh g^{-1})	Coulombic Efficiency (%)
Nanoporous	x=1	2700	1871	69
Nanoporous	x=2	2766	1771	64
Nanoporous	x=3	2912	1896	65
Nanoporous	x=4	3015	1715	57
Non-porous	x=1	2829	1761	62

and capacity retentions are summarized in Table 4-2. The maximum discharge capacity is defined as the highest value after four cycles measured using constant current/constant voltage mode. The capacity retention is the ratio of the discharge capacity at the 50th cycle to the maximum discharge capacity. The discharge capacity of nanoporous Si half cells gradually decreased with increasing the number of cycles. In contrast, non-porous Si half cell exhibited a dramatic decrease. Among all the half cells prepared, nanoporous Si half cell with x=2 exhibited the maximum values in both of the discharge capacity and capacity retention at the 50th cycle. The discharge capacity of 2071 mAh g^{-1} was approximately 15.5 times higher than the observed capacity of non-porous Si half cell (134 mAh g^{-1}). In addition, the capacity retention (91%) was extremely large compared to non-porous Si half cell (17%). Regarding cyclability, Liu showed that Si particles neither crack nor fracture upon lithiation below a particle diameter of 150 nm [21]. The diameter of nanoporous and non-porous Si particles in this study were estimated as 479 nm and 466 nm by DLS, respectively (see Table 2-1 in Section 2.5). Therefore, the excellent cycling property of nanoporous Si half cells is not attributed to the size effect. These results indicate that the nanoporous structure successfully mitigates the large volume change of Si particles/aggregates during charge and discharge.

As described above, the effect of CA on the electrical conductivity and initial charge capacity can be clearly explained by the conduction paths in nanoporous Si composite anodes. On the other hand, the electrochemical characteristics after cycling are rather complexly related to CA content. Both of the discharge capacity and capacity retention at the 50th cycle fluctuate after reaching a peak at x=2, as shown in Table 4-2. Here note that the cracks were clearly observed between Si aggregates and SE in the half cells with x=3 and 4 (see the dashed ellipses in Figure 4-1). As demonstrated in our previous study [22,23], the structural stress arising from Si is relieved by the elastic deformation of the surrounding SE. The good response to volume change is possibly due to the low Young's modulus of $75Li_2S \cdot 25P_2S_5$ [24]. However, such a relaxation effect is weakened when CA exceeds a certain amount, resulting in the occurrence of cracks. Namely, there is an optimum amount of CA for cycle performance: x=2 in this study.

Table 4-2. Cycle performance of nanoporous Si half cells with various amounts of CA (nanoporous Si particles:SE:CA=4:6:x weight ratio). The data of non-porous Si half cell with CA weight ratio of x=1 are shown as reference.

Si Particles	Weight Ratio (Si:SE:CA=4:6:x)	Maximum Discharge Capacity[*1] (mAh g^{-1})	Discharge Capacity at 50th Cycle (mAh g^{-1})	Capacity Retention[*2] (%)
Nanoporous	x=1	2224	1727	78
Nanoporous	x=2	2277	2071	91
Nanoporous	x=3	2363	1834	78
Nanoporous	x=4	2147	1906	89
Non-porous	x=1	782	134	17

*1 Maximum discharge capacity is the highest discharge capacity after the fourth cycle.
*2 Capacity retention is the ratio of the discharge capacity at the 150th cycle to the maximum discharge capacity.

4.3. Quantitative Evaluation of Structural Stress using Full Cell Configuration

4.3.1. Experimental

Cathode and anode composite materials were composed of $LiNi_{1/3}Mn_{1/3}Co_{1/3}O_2$ (NMC):SE:AB=70:30:5 weight ratio and nanoporous Si particles (NPS-F):SE:AB=40:60:10 weight ratio, respectively. Full cells equipped with a load cell were fabricated by the procedure shown in Figure 4-5. First, SE (80 mg) was pressed in an electric insulation tube under 37 MPa. Second, the anode composite material (2 mg) were overlapped at a pressure of 259 MPa to obtain a two-layered pellet. Third, after turning the cell upside down, the current collector was removed. Finally, the cathode composite material (11 mg) was pressed under 259 MPa to complete full cell configuration. In addition, a load cell (UNIPULCE, USH-10KN) was inserted at the bottom of full cells. The fabrication processes of SE and half cells are explained in Paragraph 3.2.1.

Electrochemical tests were conducted in the constant current mode of 0.127 mA cm^{-2} (0.03 C) at 30°C using a charge/discharge measurement device (BTS-2004, Nagano). The cut-off voltages were 2.5 and 4.2 V. The load change was recorded on the monitor (UNIPULCE, FS-10). The measurement method of structural characteristics was described in Paragraph 3.2.1.

4.3.2. Results and Discussion

Figure 4-6(a) shows the initial charge and discharge curves of nanoporous and non-porous Si full cells, including NMC half cell as reference. For comparison, the characteristics of nanoporous and non-porous Si half cells are shown in Figure 4-6(b) [22]. Their initial charge/discharge capacities and CE are summarized in Table 4-3. The initial charge capacities of three cells with NMC composite cathode were similar to each other (mean value: 164 mAh g^{-1}). These are close to a theoretical capacity of NMC (163 mAh g^{-1}) [25]. Here, nanoporous and non-porous Si half cells as the references exhibited high initial charge capacities of 2700 mAh g^{-1} and 2829 mAh g^{-1}, respectively. Therefore, the

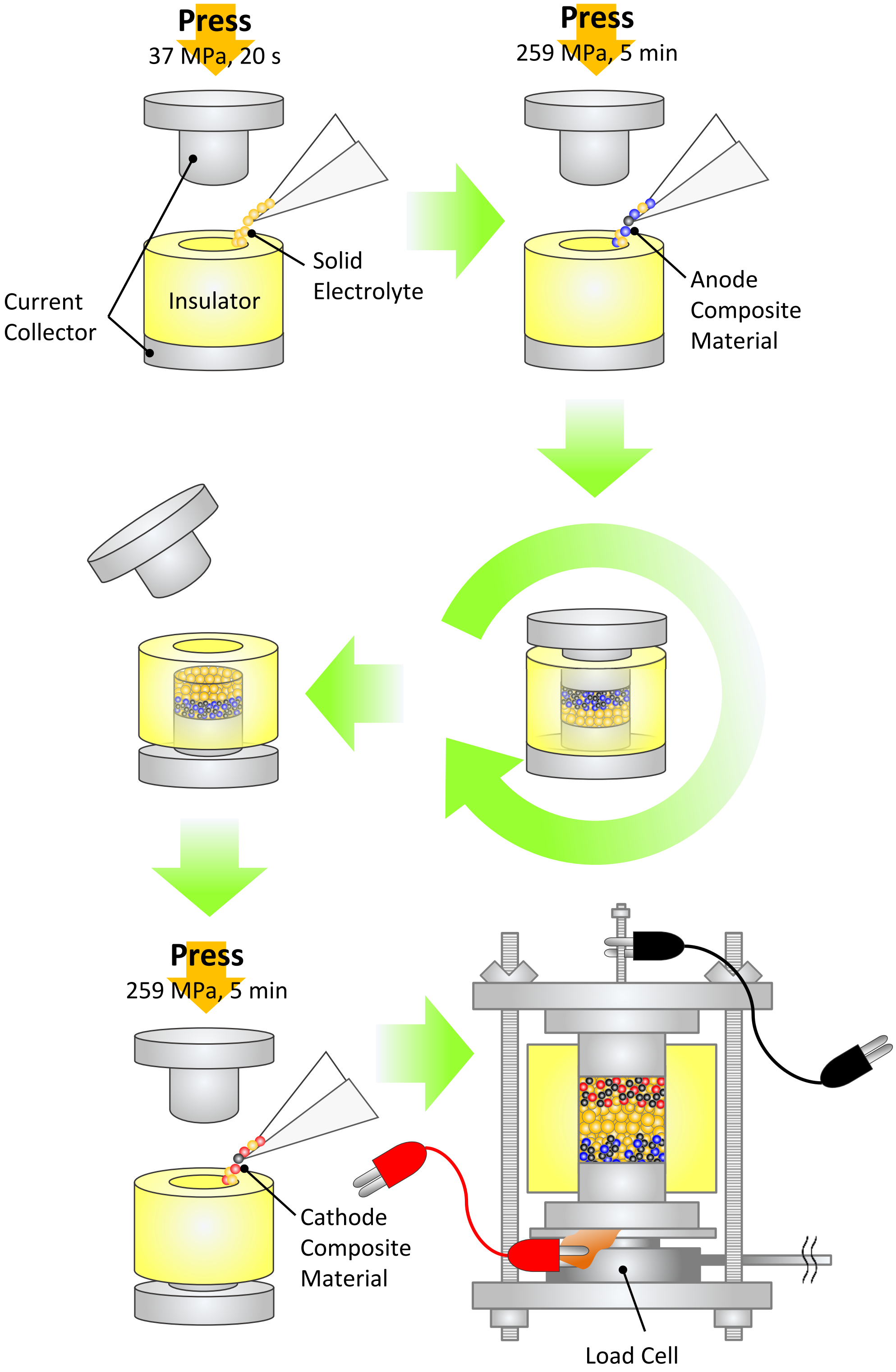

Figure 4-5. Fabrication process of full cells.

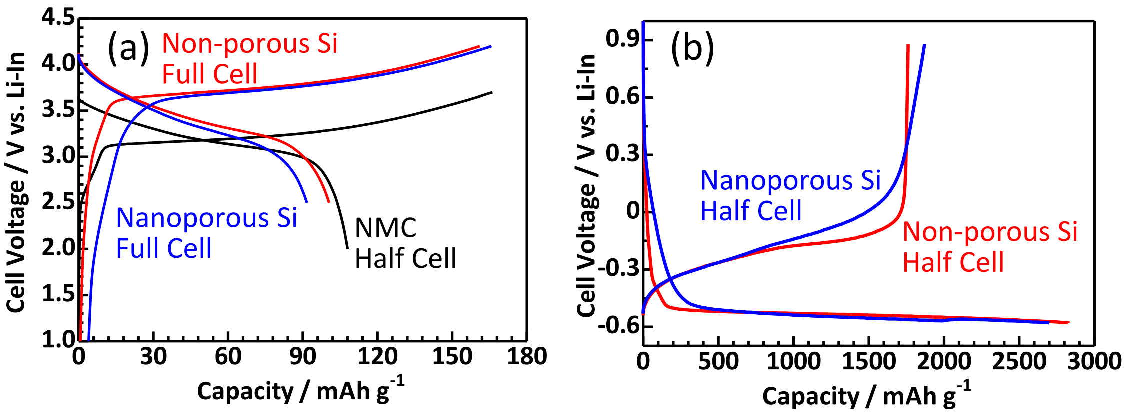

Figure 4-6. Initial charge and discharge curves of (a) nanoporous and non-porous Si full cells, and NMC half cell and (b) nanoporous and non-porous Si half cells.

Table 4-3. Charge and discharge characteristics of various full and half cells.

Configuration	Cell Type	Initial Charge Capacity (mAh g^{-1})	Initial Discharge Capacity (mAh g^{-1})	Coulombic Efficiency (%)
Nanoporous Si/SE/NMC	Full	166	92	55
Non-porous Si/SE/NMC	Full	161	101	62
Li-In/SE/NMC	Half	166	108	65
Nanoporous Si/SE/Li-In	Half	2700	1871	69
Non-porous Si/SE/Li-In	Half	2829	1761	62

charge characteristics of full cells are limited by NMC composite cathode. On the other hand, the initial discharge capacities of nanoporous and non-porous Si full cells were 92 mAh g^{-1} and 101 mAh g^{-1}, corresponding to 55% and 62% of CE, respectively. These values were smaller than 108 mAh g^{-1} of NMC half cell. This is probably because Si oxides form several Li oxides (Li_2O, Li_4SiO_4, and $Li_2Si_2O_5$) which show no reversible reactions. This consideration can be supported by the results of XPS measurements. Namely, as shown in Figure 2-10 (see Paragraph 2.4.2), the feature of Si 2p profiles indicates the oxidized layers on the surface of both Si particles.

Figure 4-7 shows the time dependence of cell voltage and load pressure in nanoporous and non-porous Si full cells. Although the cell voltage was raised to 4.2 V over 12 hours in charging, the load on nanoporous Si full cell was remained nearly constant at 56.4 MPa. In addition, no change was observed during discharge for 8 hours, resulting in negligibly small load change in the lithiation/delithiation process. On the other hand, the load on non-porous Si full cell gradually increased with charging, reaching 57.3 MPa at full charge. A similar behavior was observed during discharge and the load returned to 56.5 MPa. As the result, the load change of nanoporous Si full cell was 0.8 MPa. Here, NMC-based cathodes are well known to have no load change in the charge/discharge process [26]. Therefore, the obvious change of load in non-porous Si full cell is caused by the expansion and contraction of Si particles/aggregates in the lithiation/delithiation process. In contrast, nearly constant load in nanoporous Si full cell indicates that the nano-sized pores successfully mitigate the large volume change of Si.

Figure 4-8 shows the cycle performance of nanoporous Si full cell, including non-porous Si full cell and NMC half cell as references. As summarized in Table 4-4, the discharge capacity (53 mAh g^{-1}) and capacity retention (57%) of nanoporous Si full cell at the 50th cycle were similar to 57 mAh g^{-1} and 53% of NMC half cell, respectively. On the other hand, non-porous Si full cell exhibited the poorer cycle performance. In order to understand the electrochemical characteristics described above, the cross-sectional SEM and EDX images of nanoporous and non-porous Si full cells were measured after

50 cycles (Figure 4-9). Nanoporous Si composite anode exhibited no cracks, whereas a lot of cracks were observed in non-porous Si composite anode. NMC particles in the cathodes of both cells possessed the characteristic hollow core surrounded by dense shell, which has been also reported in the previous studies [27]. Here, note that almost all NMC particles were cracked in non-porous Si full cell. The expansion of Si particles/aggregates, which is responsible for large load changes (0.8 MPa) during charging, cause plastic deformation in the surrounding SE. As the result, the propagated compressive stress cracks NMC, decreasing discharge capacity (25 mAh g^{-1}) and capacity retention (25%) in non-porous Si full cell. In contrast, no cracks were observed in the cathode of nanoporous Si full cell. The results of cycle performance and SEM measurements show that the structural stress of Si was relieved by the nanoporous structure.

To consistently explain all the experimental results, we propose the electrochemical mechanism as follows. In nanoporous Si full cell, the volumetric expansion of Si at lithiation is mainly buffered by the shrinkage of nano-sized pores. In addition, the structural stress arising from the slightly expanded Si is relieved by the elastic deformation of the surrounding SE ($75Li_2S \cdot 25P_2S_5$). During delithiation, the elastically deformed SE returns to its original shape and maintains the contact with Si particles/aggregates. Such a good response to volume change can be attributed to the low Young's modulus (22.9 GPa) of $75Li_2S \cdot 25P_2S_5$ [28]. On the other hand, non-porous Si particles/aggregates give large stress on the surrounding SE during lithiation and cause the cracks in NMC composite cathode. In the delithiation process, voids are formed between Si aggregates and plastically deformed SE, resulting in the low capacity retention.

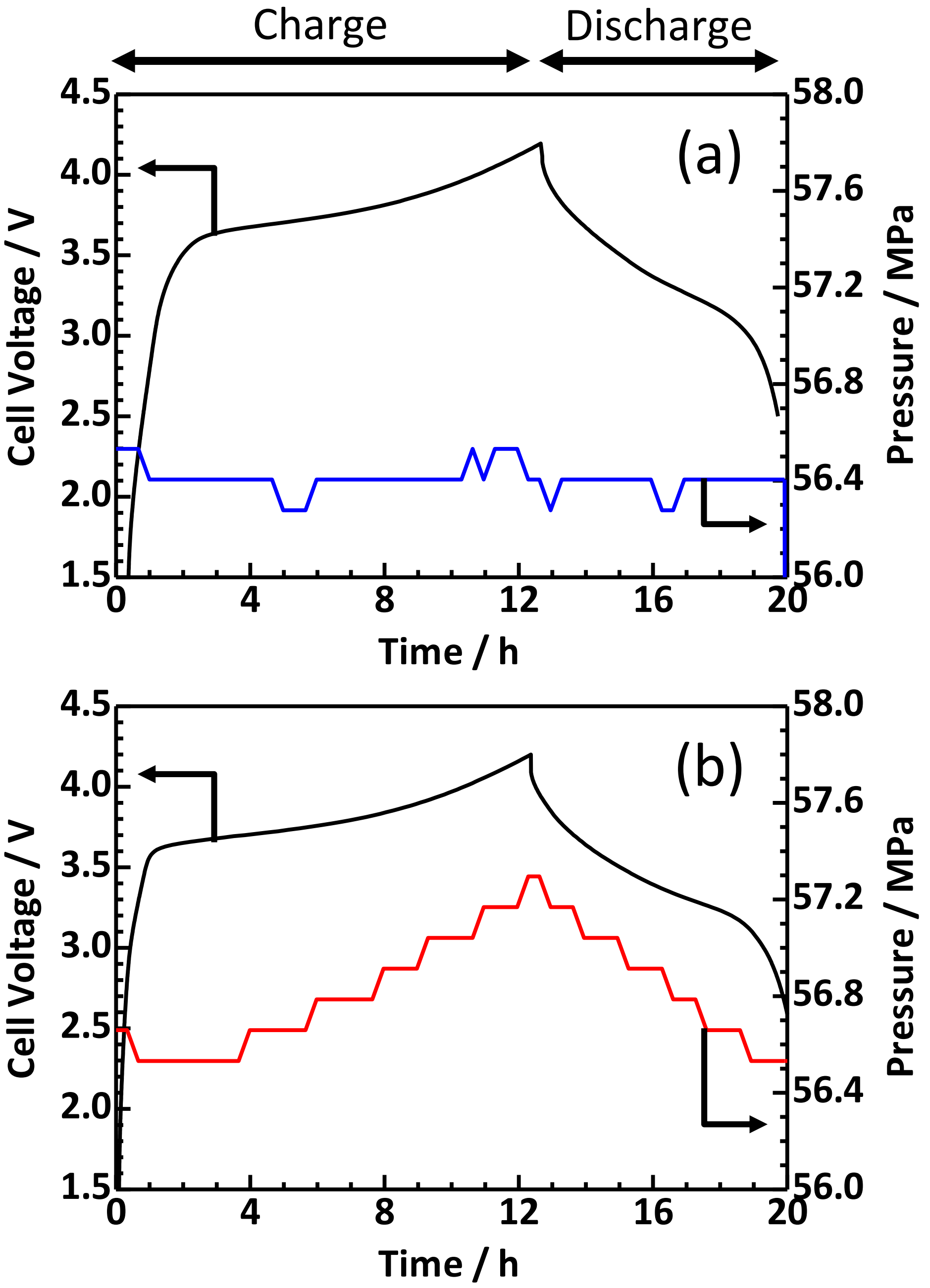

Figure 4-7. Load change during charge and discharge of (a) nanoporous and (b) non-porous Si full cells.

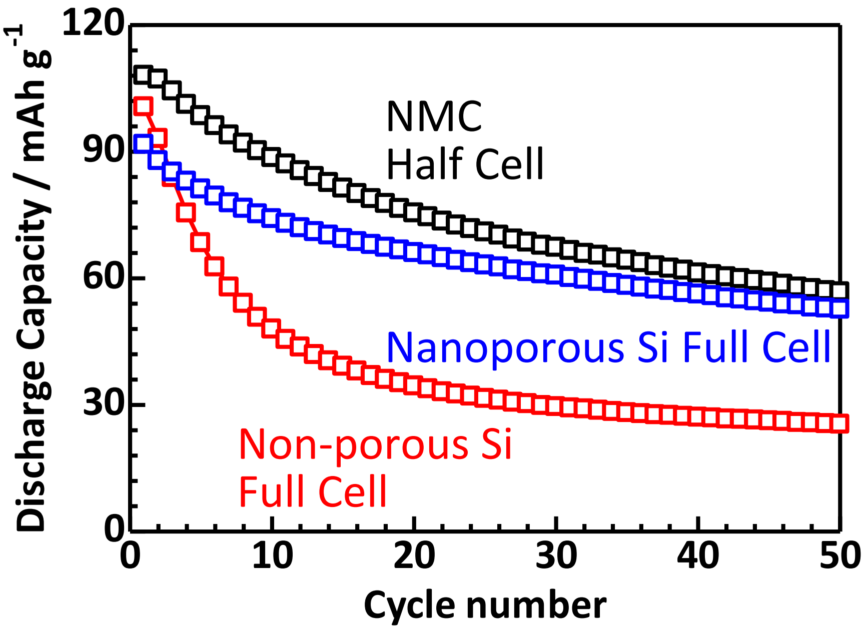

Figure 4-8. Cycle performance of nanoporous and non-porous Si full cells, and NMC half cell.

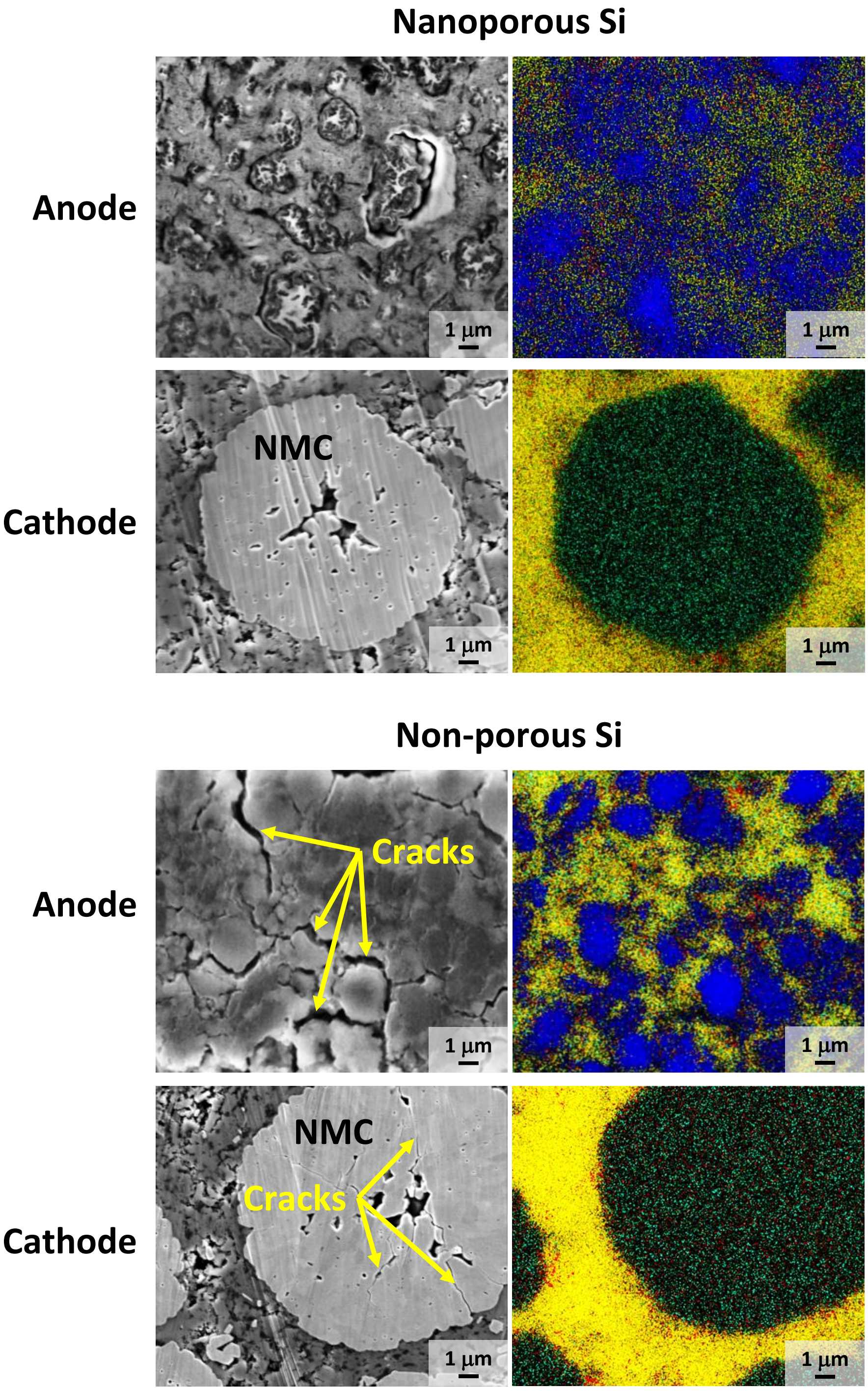

Figure 4-9. Cross-sectional SEM and EDX images of nanoporous Si and non-porous Si full cells. In EDX mapping images, Si, S, C, and Ni are colored in blue, yellow, red, and light blue, respectively.

Table 4-4. Cycle performance of various full and half cells.

Configuration	Cell Type	Initial Discharge Capacity (mAh g^{-1})	Discharge Capacity at 50th Cycle (mAh g^{-1})	Capasity Retention[*1] (%)
Nanoporous Si/SE/NMC	Full	92	53	57
Non-porous Si/SE/NMC	Full	101	25	25
Li-In/SE/NMC	Half	108	57	53
Nanoporous Si/SE/Li-In	Half	1871	1727	92
Non-porous Si/SE/Li-In	Half	1761	134	8

*1 Capacity retention is the ratio of the discharge capacity at the 50th cycle to the initial discharge capacity.

4.4. Summary

The electrochemical characteristics of half cells with nanoporous Si composite anodes were improved by optimizing the amounts of CA. First, the electrical conductivity and charge capacity simply increased with the concentration of CA. This is because Si particles/aggregates involved in the conduction and charge processes increase upon contact with CAs. Second, there was an optimum amount of CA for cycle performance. The cross-sectional SEM and EDX images after 50 cycles showed that cracks occurred between Si aggregates and SE over weight ratio of NPS-F:SE:AB=4:6:3. The important achievements are as follows:

1) Electrical conductivity of 6.8×10^{-4} S cm^{-1} in NPS-F:SE:AB=4:6:4 weight ratio
2) Initial charge capacity of 3015 mAh g^{-1} in NPS-F:SE:AB=4:6:4 weight ratio
3) Discharge capacity of 2071 mAh g^{-1} at 50th cycle in NPS-F:SE:AB=4:6:2 weight ratio
4) Capacity retention of 91% at 50th cycle in NPS-F:SE:AB=4:6:2 weight ratio

CAs necessarily continue to be the major elements of composite electrodes, even if new coating materials are developed in future. Therefore, optimizing their concentration is crucial to improve the performance of ASSLIBs.

In the full cell with NMC composite cathode and NPS-F composite anode, it was demonstrated that nanoporous structure acted as the buffer regions for large volume change of Si particles/aggregates during charge and discharge. Namely, the load of NPS-F cell was almost constant during charge and discharge, while there was a large load change in non-porous Si full cell. Moreover, although no cracks were observed in NPS-F full cell, almost all of NMC aggregates in non-porous Si full cell were cracked due to plastic deformation at the surrounding SE. The important achievements are as follows:

1) Negligibly small load change in NPS-F full cell compared to 0.8 MPa in non-porous Si full cell
2) 2.1 times higher discharge capacity at 50th cycle in NPS-F full cell versus non-

porous Si full cell

3) 2.3 times higher capacity retention at 50th cycle in NPS-F full cell versus non-porous Si full cell

In NPS-F full cell, the volume expansion of Si at lithiation is buffered mainly by the contraction of pores. In addition, the stress from the slightly expanded Si is relieved by the elastic deformation of the surrounding SE. During delithiation, the elastically deformed SE returns to its original shape and maintains contact with Si particles/aggregates. The good response to volume change can be attributed to the low Young's modulus of $75Li_2S\cdot25P_2S_5$ solid electrolyte. This is the first study to quantitatively evaluate the stress relaxation of Si due to the pore structure in full cell configuration.

References

[1] Y. Cai and C. L. Fan, *Electrochim. Acta*, **58** (2011) 481-487.

[2] M. E. Spahr, D. Goers, A. Leone, S. Stallone, and E. Grivei, *J. Power Sources*, **196** (2011) 3404-3413.

[3] T. Chen, L. Pan, X. Liu, and Z. Sun, *Mater. Chem. Phys.*, **142** (2013) 345-349.

[4] Y. H. Chen, C. W. Wang, G. Liu, X. Y. Song, V. S. Battaglia, and A. M. Sastry, *J. Electrochem. Soc.*, **154** (2007) A978-A986.

[5] N. H. Kwon, D. Mouck-Makanda, and K. M. Fromm, *Batteries*, **4** (2018) 50.

[6] O. S. Medvedev, Q. Wang, A. A. Popovich, and P. A. Novikov, *Ionics*, **26** (2020) 4277-4286.

[7] F. Joho, B. Rykart, R. Imhof, P. Novák, M. E. Spahr, and A. Monnier, *J. Power Sources*, **81-82** (1999) 243-247.

[8] X. L. Li, K. Du, J. M. Huang, F. Y. Kang, and W. C. Shen, *J. Phys. Chem. Solids*, **71** (2010) 457-459.

[9] W. R. Liu, Z. Z. Guo, W. S. Young, D. T. Shieh, H. C. Wu, M. H. Yang, and N. L. Wu, *J. Power Sources*, **140** (2005) 139-144.

[10] B. P. N. Nguyen, N. A. Kumar, J. Gaubicher, F. Duclairoir, T. Brousse, O. Crosnier, L. Dubois, G. Bidan, D. Guyomard, and B. Lestriez, *Adv. Energy Mater.*, **3** (2013) 1351-1357.

[11] B. P. N. Nguyen, J. Gaubicher, and B. Lestriez, *Electrochim. Acta*, **120** (2014) 319-326.

[12] Z. Karkar, D. Mazouzi, C. R. Hernandez, D. Guyomard, L. Roué, and B. Lestriez, *Electrochim. Acta*, **215** (2016) 276-288.

[13] M. Yoshio, H. Wang, K. Fukuda, T. Umeno, N. Dimov, and Z. Ogumi, *J. Electrochem. Soc.*, **149** (2002) A1598-A1603.

[14] N. Dimov, K. Fukuda, T. Umeno, S. Kugino, and M. Yoshio, *J. Power Sources*, **114** (2003) 88-95.

[15] N. Dimov, S. Kugino, and M. Yoshio, *Electrochim. Acta*, **48** (2003) 1579-1587.

[16] D. M. Piper, T. A. Yersak, and S. H. Lee, *J. Electrochem. Soc.*, **160** (2013) A77-A81.

[17] G. Bucci, T. Swamy, S. Bishop, B. W. Sheldon, Y. M. Chiang, and W. C. Carter, *J. Electrochem. Soc.*, **164** (2017) A645-A654.

[18] D. H. Kim, H. A. Lee, Y. B. Song, J. W. Park, S. M. Le, and Y. S. Jung, *J. Power Sources*, **426** (2019) 143-150.

[19] M. Gu, Z. Wang, J. G. Connell, D. E. Perea, L. J. Lauhon, F. Gao, and C. Wang, *ACS Nano*, **7** (2013) 6303-6309.

[20] J. P. Maranchi, A. F. Hepp, and P. N. Kumta, Electrochem. *Solid-State Lett.*, **6** (2003) A198-A201.

[21] X. H. Liu, L. Zhong, S. Huang, S. X. Mao, T. Zhu, and J. Y. Huang, *ACS Nano*, **6** (2012) 1522-1531.

[22] R. Okuno, M. Yamamoto, A. Kato, and M. Takahashi, *Electrochem. Commun.*, **130** (2021) 107100.

[23] R. Okuno, M. Yamamoto, A. Kato, and M. Takahashi, *J. Electrochem. Soc.*, **167** (2020) 140522.

[24] A. Sakuda, A. Hayashi, and M. Tatsumisago, *Sci. Rep.*, **3** (2013) 2261.

[25] R. Jung, M. Metzger, F. Maglia, C. Stinner, and H. A. Gasteiger, *J. Electrochem. Soc.*, **164** (2017) A1361-A1377.

[26] N. Yabuuchi and T. Ohzuku, *J. Power Sources*, **119** (2003) 171-174.

[27] M. Zukalova, J. Prochazka, A. Zukal, and L. Kavan, *ECS Trans.*, **95** (2019) 55-63.

[28] A. Kato, M. Nose, M. Yamamoto, A. Sakuda, A. Hayashi, and M. Tatsumisago, *J. Ceram. Soc. Jpn.*, **126** (2018) 719-727.

5. GENERAL CONCLUSIONS

This thesis focused on the development of ASSLIBs with high energy density and long cycle life. The first approach was the accommodation to the large volumetric expansion of Si utilizing the shrinkage of nano-sized pores. The second was the increase of interface adhesion with Si by using sulfide-based solid electrolyte (SE) with low Young's modulus. To the best of my knowledge, this is the first study to employ nanoporous Si particles as the anode active material in ASSLIBs. This study mainly discussed the electrochemical characteristics of nanoporous Si-$75Li_2S{\cdot}25P_2S_5$ composites as the promising anode materials for ASSLIBs.

The following results and considerations were obtained.

1. Nanoporous Si particles could be successfully prepared by (i) air oxidation of Mg_2Si (NPS-A) and (ii) Mg_2Si reduction of mesoporous SiO_2 (NPS-M) or SiO_2 fumes (NPS-F):

$$\text{(i) } Mg_2Si + O_2 \text{ (air)} \rightarrow Si + 2MgO$$
$$\text{(ii) } Mg_2Si + SiO_2 \rightarrow 2Si + 2MgO$$

These processes are very simple. In addition, the raw materials are inexpensive and easy to handle in comparison with other processes using gas, liquid, or solid phase reaction. Therefore, there are the advantages in the mass production and manufacturing cost. The structural data of the prepared nanoporous Si particles are as follows:

1) NPS-A
   Particle size: 506 nm, Pore size: 9.4 nm, and Surface area: 144 $m^2\ g^{-1}$
2) NPS-M

Particle size: 354 nm, Pore size: 6.0 nm, and Surface area: 201 m^2 g^{-1}

3) NPS-F

Particle size: 479 nm, Pore size: 5.9 nm, and Surface area: 213 m^2 g^{-1}

2. The electrochemical characteristics of all-solid-state half/full cells were significantly improved by anodes compositing nanoporous Si particles with $75Li_2S\cdot25P_2S_5$ SE. The important achievements were as follows:

   1) Discharge capacity:

   1317 mAh g^{-1} at 150th cycle: 3.5 times higher than graphite

   15 times higher than non-porous Si

   2) Capacity retention:

   95% at 150th cycle: 5.6 times higher than non-porous Si

   3) Load change:

   Negligibly small: 0.8 MPa in non-porous Si

   Regarding the improvement of the electrochemical characteristics described above, the mechanism was proposed as follows. The nanoporous structure acts as the buffer regions for large volume change of Si particles/aggregates during charge and discharge. Namely, the volume expansion of Si during lithiation is mainly buffered by the shrinkage of pores. The stress from Si expanded slightly outward is relieved by elastic deformation of the surrounding SE. During delithiation, the elastically deformed SE returns to its original shape and retains contact with Si particles/aggregates. The good response to volume change is possibly owing to the low Young's modulus (22.9 GPa) of $75Li_2S\cdot25P_2S_5$.

3. The excellent electrochemical characteristics of half cells with nanoporous Si composite anodes were obtained by optimizing the amounts of conductive additive (acetylene black: AB). This is because the conduction path in the cell increases as the conductive additive increases. As the result, more Si particles/aggregates can be

involved in the charge/discharge process. The important achievements are as follows:

1) Electrical conductivity
   6.8×10^{-4} S cm^{-1} in NPS-F:SE:AB=4:6:4 weight ratio
2) Initial charge capacity
   3015 mAh g^{-1} in NPS-F:SE:AB=4:6:4 weight ratio
3) Discharge capacity
   2071 mAh g^{-1} at 50th cycle in NPS-F:SE:AB=4:6:2 weight ratio

4. By comparing the electrochemical and structural characteristics of NPS-A, NPS-M, and NPS-F half cells, several directions on nanoporous Si particles were obtained to further improve the battery performance as follows:

1) Large capacity
   Suppress surface oxidation
   Increase particle size
2) Large coulombic efficiency
   Suppress surface oxidation
3) High capacity retention
   Increase pore size
   Increase dispersibility in composites

Mg_2Si reduction of SiO_2 is more suitable for the preparation of higher-purity nanoporous Si particles. On the other hand, the air oxidation of Mg_2Si is appropriate to increase the particle size and pore size of nanoporous Si. In order to increase the dispersibility of Si particles, mechanical milling should be used to prepare the composites.

5. This thesis is the first microscopic study to demonstrate that the nanoporous structure relieves the volume change of Si. In this regard, the cross-sectional SEM/EDX and electrochemical impedance spectroscopy (EIS) measurements are powerful tools for

analyzing Si-SE interface. Namely, the cross-sectional SEM and EDX images at the 50th cycle showed that Si particles/aggregates entangled the surrounding SE in nanoporous Si half cell. As the result, no microcracks are generated at Si-SE interface. Similar SEM and EDX observations were obtained for nanoporous Si full cells. On the other hand, many large cracks were observed at the boundary between Si and SE grains in non-porous Si half cells. In addition, in non-porous Si full cells, the plastic deformation in the surrounding SE cracked almost all the composite cathode particles/aggregates. These microstructural features were fully consistent with the change of interfacial resistance in EIS measurement. The experimental results described above demonstrated that nanoporous structure acted as the buffer regions for large volume change of Si particles/aggregates during charge and discharge.

6. I systematically investigated the electrochemical characteristics of composite anodes consisting of nanoporous Si particles and $75Li_2S{\cdot}25P_2S_5$ SE. Main findings can be summarized as follows: 1) the large volumetric expansion of Si is buffered by the shrinkage of the pores; 2) the elasticity of $75Li_2S{\cdot}25P_2S_5$ relieves the strains arising from the expanded Si particles; and 3) these two effects are enhanced when Si particles are highly dispersed in $75Li_2S{\cdot}25P_2S_5$ matrix. The composite anodes in the present study have a high areal mass loading of 0.90 mg cm^{-2}, which is applicable to practical batteries. Meanwhile, although the initial CE is not high enough, further processing, such as removing the surface SiO_x with HF, overcoating conductive carbon, and/or adjusting the compressive pressure, would lead to additional improvements. In conclusion, the proposed approach is a novel and unique way to improve the charge/discharge capacity and cycle stability of ASSLIBs with Si composite anodes. My findings provide valuable information to design composite anodes for ASSLIBs, enabling them to meet the energy demands of next-generation applications.

ACKNOWLEDEMENTS

The present study has been conducted under the guidance of Professor Masanari Takahashi (Nara Institute of Science and Technology; Osaka Research Institute of Industrial Science and Technology). I would like to express my greatest gratitude to him for his continuing interest, valuable discussion, and encouragement. I am pleased that I could study under Professor Takahashi for five years.

I would like to express my appreciation to Associate Professor Mari Yamamoto (Nara Institute of Science and Technology; Osaka Research Institute of Industrial Science and Technology) for her useful direction during this study. In particular, the author is grateful for her specific instruction on research subjects and her carefully proofreading the papers.

The author sincerely appreciates Professor Tsuyoshi Kawai and Professor Jun Ohta of Nara Institute of Science and Technology for their valuable suggestions and helpful comments to this thesis.

I am deeply grateful to Dr. Atsutaka Kato of Osaka Research Institute of Industrial Science and Technology for his perceptive indication and precise information. The author always respects his attitude and statements as a researcher.

The author acknowledges Dr. Yutaka Fujiwara and Dr. Yasuyuki Agari of Osaka Research Institute of Industrial Science and Technology for their valuable suggestions and discussion. I am also thankful to Mr. Yoshihiro Terauchi of Osaka Research Institute of Industrial Science and Technology for the technical direction with the experiment.

The author really appreciates Ms. Yuko Nakao (Rasa Industries, Ltd.) for her help in the measurement of specific surface area and pore size.

The author would like to thank all of the graduate students in Advanced Functional Materials Laboratory for their support to this research.

Finally, I want to thank my family. Without their long-term support and considerable encouragement, this thesis would not have been possible.

This work was partially supported by JSPS KAKENHI Grant Numbers JP16K06787, JP16K05949, JP19K05685, Grant-in-Aid for JSPS Fellows Grant Number 21J14403, NAIST Special Fund, and Hosokawa Powder Technology Foundation.

LIST OF PUBLICATIONS

Original articles regarding this study are as follows:

1. "Stable cyclability of porous Si anode applied for sulfide-based all-solid-state batteries"
   Ryota Okuno, Mari Yamamoto, Yoshihiro Terauchi, and Masanari Takahashi
   Energy Procedia, **156** (2019) 183-186. (Chapter 2 and 3)

2. "Microstructures of nanoporous-Si composite anodes in sulfide-based all-solid-state lithium-ion batteries"
   Ryota Okuno, Mari Yamamoto, Atsutaka Kato, Yoshihiro Terauchi, and Masanari Takahashi
   Materials Science and Engineering, **625** (2019) 012012. (Chapter 2 and 3)

3. "Stable cyclability caused by highly dispersed nanoporous Si composite anodes with sulfide-based solid electrolyte"
   Ryota Okuno, Mari Yamamoto, Atsutaka Kato, and Masanari Takahashi
   Journal of The Electrochemical Society, **167** (2020) 140522. (Chapter 2 and 3)

4. "Microscopic observation of nanoporous Si-Li_3PS_4 interface in composite anodes with stable cyclability"
   Ryota Okuno, Mari Yamamoto, Atsutaka Kato, and Masanari Takahashi
   Electrochemistry Communications, **130** (2021) 107100. (Chapter 2 and 3)

5. "High cycle stability of sulfide-based composite anodes with nanoporous Si particles prepared by Mg_2Si reduction of mesoporous SiO_2"
   Ryota Okuno, Mari Yamamoto, Atsutaka Kato, and Masanari Takahashi

Electrochemistry Communications, to be submitted. (Chapter 2 and 3)

6. "Improved performance of nanoporous Si composite anodes in all-solid-state lithium-ion batteries using conductive additive"
   Ryota Okuno, Mari Yamamoto, Atsutaka Kato, and Masanari Takahashi
   Electrochemistry Communications, to be submitted. (Chapter 2 and 4)

7. "Small load change in all-solid-state lithium-ion full cells with nanoporous Si composite anodes"
   Ryota Okuno, Mari Yamamoto, Atsutaka Kato, and Masanari Takahashi
   Journal of The Electrochemical Society, to be submitted. (Chapter 2 and 4)